TÉCNICO LISBOA

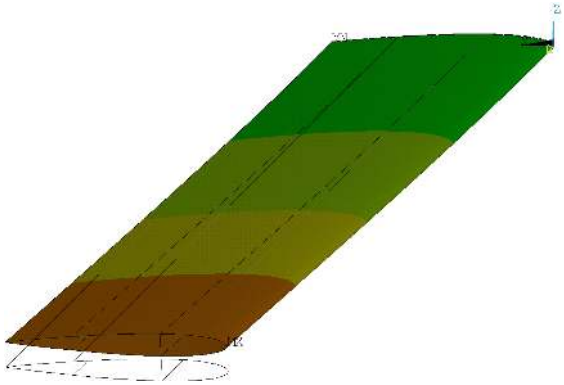

Aeroelastic Analysis of Aircraft Wings

André de Sousa Cardeira

Thesis to obtain the Master of Science Degree in

Aerospace Engineering

Supervisor: Professor André Calado Marta

Examination Committee

Chairperson:	Professor Filipe Szolnoky Ramos Pinto Cunha
Supervisor:	Professor André Calado Marta
Member of the Committee:	Professor Afzal Suleman

December 2014

Dedicated to my family

Acknowledgments

First of all, I want to express my gratitude for my supervisor Professor André Marta for his total dedication since our first talk to the final presentation of this thesis. His large knowledge was definitely the key to guide me through this task. Also to Professor Luís Eça for his pertinent and helpful advices and Doctor João Baltazar for kindly providing his PhD thesis and his results which were determinant to the validation of my aerodynamic calculations.

I want to express my great thanks to my family for their unconditional and essential support, encouragement and help during all my studies and also during the elaboration of this thesis. Without that I would not be in this situation right now.

I would like to thank my girlfriend for cheering me up in the darkest hours and for being always a supportive force while I was doing this work.

Also very important were my colleagues at Instituto Superior Técnico, because nobody can be successful in a degree alone. Special thanks go to my closest friends Pedro Sousa, Miguel Rita and João Clemente.

To IST and all my teachers I have to leave a word of appreciation for developing my technical knowledge, my analytical thinking, my resilience and all my abilities as an engineer and as a person.

Resumo

Fenómenos aeroelásticos envolvem o estudo da interação entre as forças aerodinâmicas e elásticas (aeroelasticidade estática), e entre forças aerodinâmicas, inerciais e elásticas (aeroelasticidade dinâmica). Estruturas aeroespaciais modernas, usando cada vez mais componentes de materiais compósitos, podem ser muito flexíveis, tornando o estudo aeroelástico um aspecto importante do projecto de aeronaves.

Flutter é uma instabilidade dinâmica aeroelástica caracterizada por oscilações da estrutura, provenientes da interação entre as três forças referidas actuando no corpo. O presente trabalho pretende estudar o comportamento de flutter em asas subsónicas tri-dimensionais, usando um método computacionalmente eficiente. Para isso, uma nova rotina computacional de aeroelasticidade foi criada utilizando um método dos paineis para resolver o escoamento assumido como sendo potencial e um programa comercial para análise estrutural. A validação do método dos paineis é feita usando dados experimentais de túnel de vento, enquanto o programa comercial é verificado utilizando testes disponíveis. O acoplamento dos dois domínios é feito com um *script* principal, usando um esquema de discretização temporal adequado.

Os resultados são apresentados para um exemplo de uma asa que é denominada o caso referência. Mais tarde, um estudo da influência dos parâmetros pertinentes é executado, concluindo com a comparação entre os vários valores testados. Em conclusão, a rotina demonstra bons resultados, tendo em conta as influências previstas pela teoria dos parâmetros estudados. Apesar da simplificação do escoamento, assumido potencial, este método demonstra ser uma ferramenta muito útil no projecto preliminar de aeronaves.

Palavras-chave: Aeroelasticidade, Método dos paineis, Interação fluido-estrutura, Método de Elementos Finitos, *Flutter*, Velocidade de divergência.

Abstract

Aeroelasticity phenomena involve the study of the interaction between aerodynamic and elastic forces (static aeroelasticity), and aerodynamic, inertial, and elastic forces (dynamic aeroelasticity). Modern aircraft structures, making more and more use of lightweight composite structures, may be very flexible making the aeroelastic study an important aspect of the aircraft design.

Flutter is a dynamic aeroelastic instability characterized by sustained oscillation of structure arising from interaction between those three forces acting on the body. The present work aims to study the flutter behavior on three-dimensional subsonic aircraft wings, using a computationally efficient method. For that, a new computational aeroelasticity design framework was created using a panel method to solve the fluid flow approximated as potential flow and a commercial software for the structural analysis. A validation of the fluid solver is made using wind tunnel data, while the structure solver is verified using the available tests. The coupling of the two domains is made with a main script using an adequate time discretization scheme.

The results are presented for a wing example which is denoted as reference case. Later, a study of the influence of pertinent parameters is performed, concluding with the comparison between the many values tested. It is concluded that the framework shows very good agreement to the theoretical influences of the parameters studied. Despite the simplification of the fluid flow, which was assumed to be potential, this method proves to be a very useful tool in aircraft preliminary design.

Keywords: Aeroelasticity, Panel method, Fluid-structure interaction, Finite element method, Flutter, Divergence velocity.

Contents

List of Tables

List of Figures

Nomenclature

Reference Frames

(l, m, n) Local frame at the collocation point of the panel.

(s, t, r) Local frame at the centroid of the element.

(X, Y, Z) Global inertial frame.

(x, y, z) Frame fixed to the body, Cartesian coordinates.

Greek symbols

α	Angle of attack, Newmark integration parameter.
β	Mass matrix multiplier.
γ	Amplitude decay factor.
Δ	Variation.
δ	Stiffness matrix multiplier, Newmark integration parameter.
$\vec{\epsilon}$	Elastic Strain vector.
$\vec{\zeta}$	Vorticity vector.
θ	Structural rotation angle.
$\vec{\Theta}$	Orientation of the body-fixed coordinate system in relation to the inertial system having components (ϕ, θ, ψ).
Λ	Circulation.
λ	Bulk viscosity coefficient.
μ	Molecular viscosity coefficient, doublet strength.
ν	Poisson ratio.
ξ	Fraction of critical damping.
π	Mathematical constant.

ρ Density.

σ Source strength or volumetric rate.

$\vec{\sigma}$ Stress vector.

τ Stress tensor.

ω Natural frequency.

$\vec{\Omega}$ Rate of rotation of the body-fixed frame, having components (p, q, r).

$\vec{\omega}$ Angular velocity.

Φ Velocity potential.

$\vec{\phi}$ Mode shape.

Mathematical Operations

∇ Differential operator.

∂ Partial derivative.

$\int$ Integral.

$\sum$ Summation.

$\cdot$ Dot or inner product.

$\times$ Vector or cross product.

Roman symbols

$\mathcal{AR}$ Wing aspect ratio.

a Constant.

B Strain-displacement matrix.

C Structural Damping matrix, closed curve.

C_D Drag coefficient.

C_L Lift coefficient.

C_M Moment coefficient.

C_p Pressure coefficient.

D Elastic Stiffness matrix.

D_i Lift-induced drag force.

E Young's modulus, Potential function.

e	Internal energy per unit mass.
$\vec{F}$	Applied Load matrix.
$\vec{f}$	External forces vector.
G	Shear modulus.
K	Structural Stiffness matrix.
k	Thermal conductivity.
M	Structural Mass matrix.
$\vec{n}$	Unity vector normal to a surface.
N	Shape functions matrix.
p	Pressure.
$\dot{q}$	Rate of volumetric heat addition per unit mass.
$\vec{R}$	Location of a point in the inertial system.
R	Specific gas constant.
Re	Reynolds number.
S	Open surface.
Δt	Time step size.
t	Time.
T	Temperature.
$\vec{u}$	Structural displacement vector.
$\dot{\vec{u}}$	Structural velocity vector.
$\ddot{\vec{u}}$	Structural acceleration vector.
$\vec{\mathcal{U}}$	Structure state vector.
vol	Volume element.
$\vec{V}$	Fluid velocity vector with components (u, v, w).
$\vec{\mathcal{W}}$	Fluid state vector.
$\vec{w}$	Displacement vector of a general point.
$\vec{x}$	Structural displacement vector in the fluid domain.
y_i	Modal coordinates.

Subscripts

e	Discretization element.
∞	Free stream condition.
i	Mode number, internal.
k	Panel number.
L	Lower side.
n	Normal component, Time station.
ref	Reference condition.
U	Upper side.
W	Wake.

Superscripts

*	Total.
t	Time step.

Glossary

ALE	Arbitrary Lagrangian-Eulerian is a frame of reference formulation used for FSI problems.
APDL	ANSYS Parametric Design Language is a commercial software used to perform structural analysis.
BE	Backward Euler scheme for implicit first order time discretization
CAE	Computer-Assisted Engineering is the group of computational tools that support the work of the engineer (namely calculations and simulations).
CFD	Computational Fluid Dynamics is a branch of fluid mechanics that uses numerical methods and algorithms to solve problems that involve fluid flows.
CN	Crank-Nicholson scheme for implicit second order time discretization
CPU	Central Processing Unit of a computer.
CSM	Computational Structural Mechanics is a branch of structure mechanics that uses numerical methods and algorithms to perform the analysis of structures and its components.
CSS/ISS	Conventional/Improved Serial Staggered schemes are two procedures for fluid-structure coupling.
DOF	Degrees of Freedom are the number of variables in the system which vary independently. Particularly in mechanics, it represents the number of independent motions allowed to the body.

FORTRAN	Formula Translating System is a programming language.
FSI	Fluid-Structure Interaction refers to the phenomena involved in the interaction of a movable or deformable structure with an internal or surrounding fluid flow.
LE	Leading Edge of a wing is the part that first contacts the air
MATLAB	Matrix Laboratory is a high-level language and interactive environment for numerical computation, visualization, and programming.
NACA	Series of airfoil shapes developed by the National Advisory Committee for Aeronautics.
NS	Full Navier-Stokes flow governing equations
TE	Trailing Edge of a wing is the rear edge where the flow rejoins
XFOIL/XFLR5	Free-ware programs developed for aerodynamic analysis of airfoils and wings, respectively.

Chapter 1

Introduction

1.1 Motivation

Structural analyses constitute a crucial part in Aircraft Design. Since the primordials of the aviation history, it was stated that the success of the air vehicle is dependent on a structure capable of withstanding the several loads encountered in each flight and a strong propulsion system. Moreover, both components should be as light as possible.

In the beginning of the 20th century, with the World War I, research efforts were made to have reliable war aircrafts. By then, structures were tested with hanged sand bags and designed accordingly to these static loads. The technology and knowledge available were not enough even to think in dynamic loads.

As it will be defined later, *aeroelasticity* is the science that studies the mutual interaction between elastic, inertial and aerodynamic forces, and the influence of this interaction in the behavior of a body.

Figure 1.1: Picture of the Fokker D8 (or D VIII) used to demonstrate its strength [3]

The first known flight accident caused by aeroelastic circumstances already occurred prior the first flight of the Wright Brothers on December 9, 1903 [11]. The wings of the monoplane dismounted after a catapult take-off. Later, the model Fokker D-8 (Figure 1.1), considered to have superior performance,

excellent strength and structural rigidity in German Air Force tests, was not in combat more than a few days before wing failures repeatedly occurred in high-speed dives [12]. It was later discovered that both accidents were caused by a static torsion divergence of the wing, an aeroelastic phenomenon.

One hundred years later, aeroelasticity is still a major field of study in aerospace engineering. Aeroelastic phenomena in modern high-speed aircraft have profound upon the design of structural members and also upon mass distribution, lifting surface planforms and control system design [12].

Nowadays, the goal is to be able to perform accurate computational aeroelastic tests, that can be applied in early stages of the design phase. By increasing the accuracy and feasibility of computational tools, one can decrease the number of experimental tests needed, which largely reduces the design cost. Also, applications of the aeroelastic phenomena are found in several other disciplines, as it will be exposed later.

1.2 Aeroelasticity

Some authors define *Aeroelasticity* as a part of Aeronautical Engineering, for example Bisplinghoff et al. [12] and Megson [5]. However, this term as evolved to many application areas and some authors even mention the word 'aeroelastician' for the specialist in this field, namely Clark et al. [13] or Ashley and Zartarian [14]. A general (but complete) definition is the one from Hirschel et al. [11]:

The science of aeroelasticity encompasses those physical processes and problems that result from the interaction between elasto-mechanical systems and the surrounding airflow.

To help visualizing the context of the term, Collar [4] used a representation in triangle, presented in Figure 1.2.

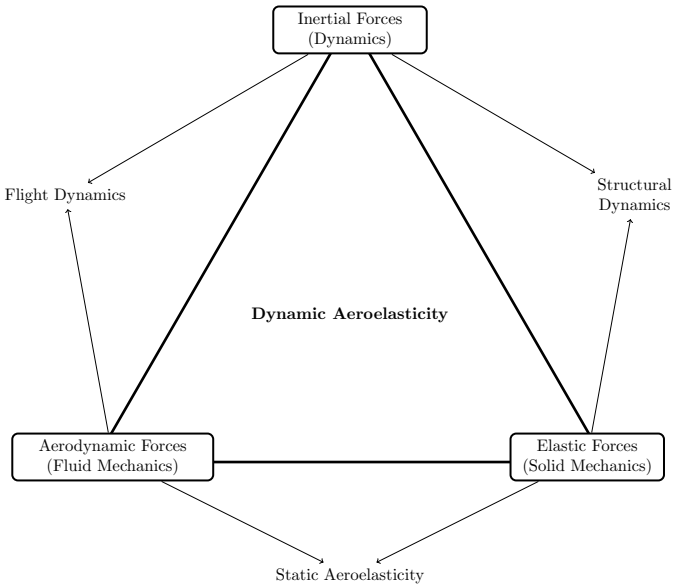

Figure 1.2: Collar triangle (adapted from the original diagram presented in [4]).

By pairing two of the three corners of the triangle, one can identify other important disciplines. For example,

- Aerodynamics + dynamics = aerodynamic stability;
- Dynamics + solid mechanics = structural dynamics;
- Aerodynamics + solid mechanics = static aeroelasticity.

In some sense, all these technical fields may be considered special cases of aeroelasticity. However, for dynamic aeroelastic effects to occur, all three forces are required.

Although this concept was pioneered in aeronautical applications, soon it became important for other areas like civil engineering, e.g. flows about bridges and tall buildings; mechanical engineering, e.g. turbomachinery blades and Formula 1 racing cars; and nuclear engineering, e.g. flows about fuel elements and heat exchanger vanes.

In the coming subsections, the different types of aeroelastic problems will be presented.

1.2.1 Static Problems

When dealing with steady aerodynamics from elastic bodies, the interaction between both aerodynamic and elastic forces may exhibit divergent tendencies in a very flexible structure, eventually leading to failure. If on the other hand, it is adequately stiff, a stable equilibrium is reached.

The static aeroelastic problems are located outside the triangle at the bottom side of Figure 1.2. Overall, these problems can be classified as: *Divergence*, *Aileron Effectiveness*, *Distribution of Lift* and *Static Flight Stability* [11].

Divergence happens when a lifting system is, after reaching a critical velocity, abruptly deformed up to fracture.

Considering the simple case of the wing in Figure 1.3, when the speed increases, so does the lift force and the torsion moment about the center of twist. This makes the local angle of attack increase, which also causes the lift to increase. Above a certain limit velocity, the *divergence speed*, the structure torsional rigidity is not enough to balance the aerodynamic moment and it becomes unstable. This problem is addressed as *Torsional Divergence*. Other divergences could theoretically occur, but this one is historically the critical one.

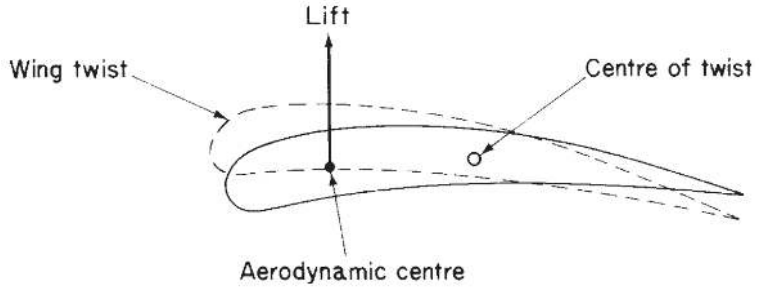

Figure 1.3: Increase of wing angle due to twist moment [5].

Another case happens in the presence of the roll movement controls, the *ailerons*, which cause an additional lift in the wing tip near the trailing edge. If the aileron deflects in such a way that the extra lift points up, it also creates an additional moment causing a nose-down twisting and a local angle

decreasing. So the effectiveness of the control surface is affected. Here again when a particular velocity is reached, the *Aileron Reversal Speed*, the aileron deflection does not produce any rolling moment at all.

Finally the *Distribution of Lift* is about the effect of an elastic deformation on the aerodynamic pressure distribution, which is naturally implicit in the divergence problem and the *Static Flight Stability* deals with the effect of the elastic deformation in the controllability of the aircraft, namely the static margin or the control behavior.

1.2.2 Dynamic Problems

When the situation becomes time-dependent, one enters in the area of *dynamic aeroelasticity* which is more related with unstable structure oscillation.

Flutter has perhaps the most far-reaching effects on high-speed aircraft [12]. The *classical* type of flutter is associated with potential flow and usually, involves coupling of two or more degrees of freedom (DOF). The *nonclassical* type of flutter may involve separated flow, turbulence and stalling conditions.

In Figure 1.4, several possible dynamic aeroelastic problems are assembled, where *SDOF* stands for Single DOF. Those happen when a single mode goes unstable due to non-linearities [15].

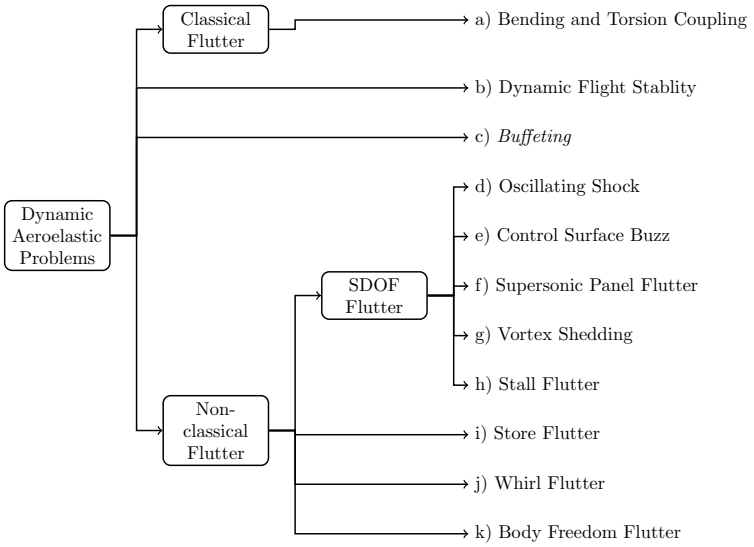

Figure 1.4: Diagram showing the different possible dynamic aeroelastic problems.

A small description of each problem comes next:

a) Bending and torsion coupling: this is the typical two DOF flutter in which there is a coalescence of flexural and torsional modes. Pure bending or pure torsional oscillations are quickly damped out, but combined and 90° out of phase, they cause the abruptly self-excited flutter [5].

b) Dynamic flight stability: this section refers simply to the influences of elastic deformations of the structure on dynamic airplane stability [12].

c) *Buffeting*: it is produced most commonly in a tailplane by eddies caused by poor airflow in the wing wake. If the frequency of these is equal to the natural frequency of the tail, a resonant oscillation

can happen [5].

d) Oscillating shock: non-linear effects of the compressible flow, with the presence of unstable shock waves (see for example [16]).

e) Control surface buzz: this phenomenon is also a shock wave (though here in transonic regime) which is located near one hinge, forward of a control surface. The deflection of the surface causes the intensity of the shock to change and, consequently, also the pressure on the boundary layer behind the shock. The result is a sucking/pushing effect on the control and possibly an undamped oscillation [5].

f) Supersonic panel flutter: panel flutter is the self-excited oscillation of the external skin of a flight vehicle when exposed to airflow along its surface. At supersonic speeds, the skin panel temperature can reach several hundred degrees, which cause large thermal deflections [17].

g) Vortex shedding: phenomenon typically known from flows around circular cylinder bodies, which for increasing velocity, the wake starts to be unstable and fluctuations of the vorticity cause the *Von Kármán vortex street*. The forces and moments on the body fluctuate together with the flow and vibrations are induced in the body. It is important because it can also happen, for example, in turbine blades with high angles of attack [18].

h) Stall flutter: it occurs at a high incidence when the blades or wings are highly loaded (near stall) and experience off-design conditions, which may cause self-inducted divergent oscillations [19].

i) Store flutter: when large external bodies, such as engine nacelles, fuel tanks or guns are added to the wing of an aircraft, dynamic characteristics, in particular the flutter speed, may be adversely affected [20].

j) Whirl flutter: this problem is normally associated with tiltrotor aircraft (see Figure 1.5), which when in high-speed axial flight, the high inflow through the rotor generates large in-plane forces. These forces can interact with the pylon/wing motion making the system unstable [21].

Figure 1.5: The Bell-Boeing V-22 Osprey tiltrotor in axial flight [6].

k) Body freedom flutter: the body freedom flutter (BFF) happens mostly on the lifting surfaces and results from coupling of the rigid body longitudinal dynamic mode called *short-period mode* with the wing bending [22].

1.3 Computer-Assisted Engineering

Through the years, design engineers have always had two main concerns: to obtain the best possible solution for their problems and to do it in the least amount of time. Experimental testing have always produced the most reliable results to any industry application. The problem is that they are expensive and time-consuming. For this reason, together with mathematicians and physicists, engineers have been developing theoretical approaches to correctly treat the problems and their constraints, to obtain acceptable results at much less expenses. The key point on this was the appearance from digital computers since most of the practical applications are humanly impossible to resolve.

A new concept was then created: the *Computer-Assisted Engineering* (CAE). It refers to the ensemble of simulation tools that support the work of the engineer between the initial design phase and the final definition of manufacturing process.

Among several branches of these tools, two are here emphasized: *Computational Solid Mechanics* (CSM) and *Computational Fluid Dynamics* (CFD). The former evaluates many parameters from solid bodies, for instance mechanical stresses, deformations, vibration modes, failure limits and thermal flow. The latter designates the software tools that allow the analysis of the fluid flow, where fluid can be any substance or mixture in liquid or gas state. The parameters here can be velocity, stresses in walls and thermodynamic variables (such as pressure, temperature, density and energy).

When applying the CAE concept in a dynamic aeroelasticity problem, which is the case of this work, both CSM and CFD simulations are needed. The decisions and approximations made in each of them will influence the other and, consequently, the final solution. This coupling is called the *Fluid-Structure Interaction*, which will be handled later.

1.4 Aircraft Wing

Like it was mentioned before, since the beginnings of the aviation history, efforts were made to decrease the wing weight while maintaining or even increasing its strength. To achieve this goal, the solution was to use a structure composed by elements, similar to a truss, covered by a layer which keeps the aerodynamic effectiveness of the wing. Nowadays, most of the aircraft wing follow a standard structure as illustrated in Figure 1.6.

The main structural parts are then spars, ribs, stringers and the skin. Then, accordingly to the application, one can change their materials, quantity, location and so on.

In this work, a simplified structure is used with only two spars and a skin. The skin will then be thicker to compensate the absence of stringers and the spars can be moved forward and backward to manipulate the torsional characteristics of the wing.

1.5 Objectives

The objectives of this work are then to review the actual models and methods to compute aeroelastic calculations, state the governing equations and acceptable approximations, and to apply some of these

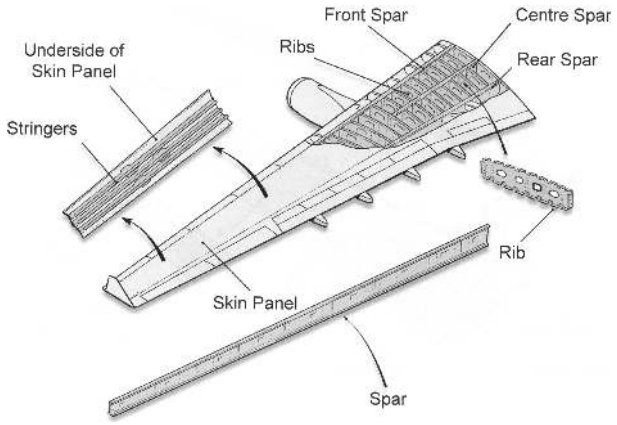

Figure 1.6: Illustration of a standard aircraft wing structure [7].

methods to perform aeroelastic studies of aircraft wings.

For these studies, an available tool for structural analysis is employed (CSM), while the aerodynamic (CFD) and coupling tools are to be created and merged in a computational program. The final result is an aeroelastic design framework for subsonic aircraft wings.

1.6 Thesis Outline

This work is divided in three main stages: the theoretical bases (Chapters 2, 3 and 4), the practical application on computational analyses (Chapters 5, 6 and 7) and, finally, the results and conclusions (Chapters 8, 9 and 10).

In Chapter 2, the fundamental theory about the structural analysis and the available options from the chosen commercial software are covered. Chapter 3 is much bigger because this is the part of the framework which is developed from scratch. Fluid mechanics theory is therefore presented, the needed approximations are justified and a panel method formulation is issued. Chapter 4 results from a literature review about the fluid-structure interaction problems, where some procedures are presented together with particularities of this subject.

At this stage, the theory is applied in the same order as the previous one. Chapter 5 presents some verification tests and a mesh convergence study, while also issuing some remarks about the computational problem setup. Chapter 6 addresses all the development stages before arriving to the final fluid solver. Also here some tests were made to validate the method and its application. In Chapter 7, one will enter into the practical details of the final product, the aeroelastic framework, namely the inputs specification, the pre-processing, the time cycle and the post-processing.

The results start then in Chapter 8 with some explanations about the choices made, then presenting the reference input values and a dynamic and static computation. In Chapter 9, several further computations are performed with different values and compared to the reference case.

Chapter 2

Structural Analysis

In this chapter, the mathematical description of the structural motion is briefly made. Since by condition the structure solver is already decided to be ANSYS Parametric Design Language (APDL), only the theory applied to this work is presented, together with some particularities of the solver. That information is based on the *Ansys* software manual [23].

The fundamental theory behind APDL for structures is the *Principle of Virtual Work* which states that *if a particle is in equilibrium, the total virtual work of the forces acting on the particle is zero for any virtual displacement of the particle* [24]. In the same way, a virtual change of the internal energy must be offset by an identical change in external work due to the applied loads.

2.1 Structural Fundamentals

In the case of linear materials, the stress is related to the strains by

$$\vec{\sigma} = D\vec{\epsilon}, \tag{2.1}$$

where $\vec{\sigma}$ is the stress vector, $\vec{\epsilon}$ is the elastic strain vector and D is the elasticity or elastic stiffness matrix or stress-strain matrix, defined as

$$D^{-1} = \begin{bmatrix} 1/E_x & -\nu_{xy}/E_x & -\nu_{xz}/E_x & 0 & 0 & 0 \\ -\nu_{yx}/E_y & 1/E_y & -\nu_{yz}/E_y & 0 & 0 & 0 \\ -\nu_{zx}/E_z & -\nu_{zy}/E_z & 1/E_z & 0 & 0 & 0 \\ 0 & 0 & 0 & 1/G_{xy} & 0 & 0 \\ 0 & 0 & 0 & 0 & 1/G_{yz} & 0 \\ 0 & 0 & 0 & 0 & 0 & 1/G_{xz} \end{bmatrix}. \tag{2.2}$$

This matrix is presumed to be symmetric. E_i is the Young's modulus in the i direction, ν_{ij} is the Poisson ratio and G_{ij} is the shear modulus in the ij plane.

2.2 Transient Analysis

The transient dynamic equilibrium equation is, for a linear structure, as follows

$$M\ddot{\vec{u}} + C\dot{\vec{u}} + K\vec{u} = \vec{F}, \tag{2.3}$$

where M represents the structural mass matrix, C the structural damping matrix, K the structural stiffness matrix, $\ddot{\vec{u}}$ the nodal acceleration vector, $\dot{\vec{u}}$ the nodal velocity vector, $\vec{u}$ the nodal displacement vector and $\vec{F}$ the applied load vector.

For each discretization element e, different matrices M_e, C_e and K_e are defined. The full derivation using the principle of virtual work is presented in [23], here one will just refer the main results.

The strain vector $\vec{\epsilon}$ is related with the displacement vector $\vec{u}$ by $\vec{\epsilon} = B\vec{u}$, where B is called the strain-displacement matrix. With this, one can obtain the element stiffness matrix as

$$K_e = \int_{vol} B^T D B d(vol). \tag{2.4}$$

Defining N as the matrix of shape functions, which relates the vector of displacements of a general point $\vec{w}$ with the nodal displacement by $\vec{w} = N\vec{u}$, the element mass matrix is defined as

$$M_e = \rho \int_{vol} N^T N d(vol). \tag{2.5}$$

The structural damping matrix C is composed by the contribution of many factors, which will differ depending on the type of dynamic analysis (harmonic, damped modal and transient), on the approximations of each analysis, on the elements used, on the material used, etc. Further explications and equations for the damping matrix can be consulted in [23].

2.3 Time Discretization Scheme

To perform a time-dependent analysis, the equations of motion need to be discretized in the time domain and that can be done in many ways. APDL includes two possible time integration procedures: the explicit central differences method and the implicit Newmark method (with an improved algorithm called HHT) [23].

Applying the Newmark method to Equation (2.3) results in

$$\left(a_0 M + a_1 C + K\right)\vec{u}_{n+1} = \vec{F} + M\left(a_0\vec{u}_n + a_2\dot{\vec{u}}_n + a_3\ddot{\vec{u}}_n\right) + C\left(a_1\vec{u}_n + a_4\dot{\vec{u}}_n + a_5\ddot{\vec{u}}_n\right), \tag{2.6}$$

where

$$a_0 = \frac{1}{\alpha \Delta t^2}, \qquad a_1 = \frac{\delta}{\alpha \Delta t},$$
$$a_2 = \frac{1}{\alpha \Delta t}, \qquad a_3 = \frac{1}{2\alpha} - 1,$$
$$a_4 = \frac{\delta}{\alpha} - 1, \qquad a_5 = \frac{\Delta t}{2}\left(\frac{\delta}{\alpha} - 2\right),$$
$$a_6 = \Delta t\,(1-\delta), \qquad a_7 = \delta \Delta t.$$

As documented in [23], this scheme is unconditionally stable for

$$\alpha \geq \frac{1}{4}\left(\frac{1}{2} + \delta\right)^2, \qquad \delta \geq \frac{1}{2}, \qquad \frac{1}{2} + \delta + \alpha > 0, \tag{2.7}$$

where α and δ are the Newmark integration parameters and are related to the amplitude decay factor γ by $\alpha = \frac{1}{4}(1+\gamma)^2$ and $\delta = \frac{1}{2} + \gamma$.

The HHT method is a further refinement which basically adds controlled numerical damping to reduce the numerical noise, while not losing solution accuracy. Further derivation can be found in [23].

The nature of a transient aeroelastic computation, where the fluid loads applied on the structure are constantly varying, makes it important to have some attention on the way physical time is managed. Particularly, the time step size Δt can be set to a constant through out the simulated total physical time. Alternatively, APDL has also an *Automatic Time Stepping* which predicts the next time step size, using the information of the previous computations.

2.4 Solution Method

Three methods are available in APDL to solve the Equation (2.6): the full, reduced and mode superposition.

Full Solution Method

This method simply solves Equation (2.6) with no additional assumptions. In the case of a nonlinear analysis, the typical Newton-Raphson method is employed.

Reduced Solution Method

Hereby reduced structure matrices are used to solve Equation (2.3) for linear structures. The following conditions are imposed:

1. Constant M, C and K matrices. This implies no large deflections or change of stress stiffening;
2. Constant time step size;
3. No element load vectors. This implies no pressures, which means that only nodal forces are permitted;

4. Nonzero displacements may be applied only at master a DOF.

This method has the big advantage that it usually runs faster then the full method, mainly because the left-hand side of Equation (2.6) is inverted only once.

Mode Superposition Method

This method uses the natural frequencies and mode shapes of a linear structure to predict the response. In this case the restrictions are:

1. Constant M and K matrices. This implies no large deflections or change of stress stiffening;

2. Constant time step size;

3. There are no element damping matrices. However, various types of system damping are available;

4. Time varying imposed displacements are not allowed.

Having defined previously n modes to calculate, the displacement vector is $\vec{u} = \sum_{i=1}^{n} \vec{\phi}_i y_i$, where $\vec{\phi}_i$ is the mode shape of mode i and y_i the respective modal coordinates.

Then for each mode the equation of motion is only

$$\ddot{y}_i + 2\omega_i \xi_i \dot{y}_i + \omega_i^2 y_i = f_i, \tag{2.8}$$

where ω_i is the natural frequency of mode i, ξ_i is the fraction of critical damping and $f_i = \vec{\phi}_i^T \vec{F}$ represents the right-hand side of (2.3), in this form for convenience.

2.5 Geometric Definitions

To model any geometry in APDL, it contains a list of many available types of elements, for instance, beams, links, pipes, solids and shells. For each type, several parameters are required and several levels of approximation are available, which must be careful chosen by the user.

Herein the element SHELL181 [23] will be presented. It is suitable for analyzing thin structures (when one dimension is much smaller than the other two), the so called shells. It is a four-node quadrilateral element (see Figure 2.1) with six DOF at each node: translations in the x, y, and z directions and rotations about the x, y and z-axes. It also accounts for effects of distributed pressures.

To each element, one thickness and one material is attributed, unless one wants to study a multilayer shell (composite materials).

Several reference frames are defined in Figure 2.1. (X, Y, Z) is the global system of the problem, (x, y, z) is the frame fixed with the body to describe the rotation and (s, t, r) is the local frame at the centroid of the element.

To address the variables and their variation along the structure, APDL elements have associated *shape functions*. In the case of this element, it uses the local frame to interpolate the variations through it,

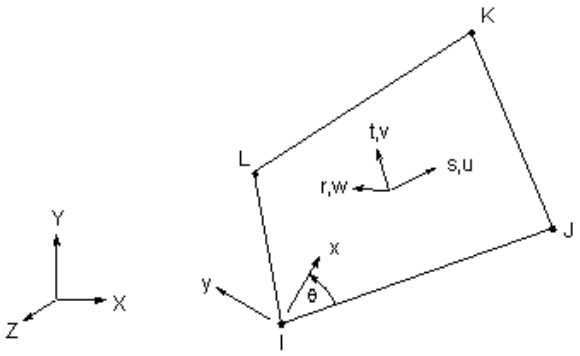

Figure 2.1: 3D four-node quadrilateral shell element and its local frames.

where

$$I = (-1, -1, 0)\ ,\ J = (1, -1, 0)\ ,\ K = (1, 1, 0)\ ,\ L = (-1, 1, 0). \tag{2.9}$$

Then all the displacements (u, v, w), rotations $(\theta_x, \theta_y, \theta_z)$, velocities (V_x, V_y, V_z) and other variables are described as

$$\begin{aligned} u &= \frac{1}{4}\left[u_I(1-s)(1-t) + u_J(1+s)(1-t) + u_K(1+s)(1+t) + u_L(1-s)(1+t)\right], \\ \theta_x &= \frac{1}{4}\left[\theta_x(1-s)(1-t) + \theta_x(1+s)(1-t) + \theta_x(1+s)(1+t) + \theta_x(1-s)(1+t)\right], \\ V_x &= \frac{1}{4}\left[V_I(1-s)(1-t) + V_J(1+s)(1-t) + V_K(1+s)(1+t) + V_L(1-s)(1+t)\right], \end{aligned} \tag{2.10}$$

for the case of the displacement, rotation and velocity in the x direction. All the other variables are determined analogically. As it can be inferred from Equation (2.10), the element SHELL181 is a bi-linear element, since the underlying shape functions are linear in both directions s and t.

Chapter 3

Aerodynamic Analysis

3.1 Governing Equations of Fluid Dynamics

When studying any kind of fluid motion, regardless of the fluid, one has to state the fundamental governing equations which describe the evolution of the fluid flow - the continuity, momentum and energy equations. They are mathematical statements of three physical principles, respectively:

- Mass conservation;
- Newton's second law (momentum conservation);
- Energy conservation.

It is important to define the concept of *conservation* of a quantity. It means that whatever mechanisms occur in the fluid movement, the quantity does not change its value. Talking for example about energy, it cannot be destroyed or created. Instead it is converted or transformed (e.g. from kinetic to thermal energy).

Those mathematical equations, are then transformed using some fluid properties and particularities (example of types of forces on fluids, body forces and surface forces). For real viscous fluids, the resultant system of equations is referred as the *Navier-Stokes* (NS) equations. The derivation of these equations is not pertinent in this work, so only the final form of the 3D NS equations in conservative form is presented here. For more details consult Anderson et al. [25].

$$\frac{\partial \rho}{\partial t} + \nabla \cdot \left(\rho \vec{V}\right) = 0, \tag{3.1a}$$

$$\begin{cases} \frac{\partial \rho u}{\partial t} + \nabla \cdot \left(\rho u \vec{V}\right) = -\frac{\partial p}{\partial x} + \frac{\partial \tau_{xx}}{\partial x} + \frac{\partial \tau_{yx}}{\partial y} + \frac{\partial \tau_{zx}}{\partial z} + \rho f_x \\ \frac{\partial \rho v}{\partial t} + \nabla \cdot \left(\rho v \vec{V}\right) = -\frac{\partial p}{\partial y} + \frac{\partial \tau_{xy}}{\partial x} + \frac{\partial \tau_{yy}}{\partial y} + \frac{\partial \tau_{zy}}{\partial z} + \rho f_y \\ \frac{\partial \rho w}{\partial t} + \nabla \cdot \left(\rho w \vec{V}\right) = -\frac{\partial p}{\partial z} + \frac{\partial \tau_{xz}}{\partial x} + \frac{\partial \tau_{yz}}{\partial y} + \frac{\partial \tau_{zz}}{\partial z} + \rho f_z \end{cases}, \tag{3.1b}$$

$$
\begin{aligned}
&\frac{\partial}{\partial t}\left[\rho\left(e+\frac{V^2}{2}\right)\right]+\nabla\cdot\left[\rho\left(e+\frac{V^2}{2}\right)\vec{V}\right] \\
&\quad=\rho\dot{q}+\frac{\partial}{\partial x}\left(k\frac{\partial T}{\partial x}\right)+\frac{\partial}{\partial y}\left(k\frac{\partial T}{\partial y}\right)+\frac{\partial}{\partial z}\left(k\frac{\partial T}{\partial z}\right) \\
&\qquad-\frac{\partial up}{\partial x}-\frac{\partial vp}{\partial y}-\frac{\partial wp}{\partial z}+\frac{\partial u\tau_{xx}}{\partial x}+\frac{\partial u\tau_{yx}}{\partial y}+\frac{\partial u\tau_{zx}}{\partial z} \\
&\qquad+\frac{\partial v\tau_{xy}}{\partial x}+\frac{\partial v\tau_{yy}}{\partial y}+\frac{\partial v\tau_{zy}}{\partial z} \\
&\qquad+\frac{\partial w\tau_{xz}}{\partial x}+\frac{\partial w\tau_{yz}}{\partial y}+\frac{\partial w\tau_{zz}}{\partial z}+\rho\vec{f}\cdot\vec{V},
\end{aligned}
\tag{3.1c}
$$

where

- From (3.1a) to (3.1c) they are the mathematical expression of the mass, momentum and energy conservation, respectively;

- ρ, p and T are the density, pressure and temperature, respectively, scalar functions of both time and space;

- $\vec{V}=(u,v,w)$ is the vector velocity field. Here u, v and w are the velocity components in the x, y and z directions, respectively, which are scalar functions both of time and space;

- τ_{ij} is the stress tensor. The convention is that τ_{ij} denotes a stress in the j-direction exerted on a plane perpendicular to the i-axis. For *Newtonian* fluids (in which the shear stress is proportional to the time-rate-of-strain), it comes

$$
\tau_{ij}=\begin{bmatrix}
\lambda\nabla\cdot\vec{V}+2\mu\frac{\partial u}{\partial x} & \mu\left(\frac{\partial v}{\partial x}+\frac{\partial u}{\partial y}\right) & \mu\left(\frac{\partial u}{\partial z}+\frac{\partial w}{\partial x}\right) \\
- & \lambda\nabla\cdot\vec{V}+2\mu\frac{\partial v}{\partial y} & \mu\left(\frac{\partial w}{\partial y}+\frac{\partial v}{\partial z}\right) \\
- & - & \lambda\nabla\cdot\vec{V}+2\mu\frac{\partial w}{\partial z}
\end{bmatrix},
\tag{3.2}
$$

  being λ the bulk viscosity coefficient and μ the molecular viscosity coefficient;

- $\vec{f}$ is the vector of the external forces;

- $\dot{q}$ is the rate of volumetric heat addition per unit mass;

- e is the internal energy per unit mass;

- k is the thermal conductivity.

Equations (3.1a) to (3.1c) form a system of non-linear partial different equations, and hence very difficult to solve analytically. To date, there is no general closed-form solution to these equations. So, to be able to apply the equations to obtain numerical results, approximations adequate to the case of the flow in study have to be made.

3.2 Levels of Approximation

The equations presented in Section 3.1 contain many levels of complexity:

- They form a system of five fully coupled time-dependent partial differential equations and seven unknowns, ρ, p, T, u, v,w and e;
- To close the system two more equations are needed. One is the equation of state ($p = \rho RT$ for a perfect gas where R is the specific gas constant) and another thermodynamic relation, for example, $e = e(T, p)$;
- Each of the equations is nonlinear. This nonlinearities cause many well-known physical effects, such as turbulence or shock waves. Also, they lead to non-unique solutions, which means that two flows with the same boundary conditions can have different configurations.

CFD is then, in part, "the art of replacing the governing equations with numbers" [25] and obtain a numerical description of the flow field. Normally, CFD solutions require manipulations of millions of numbers, so the aid of a computer is primal.

A CFD simulation system can be divided in five main steps:

1. Selection of the mathematical model, with the adequate approximations;
2. Discretization of the space and equations, defining the numerical scheme;
3. Stability and accuracy of the scheme analysis;
4. Solve using appropriate time integration and matrix manipulation methods;
5. Post-processing and interpretation of the simulation results.

Starting with the first step, it is now time to explore the many approximations for the flow motion. Figure 3.1 shows some of the possible formulations in a pyramid. As one steps down, the accuracy is lower but the computation cost also.

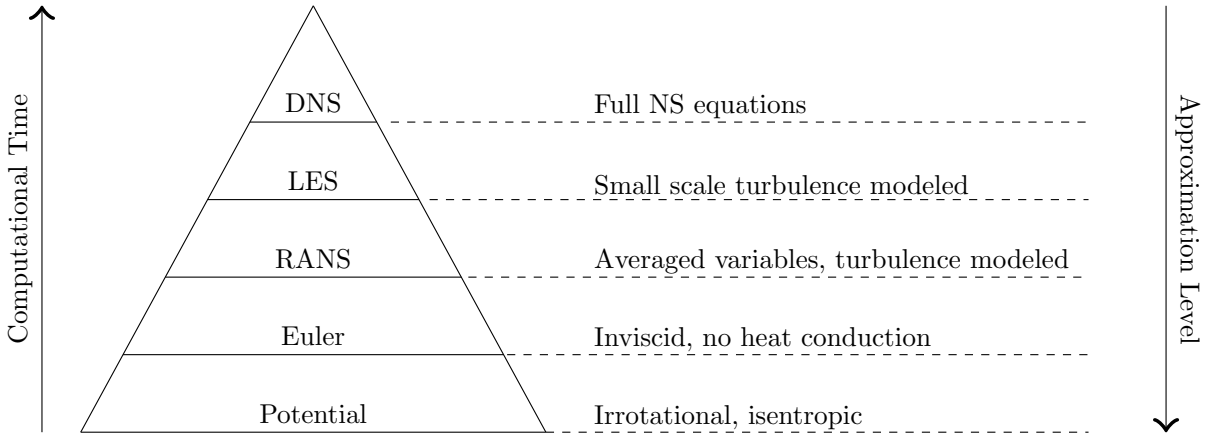

Figure 3.1: Levels of approximation of a fluid flow computation.

Direct Numerical Simulation

With the increasing computer power and memory, it is becoming progressively possible to numerically resolve the full Navier-Stokes equations. This is called the *Direct Numerical Simulation* or simply DNS.

Checking recent investigations in this area, one can see that simulations of boundary layers are already possible but for limited Reynolds (Re) numbers and using supercomputers. For instance in Borrell et al. [26], simulations of the boundary layer with zero pressure gradient and with artificial roughness are made for Re_θ maximum of 6 800 and 4 200, respectively. Here a supercomputer with 32 768 cores was used.

Therefore, DNS computations for realistic Re numbers such as the ones found in external flows around aircrafts, are still out of reach and so they will be for a long time [27]. However, the research on simpler problems is being useful to discover the fundamental mechanisms of turbulence and transition. For example in the paper from Lu and Liu [28], it was discovered that "large vortex breakdown", which was considered the last step of transition for years, is incorrect.

Large Eddy Simulation

The highest level of approximation is called *Large Eddy Simulation* (LES). The approach here is similar to the DNS, being only the small scales of the turbulent fluctuations modeled. All the rest is directly simulated. This method has good prospects for reaching the industry stage in the near future [27].

Bouffanais [29] recently made a resume of the evolution of this method through the last years and also its main characteristics and features. In Tan et al. [30] one can see a recent work on this area, a study of the flow in a pipe curve at $Re = 6 \times 10^4$.

Reynolds Averaged Navier-Stokes

The next level of approximation is the consideration of the averaged turbulent flow. Here the *Reynolds Averaged Navier-Stokes* equations (RANS) obtained by considering that each variable is the sum of an average value to a perturbation. The result is that some extra terms appear in the system of equations, the *Reynolds Stresses* which require the use of turbulence models.

It is also possible to use the RANS approach together with the LES, being the former applied near the walls and the latter in the outer flow. This is the hybrid RANS-LES formulation and one example of application can be seen in Davidson [31].

Inviscid Flow

Considering flow at high Reynolds numbers and far from solid surfaces (viscous regions), one can neglect all the shear stresses and heat conduction terms from the Navier-Stokes equations. The result is a mathematically simpler system of equations called the *time-dependent Euler* equations.

This formulation can be applied in the study of compressible flows, for example the flutter of a complex geometry [32].

Potential Flow

At a lower level, this is the formulation in which, from the previous model, it is additionally assumed that the flow is non-rotational and isentropic. The result is the *Potential Flow Model*.

Because of the isentropic condition, this model can not compute shock waves, since they are characterized by irreversible increasing of the entropy [27]. Therefore, for transonic or supersonic flows, the Euler equations are more adequate. Since this work is completely done in the subsonic domain, it makes all the sense to use this approximation. In the next section, the equations of the potential flow and its many solutions are presented, based on Katz and Plotkin [1].

3.3 Incompressible Potential Flow

In this section, the fundamental theory of this type of flows is presented. It starts with some definitions, then the governing equations are briefly derived and the most important solutions obtained.

3.3.1 Vorticity and Circulation

Before going into the governing equations, it is needed so state some definitions.

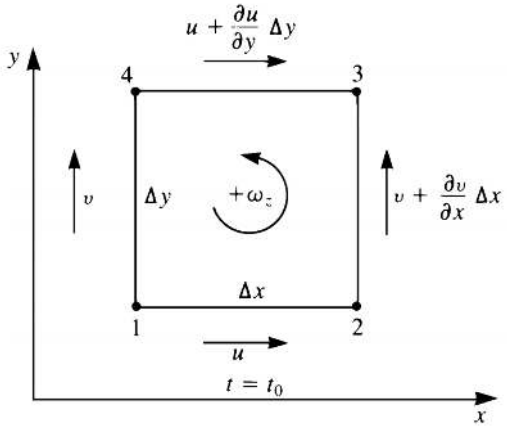

Figure 3.2: Rotating fluid element [1].

Consider the square fluid element from Figure 3.2 with sides of length Δx and Δy and velocity of corner 1 given by (u, v). The instantaneous angular velocity of segment 1-2 (ω_{1-2}) is the difference between the linear velocities of the two edges, divided by the distance,

$$\omega_{1-2} = \frac{v + \frac{\partial v}{\partial x}\Delta x - v}{\Delta x} = \frac{\partial v}{\partial x}, \tag{3.3}$$

where the negative sign comes from the right-hand rule.

Similarly, for the angular velocity of segment 1-4,

$$\omega_{1-4} = \frac{-\left(u + \frac{\partial u}{\partial y}\Delta y\right) + u}{\Delta y} = -\frac{\partial u}{\partial y}. \tag{3.4}$$

The angular velocity component ω_z can be obtained by averaging the results from Equations (3.3) and (3.4) as

$$\omega_z = \frac{1}{2}\left(\frac{\partial v}{\partial x} - \frac{\partial u}{\partial y}\right), \tag{3.5}$$

and for all components

$$\vec{\omega} = \frac{1}{2}\nabla \times \vec{V}. \tag{3.6}$$

In Fluid Mechanics, it is however more convenient to use the *Vorticity* vector $\vec{\zeta}$, which is defined as twice the angular velocity,

$$\vec{\zeta} = 2\vec{\omega} = \nabla \times \vec{V} = \left(\frac{\partial w}{\partial y} - \frac{\partial v}{\partial z}\right)\vec{i} + \left(\frac{\partial u}{\partial z} - \frac{\partial w}{\partial x}\right)\vec{j} + \left(\frac{\partial v}{\partial x} - \frac{\partial u}{\partial y}\right)\vec{k} \tag{3.7}$$

for Cartesian coordinates.

The condition of *irrotational flow* is that the fluid elements move and deform but they do not rotate, as illustrated in Figure 3.3. The same is saying that the curl of the velocity $\nabla \times \vec{V}$ is zero, and so does the vorticity.

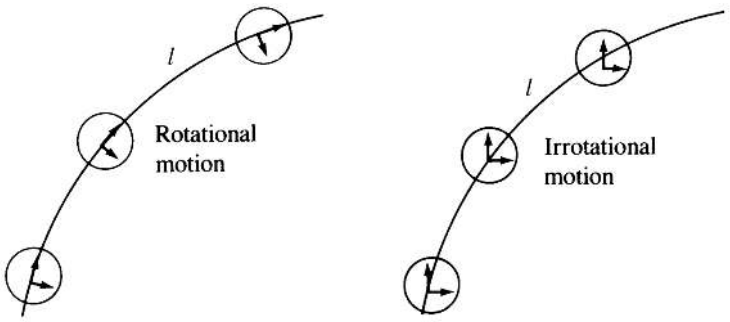

Figure 3.3: Rotational and irrotational fluid motions [1].

Having now an open surface S whose boundary is a closed curve C, the vorticity on the surface is

$$\int_S \vec{\zeta} \cdot \vec{n}\, dS = \int_S \nabla \times \vec{V} \cdot \vec{n}\, dS, \tag{3.8}$$

where $\vec{n}$ is the unity vector normal to S. Applying the Stokes' theorem results in

$$\int_S \nabla \times \vec{V} \cdot \vec{n}\, dS = \oint_C \vec{V} \cdot \vec{dl} \equiv \Gamma. \tag{3.9}$$

In Equation (3.9), the quantity Γ is named *Circulation*. It is related with the rotation of the fluid elements.

An important fact was obtained from Lord Kelvin, the *Kelvin's Theorem*, which states that, for an inviscid and barotropic flow with conservative body forces, the circulation around a closed curve moving with the fluid remains constant in time [33]. This will have some consequences in the case of lifting bodies.

3.3.2 Governing Equations

In this section, the assumptions of potential flow are applied, to obtain the flow governing equations.

If one has an incompressible fluid, which means ρ is constant, Equation (3.1a) stays simply

$$\nabla \cdot \vec{V} = 0. \tag{3.10}$$

Furthermore if the flow is irrotational, the velocity $\vec{V}$ can be represented as the gradient of a scalar function $\Phi = \Phi(x, y, z)$ as

$$\vec{V} = \nabla\Phi, \tag{3.11}$$

which is known as the velocity potential (the full derivation and mathematical proof can be consulted in Kreyszig [34]). Substituting in Equation (3.10), one gets the so called *Laplace equation*

$$\nabla \cdot (\nabla \cdot \Phi) = \nabla^2\Phi = 0. \tag{3.12}$$

Equation (3.12) is a linear differential equation. It was extensively studied and it has many possible analytical solutions. Also, because it is linear, the *principle of superposition* applies. This means that if Φ_1, Φ_2, ..., Φ_n are solutions of the Laplace equation, then

$$\Phi = \sum_{k=1}^{n} c_k \Phi_k \tag{3.13}$$

is also a solution for it (c_k are arbitrary constants).

The problem is closed with the impermeability condition,

$$\nabla\Phi \cdot \vec{n} = 0, \tag{3.14}$$

that expresses that the velocity normal to a solid body (in a body fixed coordinate system) is zero. Also, the disturbance created by the motion should vanish far from the body

$$\lim_{\vec{r}\to\infty} (\nabla\Phi - \vec{V_\infty}) = 0, \tag{3.15}$$

where $\vec{V_\infty}$ is the far field undisturbed velocity and $\vec{r} = (x, y, z)$.

The next step is then find solutions of the Equation (3.12), applying the boundary conditions, Equations (3.14) and (3.15).

3.3.3 Elementary Solutions

As it was mentioned before, many basic solutions exist for the Laplace equation. Here only the ones with physical interest in fluid flow using Cartesian coordinates will be presented.

Polynomials

A first simple solution is

$$\Phi = U_\infty x + V_\infty y + W_\infty z, \tag{3.16}$$

where $(U_\infty, V_\infty, W_\infty)$ are the three components of the velocity field. This is the constant free stream flow case.

A second-order polynomial $\Phi = Ax^2 + By^2 + Cz^2$ can also be a solution as far as

$$A + B + C = \nabla^2 \Phi = 0. \tag{3.17}$$

Many constants can satisfy this conditions, e.g. for a certain combination the result is a flow around a corner, or against a flat plate.

Source/Sink

The velocity potential of a point source or sink is

$$\Phi = -\frac{\sigma}{4\pi \left|\vec{r} - \vec{r_0}\right|}, \tag{3.18}$$

where σ is the volumetric rate at which the fluid comes from the source ($\sigma > 0$) or goes into the sink ($\sigma < 0$); $\vec{r_0}$ is the point location (x_0, y_0, z_0).

This 'introduction' or 'removal' of fluid violates the conservation of mass. Therefore, this point has to be excluded from the region of solution, as it represents a mathematical singularity.

The potential function and the respective velocity vector can then be developed, resulting in

$$\Phi(x, y, z) = -\frac{\sigma}{4\pi\sqrt{(x - x_0)^2 + (y - y_0)^2 + (z - z_0)^2}} \tag{3.19}$$

and

$$\vec{V} = \nabla \cdot \Phi = \frac{\sigma}{4\pi \left[(x - x_0)^2 + (y - y_0)^2 + (z - z_0)^2\right]^{3/2}} \cdot \begin{pmatrix} x - x_0 \\ y - y_0 \\ z - z_0 \end{pmatrix}. \tag{3.20}$$

Doublet

Another different element happens when one sink and one source with the same strength σ are joined, and the flow when the distance between them goes to zero is calculated (see Figure 3.4).

The result is the velocity potential

$$\Phi(x, y, z) = \frac{\mu}{4\pi} \frac{\partial}{\partial n} \frac{1}{\sqrt{(x - x_0)^2 + (y - y_0)^2 + (z - z_0)^2}}, \tag{3.21}$$

where μ is the doublet strength and $\frac{\partial}{\partial n}$ is the normal derivative or the derivative in the doublet direction (e_l in figure 3.4).

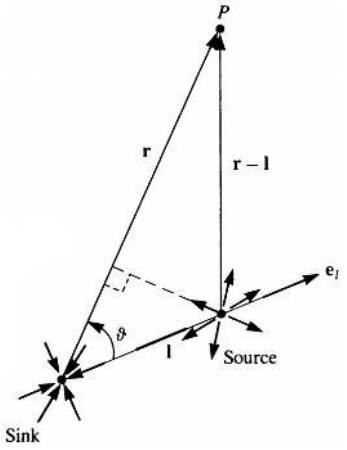

Figure 3.4: Schematic of the sink and source (when l goes to zero, one has a doublet) [1].

Having, for instance, a doublet in the x-direction, $\frac{\partial}{\partial n}$ becomes $\frac{\partial}{\partial x}$ and the velocity potential is

$$\Phi(x,y,z) = -\frac{\mu(x-x_0)}{4\pi\left[(x-x_0)^2+(y-y_0)^2+(z-z_0)^2\right]^{3/2}}. \tag{3.22}$$

One more differentiation gives the velocity field for that case as

$$\vec{V} = \frac{\mu}{4\pi\left[(x-x_0)^2+(y-y_0)^2+(z-z_0)^2\right]^{5/2}} \cdot \begin{pmatrix} -\left[(y-y_0)^2+(z-z_0)^2-2(x-x_0)^2\right] \\ 3(x-x_0)(y-y_0) \\ 3(x-x_0)(z-z_0) \end{pmatrix}. \tag{3.23}$$

Vortex

This singularity can be idealized as a rigid cylinder rotating in a viscous fluid with some constant angular velocity. It can be proved that this vortex flow is irrotational everywhere, except at the core [1]. When the core size approaches zero, then it satisfies the potential flow conditions (except the center point which is a singularity). That idealized two dimensional flow is shown in Figure 3.5.

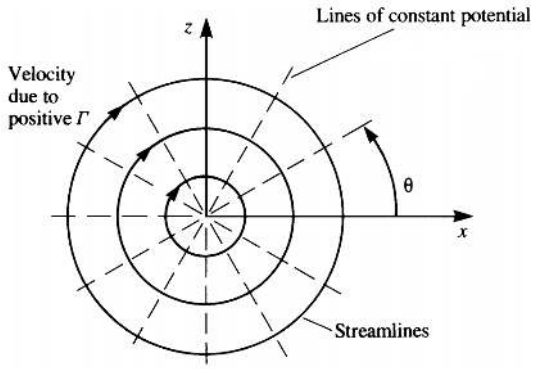

Figure 3.5: Two dimensional vortex centered at the origin [1].

The velocity potential and vector for the vortex centered at (x_0, z_0) are, respectively,

$$\Phi(x,z) = -\frac{\Gamma}{2\pi}\tan^{-1}\frac{z-z_0}{x-x_0} \tag{3.24a}$$

and

$$\vec{V}(x,z) = \frac{\Gamma}{2\pi}\frac{1}{(z-z_0)^2+(x-x_0)^2}\cdot\begin{pmatrix} z-z_0 \\ -(x-x_0)\end{pmatrix}. \tag{3.24b}$$

The three dimensional vortex is simply the two dimensional one propagated in the perpendicular direction forming a tube or filament.

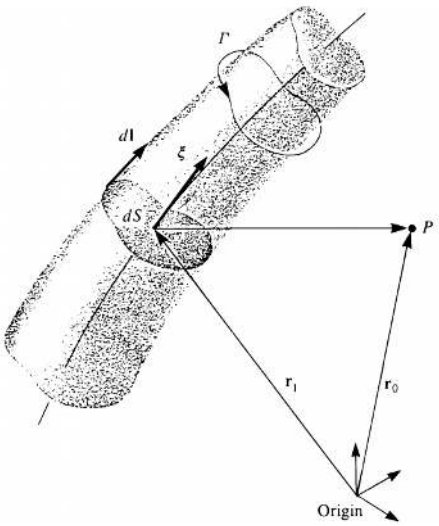

Figure 3.6: Three dimensional vortex segment [1].

The velocity induced by a vortex segment in the point P (Figure 3.6) is calculated using the *Biot-Savart Law* as

$$\vec{V} = \frac{\Gamma}{4\pi}\int\frac{\vec{dl}\times(\vec{r_0}-\vec{r_1})}{|\vec{r_0}-\vec{r_1}|^3}. \tag{3.25}$$

3.3.4 Pressure Computation

As the main objective of the flow simulation is to compute forces applied in the body, after calculating the velocity field $\vec{V}$, the calculation of the pressure field follows.

For that, the momentum conservation Equation (3.1b) is used, which in case of inviscid incompressible fluid simplifies to

$$\frac{\partial\vec{V}}{\partial t} + \vec{V}\cdot\nabla\vec{V} = -\frac{\nabla p}{\rho} + \vec{f}. \tag{3.26}$$

Equation (3.26) is called the incompressible Euler equation.

The convective term $\vec{V}\cdot\nabla\vec{V}$ can be rewritten using a vector identity [1],

$$\vec{V}\cdot\nabla\vec{V} = \nabla\frac{V^2}{2} - \vec{V}\times(\nabla\times\vec{V}), \tag{3.27}$$

where the second term vanishes for the irrotational flow. Also the time derivative can be written as

$$\frac{\partial \vec{V}}{\partial t} = \frac{\partial}{\partial t}\nabla\Phi = \nabla\left(\frac{\partial \Phi}{\partial t}\right), \tag{3.28}$$

using the mathematical properties of the derivation.

Furthermore, if $\vec{f}$ represents conservative external body forces, e.g. gravity, it can be written as the gradient of a potential E

$$\vec{f} = -\nabla E. \tag{3.29}$$

Substituting (3.27), (3.28) and (3.29) into (3.26), yields

$$\nabla\left(E + \frac{p}{\rho} + \frac{V^2}{2} + \frac{\partial \Phi}{\partial t}\right) = 0, \tag{3.30}$$

which is only true if the quantity in parentheses is a function of time only

$$E + \frac{p}{\rho} + \frac{V^2}{2} + \frac{\partial \Phi}{\partial t} = C(t). \tag{3.31}$$

Equation (3.31) is the *Bernoulli equation* for inviscid incompressible irrotational flow.

This means that at a certain time t_1, the quantity at the left-hand side of (3.31) must be equal throughout the field. Particularly, one can compare any point of the field with a reference point, say at infinity, hence

$$\left[E + \frac{p}{\rho} + \frac{V^2}{2} + \frac{\partial \Phi}{\partial t}\right] = \left[E + \frac{p}{\rho} + \frac{V^2}{2} + \frac{\partial \Phi}{\partial t}\right]_\infty. \tag{3.32}$$

If this reference condition is chosen such that $E_\infty = 0$ and $\Phi_\infty = \text{const.}$, then the pressure at any point can be calculated from

$$\frac{p_\infty - p}{\rho} = \frac{\partial \Phi}{\partial t} + E + \frac{V^2 - V_\infty^2}{2}. \tag{3.33}$$

In the case of a steady problem with no external forces, the steady-state Bernoulli equation holds,

$$p_\infty + \frac{1}{2}\rho V_\infty^2 = p + \frac{1}{2}\rho V^2. \tag{3.34}$$

From here, the pressure coefficient can be defined as

$$C_p \equiv \frac{p - p_\infty}{0.5\rho V_\infty^2} = 1 - \left(\frac{V}{V_\infty}\right)^2. \tag{3.35}$$

3.3.5 Lifting Body

Getting back to the context of this work, the goal is to perform studies of lifting bodies. In other words, bodies that when submerged in a free stream flow, are pushed perpendicular to the flow direction, e.g. the wing on an airplane.

Kutta and Joukowski discovered that this is only possible if the flow has circulation (Γ defined in Equation (3.9)). This was stated on the *Kutta-Joukowski Theorem* [1]:

"The resultant aerodynamic force in an incompressible, inviscid, irrotational flow in an unbounded fluid is of magnitude $\rho V_\infty \Gamma$ per unit width, and acts in a direction normal to the free stream".

Using more general vector notation,

$$\vec{F} = \rho \vec{V}_\infty \times \vec{\Gamma}, \tag{3.36}$$

where $\vec{F}$ is the aerodynamic force per unit width and the positive $\vec{\Gamma}$ is defined with the right-hand rule.

Finally it is needed something that can say how strong are the vortexes or how much is the total circulation. This comes from the *Kutta condition*.

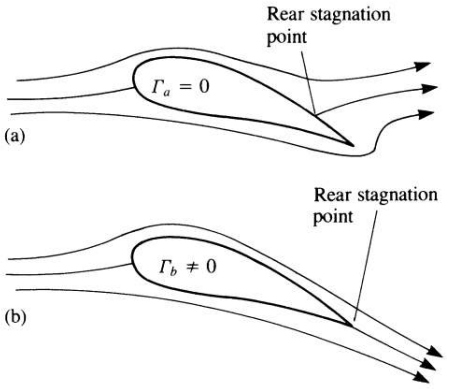

Figure 3.7: Possible cases for the flow over an airfoil: (a) zero circulation, (b) flow with circulation resulting in a smooth flow near the trailing edge [1].

If one constructs an airfoil using a certain distribution of sources and sinks, the result is more likely to be something similar to Figure 3.7(a), where the velocity at the trailing edge is infinite.

Kutta stated that *the flow leaves the sharp trailing edge of an airfoil smoothly and the velocity there is finite* [1]. The way to this is to add circulation in such a way that the rear stagnation point moves to the trailing edge.

3.4 Numerical Methods

When solving flow using the full potential approximation, in some cases it is possible to obtain analytical solutions for example for thin airfoils and wings or using the complex potential and complex transformations (some applications are presented in Katz and Plotkin [1]). However, for more realistic geometries, numerical techniques are needed.

In the case of viscous compressible fluids approaches such as Finite-Volume or Finite-Element methods are typically used, that solve the whole fluid volume using complex meshes. For the simpler case of potential flow, also simpler methods exist such as the *panel method*. This method consists in modeling the body with N panels, using a distribution of basic singularity elements presented in Section 3.3.3.

Advantages of linear panel methods include quick run times, relatively easy geometrical modeling, and little user interface. They can not predict transonic flows with nonlinear phenomena (such as shock waves), being however still used in an industrial environment in the first design stages [35].

The panel method can be summed in the following steps:

1. **Selection of singularity element.** This includes the selection of source, doublet or vortex representation and the order to discretize these distributions (constant, linear, quadratic, etc...);
2. **Discretization of geometry.** The geometry of the problem is subdivided and the panels defined together with the corner points and the collocation points, where the boundary conditions are enforced;
3. **Influence Coefficients.** For each of the elements' collocation points, an algebraic equation is derived, forming a matrix system of equations;
4. **Solution of matrix.** The previous set of equations is solved using standard matrix techniques (that will be presented later);
5. **Variables computation.** The variables with physical meaning are calculated, such as velocities, pressures and forces.

Many formulations can be done to the construction of a panel method program, namely depending on the singularities selected. Moran [36] makes a review on this subject based on many studies. Moreover it states that for a certain continuous distribution of vortex over some panels, there is an equivalent distribution of doublets over the same panels, with the vortex strength being the derivative of the doublet strength. Since the strength of the doublet is the value of the potential on the surface, the vortex strength is the correspondent tangential velocity.

The panel methods based on sources and vortexes are physically easier to understand and create. However their distribution must satisfy the Helmholtz vortex theorems (see [1]) to maintain the flow irrotational. Furthermore, results comparison between doublet and vortex panel methods with the same number of panels, show that doublet-based calculations take less time and give better results [36]. Therefore, the doublet panel method is chosen for this work.

3.4.1 Basic Formulation

Considering the body of Figure 3.8 submerged in a potential flow, a panel formulation can be obtained using one of Green's identities (full derivation in [1]).

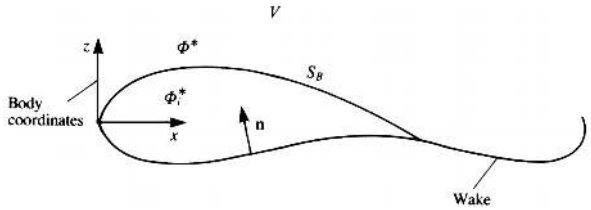

Figure 3.8: Inner and outer velocity potentials and the body coordinate system [1].

If Φ^* is the total velocity potential in the body frame of reference,

$$\Phi^*(x,y,z) = \frac{1}{4\pi}\int_{body+wake} \mu\vec{n}\cdot\nabla\left(\frac{1}{r}\right)dS - \frac{1}{4\pi}\int_{body}\sigma\left(\frac{1}{r}\right)ds + \Phi_\infty, \tag{3.37}$$

where μ and σ represent, respectively, the strength of doublets and sources and Φ_∞ is the free stream potential as defined in Equation (3.16). It can be observed that the body is modeled with doublets and sources, while the wake has only doublets. This is physically understandable since the sources are used mainly to add thickness to the body.

Moving forward to the boundary conditions, the one presented in Equation (3.15) is automatically met by all the solution elements considered. The impermeability condition can be applied in two ways:

- Applying Equation (3.14) directly to (3.37), which results in

$$\left\{ \frac{1}{4\pi} \int_{body+wake} \mu \nabla \left[\vec{n} \cdot \nabla \left(\frac{1}{r} \right) \right] dS - \frac{1}{4\pi} \int_{body} \sigma \nabla \left(\frac{1}{r} \right) dS + \nabla \Phi_\infty \right\} \cdot \vec{n} = 0, \tag{3.38}$$

  which is computed for every point on the surface of the body S_B. This direct formulation is called the *Neumann problem.*

- Another approach comes from the observation that the potential inside the body Φ_i^* will not change. This means that

$$\Phi_i^*(x,y,z) = \frac{1}{4\pi} \int_{body+wake} \mu \vec{n} \cdot \nabla \left(\frac{1}{r} \right) dS - \frac{1}{4\pi} \int_{body} \sigma \left(\frac{1}{r} \right) dS + \Phi_\infty = const. \tag{3.39}$$

  This is called the *Dirichlet problem.* If one sets this constant equal to the free-stream potential Φ, then Equation (3.39) reduces to a simpler form

$$\frac{1}{4\pi} \int_{body+wake} \mu \vec{n} \cdot \nabla \left(\frac{1}{r} \right) dS - \frac{1}{4\pi} \int_{body} \sigma \left(\frac{1}{r} \right) dS = 0. \tag{3.40}$$

It is important to say that this formulation does not uniquely describe a solution, since a large number of source and doublet distributions will satisfy a given set of boundary conditions.

Wake Model

An additional help on this task comes from the wake conditioning. The two-dimensional linear Kutta condition can be written in the form

$$\mu_W = \mu_U - \mu_L, \tag{3.41}$$

where μ_U and μ_L are the upper and lower surface doublet strengths at the trailing edge and μ_W is constant along the wake.

An alternative method often used in potential flow problems is the iterative pressure Kutta condition [37]. In this formulation, the pressure is imposed to be equal on both sides of the lifting surface at the trailing edge. Due to the non-linear character of pressure, the system of equations becomes non-linear, which has to be solved with a proper numerical method.

Baltazar [37] presents several studies which compare the two formulations, concluding that the difference is only meaningful at the wing tip for bodies with variable cross sections, such as elliptical wings or marine propellers. In the present work, the objectives of study are rectangular wings, so the simpler linear Kutta condition is used.

Using the Kutta-Joukowski theorem (3.36), the force $\Delta\vec{F}$ generated by the wake is zero. This means the vorticity vector is parallel to the local velocity vector. As said before, the vorticity is equivalent to the derivative of the doublet strength μ_W. Hence

$$\vec{V} \times \nabla\mu_W = 0. \tag{3.42}$$

Two ways are then presented to determine the wake shape:

- Prescribed wake shape based on flow visualizations or simply or intuition. This method is the simplest and very useful while analyzing multi-element airfoils [1];

- The initial wake geometry is specified by the programmer and then several wake grid planes are established. The first calculation is normally performed and the velocity induced by the wing and wake on each of the wake points is obtained. Next, the wake points are moved by the local velocity times an artificial time parameter. This process is called *wake relaxation* and it takes as many iterations as needed for convergence or until condition (3.42) is met [1].

Reduction of the Problem to a Set of Linear Algebraic Equations

After defining the number and distribution of all source/doublet elements, the equations are applied to each panel and assembled in matrix form. The body surface is now discretized into N surface panels and the wake is modeled using N_W panels.

Rewriting the Dirichlet boundary condition (3.40) for each of the collocation points, one gets

$$\sum_{k=1}^{N} \frac{1}{4\pi} \int_{body\ panel} \mu\vec{n} \cdot \nabla\left(\frac{1}{r}\right) dS + \sum_{l=1}^{N_W} \frac{1}{4\pi} \int_{wake\ panel} \mu\vec{n} \cdot \nabla\left(\frac{1}{r}\right) dS - \sum_{k=1}^{N} \frac{1}{4\pi} \int_{body\ panel} \sigma\left(\frac{1}{r}\right) dS = 0. \tag{3.43}$$

This means that for each collocation point the summation of the influences of all k body panels and l wake panels is needed.

If the singularity elements have constant strength in each panel, the integrals depend only on the geometry. Equation (3.43) is then

$$\sum_{k=1}^{N} C_k\mu_k + \sum_{l=1}^{N_W} C_l\mu_l + \sum_{k=1}^{N} B_k\sigma_k = 0 \tag{3.44}$$

for each collocation point P, where

$$C_i = \frac{1}{4\pi} \int_{1,2,3,4} \vec{n} \cdot \nabla\left(\frac{1}{r}\right) dS\Bigg|_i \qquad \text{and} \qquad B_i = \frac{-1}{4\pi} \int_{1,2,3,4} \left(\frac{1}{r}\right) dS\Bigg|_i . \tag{3.45}$$

In conclusion, for any control point P, the influence of each k panel (defined by four corners 1,2,3 and 4 like in Figure 3.9) is computed.

For Equation (3.40) to be valid and from the definition of the source strength σ, it comes an additional

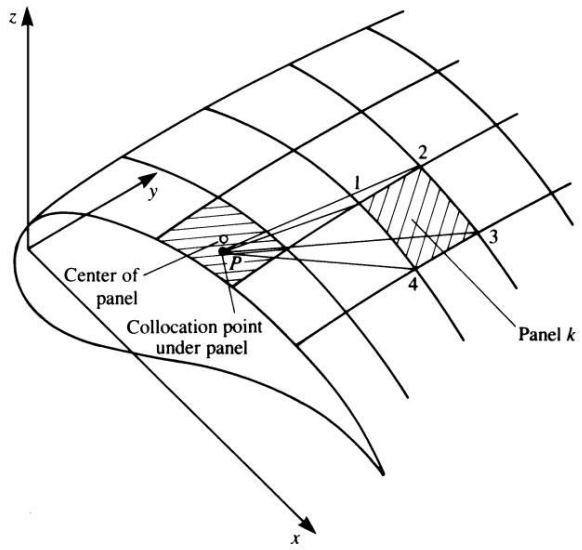

Figure 3.9: Influence of the panel 1234 in the point P [1].

condition that

$$\sigma = \vec{n} \cdot \vec{V}_\infty. \tag{3.46}$$

And this way the third term on (3.43) is calculated and can be moved to the right-hand side.

The influence from the wake comes from the Kutta condition (Equation (3.41)) which gives a relation between μ_k and μ_l. This can be applied creating another coefficient

$$A_k = \begin{cases} C_k & \text{if panel is not at T.E.} \\ C_k \pm C_l & \text{if panel is at T.E.} \end{cases}. \tag{3.47}$$

This turns (3.39) into

$$\sum_{k=1}^{N} A_k \mu_k = -\sum_{k=1}^{N} B_k \sigma_k, \tag{3.48}$$

which is a system of N equations for N variables μ_k.

For the case of more complex panels (e.g. curved) or singularity distributions (linear or quadratic), matrix inversion and numerical integration methods may be needed.

Aerodynamic Loads

Once Equation (3.48) is solved, the two tangential and normal perturbation velocities are, respectively,

$$V_l = -\frac{\partial \mu}{\partial l}, \qquad V_m = -\frac{\partial \mu}{\partial m}, \qquad V_n = -\sigma, \tag{3.49}$$

where (l, m, n) are the local coordinates of the panel. The differentiation is done numerically using the values on the neighbor panels. So the total velocity on panel k is

$$\vec{V}_k = (V_{\infty_l}, V_{\infty_m}, V_{\infty_n})_k + (V_l, V_m, V_n)_k. \tag{3.50}$$

The pressure coefficient is so calculated as in Equation (3.35). The contribution of the panel to the fluid dynamic load becomes

$$\Delta\vec{C}_{F_k} = -\frac{C_{p_k}\Delta S}{S}\vec{n}_k, \tag{3.51}$$

where ΔS is the area of the panel, S is a reference area and $\vec{n}_k$ is the vector normal to the panel.

All the contributions are summed and the result is decomposed in Lift and Drag forces, respectively in the direction and normal to the free stream velocity (see Figure 3.10). As in the potential flow no viscous effect are accounted, the only drag calculated is the lift-induced drag D_i, only present in 3D problems.

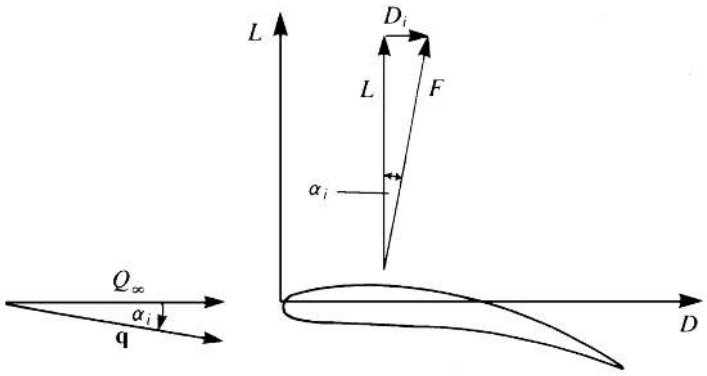

Figure 3.10: Typical forces used in aerodynamics, lift and drag [1].

3.4.2 Unsteady Problems

As seen before, for the incompressible potential flow conditions, the continuity equation does not directly include time-dependent terms. These are introduced through the boundary conditions by applying some modifications to the previous definitions, namely:

- The zero normal flow condition on a solid surface (Equation (3.38)) is reformulated;
- The computation of pressure is made with the full Bernoulli Equation (3.31);
- The unsteady wake needs a special concern.

For time-dependent problems, the selection of a coordinate system plays an important role and has many consequences. So a special attention is given to it in the next section.

Coordinates Choice

In order to apply the zero normal flow boundary condition, it is useful to define a body-fixed coordinate system (x, y, z), whose instantaneous location $\vec{R}_0(t)$ and orientation $\vec{\Theta}(t)$ in relation to an inertial system (X, Y, Z) (see Figure 3.11) are

$$\vec{R}_0(t) = (X_0, Y_0, Z_0) \tag{3.52a}$$

and

$$\vec{\Theta}(t) = (\phi, \theta, \psi). \tag{3.52b}$$

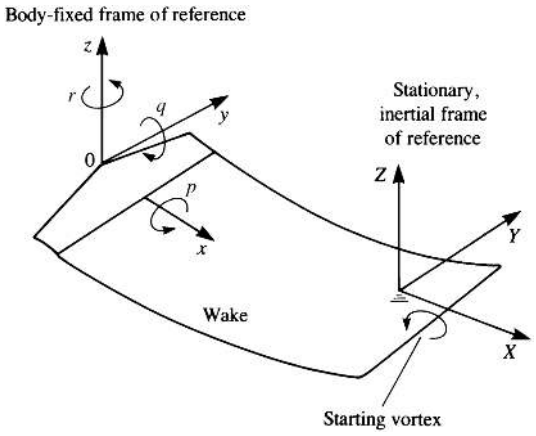

Figure 3.11: Wing movement and the frames of reference [1].

It can be proved that the mass conservation is independent of the coordinate system [1], so Equation (3.12) is still valid in the body-fixed frame.

However, the normal zero velocity condition is now (in the body-fixed frame)

$$(\nabla\Phi + \vec{v}) \cdot \vec{n} = 0, \tag{3.53}$$

where $\vec{v}$ is the surface's velocity and is equal to

$$\vec{v} = -(\vec{V_0} + \vec{v}_{rel} + \vec{\Omega} \times \vec{r}), \tag{3.54}$$

where $\vec{V_0} = (\dot{X}_0, \dot{Y}_0, \dot{Z}_0)$ is the velocity of the (x, y, z) frame, $\vec{\Omega} = (p, q, r)$ is the rate of rotation of the same (Figure 3.11) and $\vec{v}_{rel}$ represents an additional relative motion, for example, in the case of small oscillations to the average motion. It is important to mention that this vector has the negative sign, so that the free stream velocity is positive.

Applying this result to the formulation presented in Section 3.4.1, the Dirichlet boundary condition does not change, while the Neumann (3.38) becomes

$$\left\{ \frac{1}{4\pi} \int_{body+wake} \mu \nabla \left[\vec{n} \cdot \nabla \left(\frac{1}{r} \right) \right] dS - \frac{1}{4\pi} \int_{body} \sigma \nabla \left(\frac{1}{r} \right) dS - \vec{V_0} - \vec{v}_{rel} - \vec{\Omega} \times \vec{r} \right\} \cdot \vec{n} = 0. \tag{3.55}$$

Furthermore, the source strength σ which was previous defined in Equation (3.46) is now

$$\sigma = -\vec{n} \cdot (\vec{V_0} + \vec{v}_{rel} + \vec{\Omega} \times \vec{r}). \tag{3.56}$$

Pressure Computation

To calculate the pressure from the velocity potential and vector, the instantaneous Bernoulli Equation (3.31) is used, in the form

$$\frac{p_{ref} - p}{\rho} = \frac{V^2}{2} - \frac{v_{ref}^2}{2} + \frac{\partial\Phi}{\partial t}, \tag{3.57}$$

where $\vec{V}$ and p are the local fluid velocity and pressure, p_{ref} is the reference pressure and $\vec{v}_{ref}$ is the kinematic velocity previous defined in Equation (3.54). The reference will be considered the far field condition throughout this work. The pressure coefficient is then

$$C_p = \frac{p - p_\infty}{0.5\rho V_\infty^2} = 1 - \frac{V^2}{V_\infty^2} - \frac{2}{V_\infty^2}\frac{\partial \Phi}{\partial t}. \tag{3.58}$$

The derivative of the velocity potential over time deserves special attention. The integration over time demands a time discretization method. Since the goal here is to obtain the pressure coefficient at the time $t + \Delta t$, an implicit method is required. The simpler and still largely used option is the *Backward Euler Method* [27], which applied to (3.58) yields

$$C_p^{t+\Delta t} = 1 - \frac{(V^{t+\Delta t})^2}{V_\infty^2} - \frac{2}{V_\infty^2}\left(\frac{\Phi^{t+\Delta t} - \Phi^t}{\Delta t}\right), \tag{3.59}$$

which is first order accurate. A second order method is the *Crank-Nicholson Method* [27], which also use the previous velocity and pressure. Considering the Equation (3.58) in the form

$$\frac{\partial \Phi}{\partial t} = H, \tag{3.60}$$

the Crank-Nicholson Method is

$$\frac{\Phi^{t+\Delta t} - \Phi^t}{0.5\Delta t} = H^{t+\Delta t} + H^t. \tag{3.61}$$

Substituting Equation (3.58), yields

$$C_p^{t+\Delta t} = 2 - C_p^t - \frac{(V^{t+\Delta t})^2 + (V^t)^2}{V_\infty^2} - \frac{2}{V_\infty^2}\left(\frac{\Phi^{t+\Delta t} - \Phi^t}{0.5\Delta t}\right). \tag{3.62}$$

Many other options are available in the literature with many other features. In this work, this two options are considered enough considering the level of approximation used.

Wake Shape

Going back to Section 3.4.1, two ways were presented to obtain a wake shape. Prescribing it is still an option, but not very reliable in the unsteady case. Furthermore, the wake relaxation method is clearly inadequate, because of the need of wake stabilization.

The option here is a *time-stepping method*. The principle is similar to the wake relaxation but now the time step is directly related to the motion. During the computations, the number of wake panel increases with time, in the sequence:

1. The whole wake is moved by a distance which is equal to the time step times the free stream velocity. The moved panels maintain their doublet strength;

2. A new wake panel row is created, linking the trailing edge to the last wake row;

3. The new flow state is calculated, adding all the wake influences to the body panels. The new doublet row strengths is a direct result of the Kutta condition.

This method makes it possible to change the flow and body parameters at any time (for example an heaving motion like in Figure 3.12).

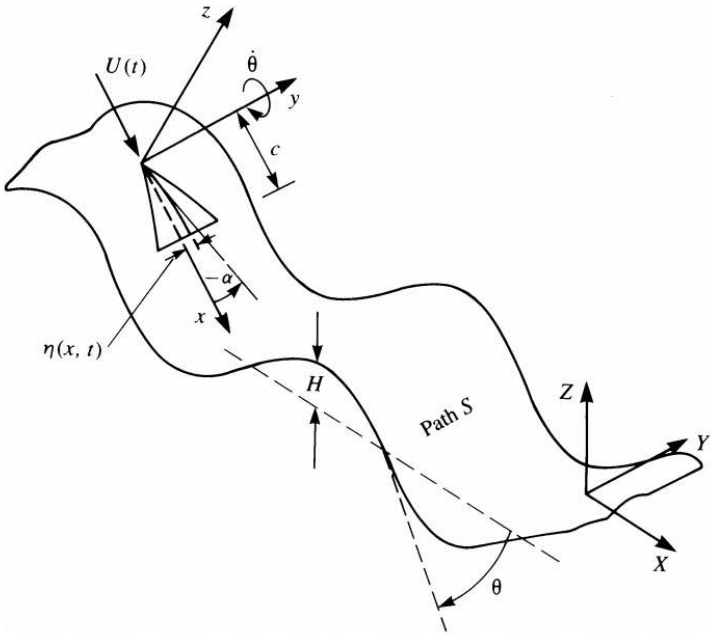

Figure 3.12: Example of an unsteady problem - heaving oscillation [1].

3.4.3 Enhancement of the Potential Model

Some modifications can be made to the previous models to improve their accuracy.

The fluid was considered inviscid which is indeed a big simplification. A next step may be consider two sections, one outer region inviscid and another region near the body where the viscous effects are taken into account. This region is called the *Boundary Layer* and it is much smaller then the length of the solid surface. There are many theories to compute the velocity evolution from zero at the surface (no-slip condition) to the near-body velocity calculated with the inviscid model.

The coupling between the inviscid and viscous solvers would also need some special handling. The application of this improvement is out of the scope of this work and will not be done here. However a complete derivation and application to the panel methods can be found in Katz and Plotkin [1].

Chapter 4

Fluid-Structure Coupling

In the previous chapters, the governing equations for both domains which take part in any aeroelastic phenomena, fluid and solid, were shortly presented. Particularly, for the fluid dynamics section, some approximations were stated and its consequences discussed.

This chapter is intended to explore the linking and influencing of the two parts, the so called *Fluid-Structure Interaction (FSI)*. Bazilevs et al. [38] made a fully revision of the state-of-the-art in the area and identified three major challenges of any FSI problem: *problem formulation*, *numerical discretization* and *fluid-structure coupling*. The first two are related with the domain conditioning and approximations and were developed in Chapters 2 and 3. Herein one will address the remaining problems which arise from the two different subsystems.

Kamakoti and Shyy [39] organized the range of FSI models in three categories, being however a little ambiguous. More recently, Bazilevs et al. [38] made a different classification using only two classes: strongly-coupled (or monolithic) and loosely-coupled (or staggered).

4.1 Monolithic Approach

In this model, the equations of fluid, structure and mesh moving are solved simultaneously. Hereby a fully-integrated FSI solver is written, which increases the robustness. However, such an approach can be very challenging to perform for a large-scale problem.

Three categories of strongly-coupled techniques are mentioned [39]:

- *Block-iterative coupling* - the fluid, struture and mesh systems are treated as separate blocks, and the nonlinear iterations are carried out one block at a time;

- *Quasi-direct coupling* - the same idea as the block iterative but with fluid and structure equations joined in the same block;

- *Direct coupling* - one has only one block, so that all the variables are joined in one set of equations.

4.1.1 Frame of Reference

To be able to solve all the domains simultaneously, the first question comes from the frame of reference. Normally, when solving fluid flows, an *Eulerian* (or space fixed) frame is applied, while a structural problem uses a *Lagrangian* (or material fixed) coordinate system [40].

In aeroelastic problems with both fluids and solids, none of the formulations is optimal for the entire domain. Besides, the coupling algorithm is quite complex if it has to handle with a Lagrangian mesh overlapping an Eulerian mesh.

The most used solution is the Arbitrary Lagrangian-Eulerian (ALE) method, which allows the mesh to move in arbitrary manner, having the two limiting cases reducing to the Lagrangian and Eulerian formulations [40].

4.1.2 Added-Mass Effect

In fluid mechanics, added mass is the inertia added to a system because an accelerating or decelerating body must move some volume of surrounding fluid as it moves through it, since the object and fluid cannot occupy the same physical space simultaneously [40].

This issue comes into play in the iteration process of a monolithic scheme. In the case of applications like blood flows, flying bugs or parachutes, where the density of the fluid and structure are comparable, the added-mass effect can cause the scheme to be unstable. It does not have influence in the case of aircraft wings though.

4.2 Staggered Approach

Farhat and Lesoinne [41] emphasize the nonlinearity of the fluid equations (in the case of Navier-Stokes or Euler equations), while the structure equations can be linear or nonlinear. Such a situation can result in matrices with different characteristics and so complicate the solving procedure. Therefore, a monolithic scheme is in general computationally challenging, mathematically and economically suboptimal, and software-wise unmanageable.

Alternatively, the equations of fluid and structure mechanics can be solved by a staggered procedure. For a given time step, such an algorithm typically involves the solution of the fluid mechanics with the velocity boundary conditions coming from the previous step, followed by the solution of the structural mechanics equations with the updated fluid interface load, and followed by the mesh movement with the new structure displacement [38].

The big attraction of this approach comes simply from the fact that it enables the use of existing fluid and structure solvers, namely commercial ones. For several problems, this option works well and efficiently, but sometimes convergence difficulties arise, mostly when the fluid is fully enclosed by the structure or when the added-mass effect applies.

Having defined both structure and fluid flow solvers, which are completely separated and independent, one has now clear that a staggered procedure is the only option. Farhat and Lesoinne [41] present several

common schemes to transfer the results between subsystems, among which using a parallel computation capacity. In this work, one will stick to the serial procedures which are simpler and more common.

4.2.1 Conventional Serial Staggered Procedure

The basic algorithm is the so called *Conventional Serial Staggered (CSS)* procedure. It is graphically depicted in Figure 4.1 where $\vec{\mathcal{U}}$ denotes the structure state vector (nodal displacement and velocity), $\vec{\mathcal{W}}$ denotes the fluid state vector (in the case of a complete fluid discretization), $\vec{p}$ designates the fluid pressure, n stands for the n^{th} time station, and the equalities shown at the top hold on the fluid/structure interface boundary.

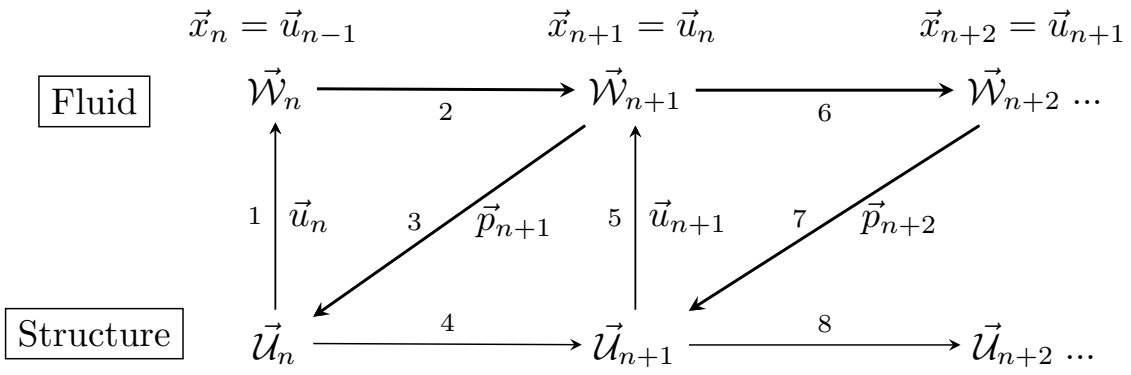

Figure 4.1: Conventional Serial Staggered (CSS) scheme.

In the CSS scheme, the time step Δt is the same for both subsystems. In most of the aeroelastic problems, the fluid flow requires a finer temporal resolution than the structural vibration [41], being therefore Δt dictated by the fluid solution accuracy.

A possible enhancement is to "subcycle" the fluid computation, saving CPU time in the overall simulation, since the structure computational kernel is less times called and the exchange of information will happen fewer times. In practice, this means that in Figure 4.1, steps 2 and 6 will have many phases.

The weakness of this procedure is its mathematically proved first-order time-accuracy, even when the structure and fluid flow solvers have higher order [41]. One possible solution is to include full subiterations on each time step, which however largely increases the computational cost.

4.2.2 Improved Serial Staggered Procedure

A second algorithm is the *Improved Serial Staggered (ISS)* procedure illustrated in Figure 4.2. Basically, the fluid and structure computations are "out of phase", being the structure calculated at the full time-stations and the fluid in the half time-stations [42].

The advantage of this method is that by using not only the structure displacement but also the velocity for the fluid mesh actualization, it does not introduce errors on the energy exchange between fluid and structure, unlike the CSS method [41]. Piperno and Farhat [42] did a deep energy (virtual work) analysis to conclude that the procedure should be as much energy-accurate and conservative as possible, in order to be able to perform aeroelastic computations.

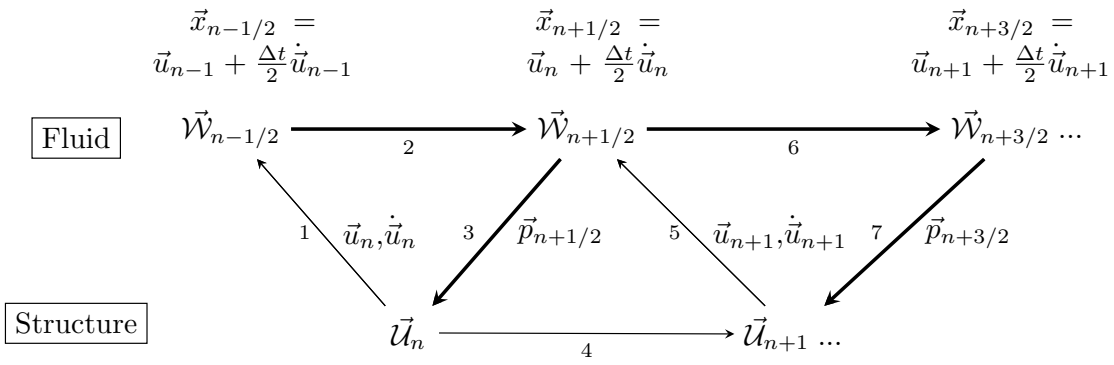

Figure 4.2: Improved Serial Staggered (ISS) scheme.

The ISS method goes as follows:

1. given some initial conditions $\vec{W}_0$, $\vec{u}_0$ and $\dot{\vec{u}}_0$, initialize the fluid dynamic mesh as

   $\vec{x}_{-1/2} = \vec{u}_0 - \frac{\Delta t}{2}\dot{\vec{u}}_0$;

2. update the fluid dynamic mesh as follows (using $\dot{\vec{x}}_n = \dot{\vec{u}}_n$)

   $\vec{x}_{n+1/2} = \vec{x}_{n-1/2} + \Delta t \dot{\vec{x}}_n$;

3. solve the fluid problem to obtain $\vec{W}_{n+1/2}$;

4. extract the pressure field $\vec{p}_{n+1/2}$ from $\vec{W}_{n+1/2}$ and convert it to structural load;

5. advance the structural subsystem using the second-order time-accurate midpoint rule.

To use this procedure, the condition is the midpoint rule for the structural time integration, which is identical to the Newmark scheme used in APDL substituting $\alpha = 1/4$ and $\delta = 1/2$ in (2.7) [42].

4.3 Distributed Loads

As it easily concluded, in any situation when a fluid is in contact with a solid body, the former does not apply concentrated forces in particular points of the latter. Instead, it applies *distributed loads* on areas or pressures. In the case of a FE discretization of the solid, those continuous loads are also discretized and divided over all nodes. The way this is done can influence the results and is addressed as *load consistency*.

The more intuitive method is to consider the distributed loads on an element based on their tributary area. In rectangular elements, for instance, the total load is assigned as four equal concentrated forces acting on the nodes [43]. This is called the *load lumping* (LL). If the pressure applied on the element is not constant, the resultant load is assigned to the centroid of the load diagram and apportioned to the nodes by statics. Furthermore if the element is triangular or it has midpoints, other approximations have to be made [9]. This method is then inconsistent.

Gudla and Ganguli [44] did a numerical and analytical study of the error introduced by this method, concluding that the low error increase of this method makes it an efficient approach because of its large computational savings.

A more exact formulation is to state that during a virtual displacement, the work of the concentrated nodal force and that of the actual distributed load must be equal. This method is naturally more expensive, since extra integrations have to be performed in order to find the loading configuration.

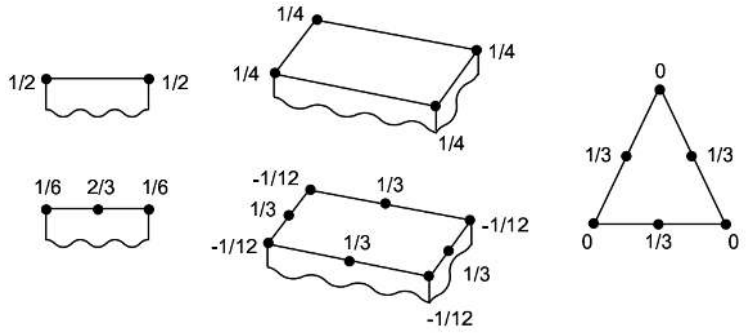

Figure 4.3: Ratios of division of the distributed load applied in different types of elements used in APDL [8].

APDL uses the simpler lumped load approach. Figure 4.3 shows how the division of a distributed load is obtained for a linear, rectangular, rectangular with midside nodes or triangular elements.

4.4 Energy Conservation

Another issue related with the previous section is related to the energy of the system that should be conserved. In another words, the transference of data between fluid and structure should preserve the total energy of the system.

Piperno and Farhat [42] did a deep energy analysis of the two procedures presented, CSS and ISS, using also different time integration methods. They justified this criterion by the fact that one of the most important aspects of aeroelastic computations is the prediction of the positive, zero, or negative damping of a given structure by the surrounding flow. Hence, a non-conservative solution method might contaminate the physical damping with artificial numerical damping. This is particularly important for problems where the flow is at critical conditions.

It is also obvious that a non-consistent transference of loads, cause the solution method to be energetically non-conservative.

4.5 Interface Methods

In general FSI problems, the interface methods between meshes is certainly a determinant aspect of the calculation procedure. This part of the calculation deals with the transformation of the fluid pressures into structural loads and of the structure displacement into the fluid displacement. Since the fluid and structural module can be modeled at different levels of complexity, the fidelity of the interfacing technique depends on how the fluid and structure are modeled [39].

Guruswamy [9] makes a review of several interface techniques solving the fluid flow with Euler/Navier-Stokes equations and the structure with Modal or FEM approaches. It states that, while the fluid grid is

normally very refined close to the body in order to cover viscid effects like the turbulence or the transition, the structure mesh is normally coarser. Therefore, a good scheme to convert all the CFD load into the structure nodes is needed.

In modal analysis, an adequate interpolation proved to be accurate for structured or unstructured meshes [9]. Kamakoti and Shyy [39] suggest many different types of interpolation using splines and gives advantages and limitations of each method.

In the case of beam and shell elements, the same interpolation techniques should be accurate enough, unless the geometry is more complex, for example a wing-body configuration [9]. For these cases, a mapping technique might be a better option using a computational and a physical domains and a set of transfer functions to change coordinates between them.

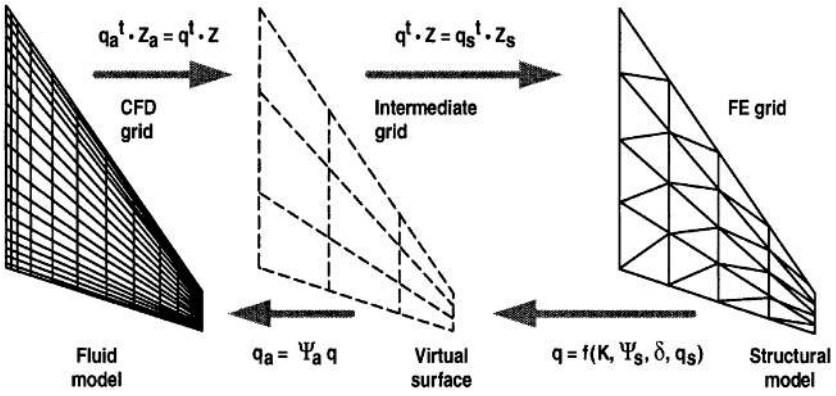

Figure 4.4: FSI interface using a virtual surface and transfer functions [9].

Figure 4.4 illustrates a possible scheme using the so called *virtual surface* method (VS) in which the loads and displacements are transfered between domains using transfer functions. The difference between this method and the previous ones using direct interpolations, is that they use the LL approach. In addition, the deformed configuration of the CFD grid at the surface is obtained by interpolating nodal displacements at the FE nodes. This approach does not conserve the work done by the aerodynamic forces [9]. In the VS approach, a mapping matrix is general enough to accommodate changes in fluid and structural models easily, which assures energy conservation.

Chapter 5

Computational Structural Analysis

In this section, the practical assumptions and simplifications of the structure of study, the aircraft wing, will be covered. Also, following Chapter 2, further explanations will be presented in order to use APDL to calculate the dynamics of the wing.

In order to be consistent with the previous approach from Chapter 6, three simple structural test cases will be done, first to do the verification of the APDL version, using its examples for the SHELL 181 element, and finally using one possible configuration for the aircraft wing.

5.1 Problem Setup

Herein, details about the mesh and initial and boundary conditions as well as time conditioning shall be more developed.

5.1.1 Structural Meshing

In the fluid flow analysis, the wing skin is divided in panels with collocation points in the center, like shown in Figure 3.9. The pressure distribution is then calculated for each panel. This property of the panel method makes it possible to use the same discretization for both structural and aerodynamic problems. Here only the boundary is discretized, while in other fluid solvers all the fluid volume as to be meshed.

This simplifies a lot the FSI calculation, since one of the main problems is the bridge between meshes and, particularly, the deformation of the fluid volume mesh with the displacement of the structure.

In this case, one just simply imports the fluid mesh to APDL basically turning panels into shells, and applies the pressure of the collocation point to the respective element. Hereby, all the elements have to have their normals pointing outwards in order to apply the pressures with the correct direction.

5.1.2 Boundary Conditions

The structural boundary conditions in this case are just the attachment of the wing to the fuselage of the airplane. This is similar to a cantilever beam so, basically, for the nodes with $y = 0$ (wing root section)

all the DOF (displacements and rotations) are constant and equal to zero.

5.1.3 Initial Conditions

For each time step Δt, the structural analysis is restarted and ANSYS reopened. To keep the continuity of the calculation, the final displacements and velocities for each node are saved and then introduced on the next step as initial conditions.

5.1.4 Time Conditioning

In order to improve the structural calculation and also to be able to track the movement in each time step, a number of substeps is imposed and the displacements for each one extracted. Here it was decided to previous stipulate a number of constant time substeps for simplicity.

5.2 Static Test

For the static example, test case 34 from the APDL Verification Manual (VM34) is applied [45]. It studies the bending of a cantilever plate, excited with a single force at the tip node (see Figure 5.1).

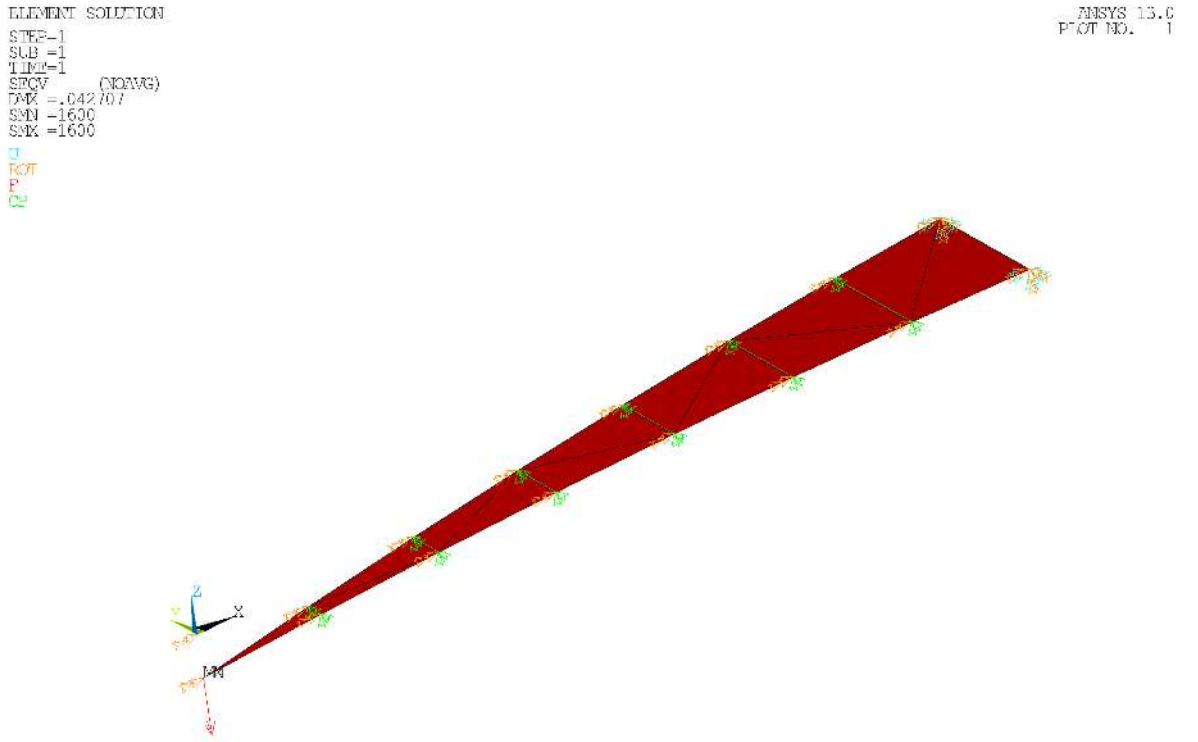

Figure 5.1: Static verification case using SHELL181 elements.

The target values are -0.042667 *in* deflection and 1600 *psi* maximum stress. Like it can be seen in

Figure 5.1, the results obtained are -0.042707 *in* and 1600 *psi*, revealing very good agreement with the expected values. The green arrows represent the nodal coupling to assure symmetry, while the orange arrows are the rotation restriction; the cyan are the zero displacement condition to fix the plate. The red arrow is the load applied.

5.3 Transient Test

The only available transient example is the VM265 [45]. It is a shock case in which an elastic rod with an initial velocity is impacting a rigid wall. Theoretically, if the rod is ideally elastic and the impact is elastic, the kinetic energy should keep constant and the rod should invert the movement with the same velocity.

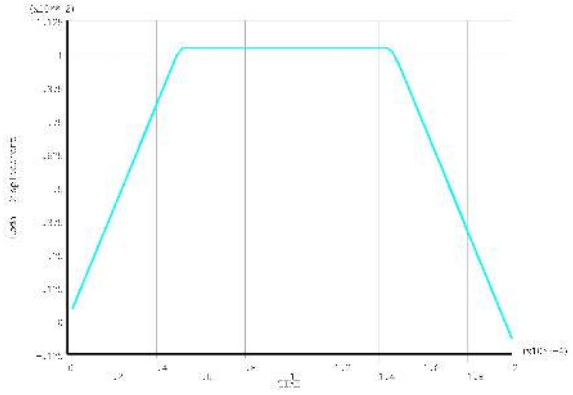

(a) Nodal displacement

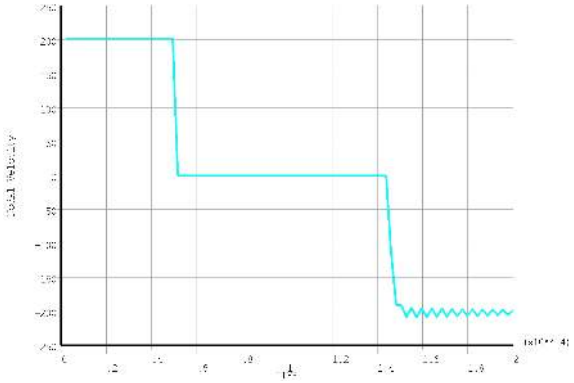

(b) Nodal velocity

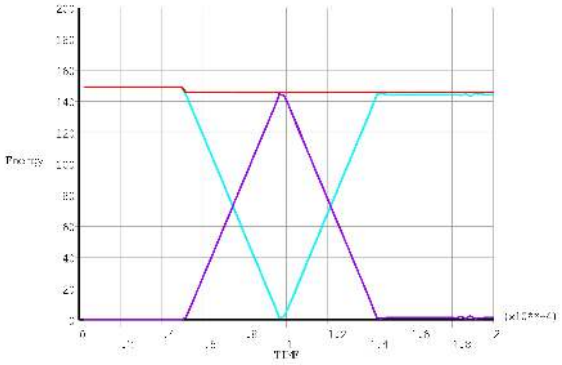

(c) Total Energy (red), Strain Energy (purple) and Kinetic Energy (Cyan)

Figure 5.2: Transient verification case using SHELL181 elements (imperial units used here).

In Figure 5.2(b), on can see that the final velocity is very close to the target, but still oscillating. Furthermore Figure 5.2(a) makes it clear that the rod describes, approximately, a symmetrical movement after the impact. By summing up the Strain and Kinetic energies, which are the only ones issued in the example, one gets the total energy, which is plotted in red in Figure 5.2(c). In the moment of the impact, there is a little loss of energy, making it not being totally elastic. The error is however very small.

5.4 Convergence Study

A final test is here done for the aircraft wing that will be used later for the aeroelastic computations. A symmetric wing with a NACA 0010 airfoil and an aspect ratio $\mathcal{R} = 4$. Two spars are introduced inside the skin at 0.3 and 0.7 chord distance from the leading edge (Figure 5.3).

The material used is steel with $E = 200\ GPa$, $\nu = 0.3$ and $\rho = 7800\ kg/m^3$ and the thickness is 10 mm for all surfaces.

The boundary conditions are zero displacement and rotation for all nodes at $y = 0$ (wing root section), being y the spanwise coordinate and also two nodal forces of 5000 N each at the wing tip at the nodes which connect the skin and the spars (see Figure 5.3).

Since a target value for the maximum displacement is not available, a mesh study is made for this static problem. Four different meshes were studied: 16×10, 32×20, 64×40 and 128×80. These numbers represent the number of panels of the skin in the form *chordwise* × *spanwise*.

Table 5.1: Mesh study for the wing steady test.

Mesh	Displacement [mm]	Deviation
16×10	-5.387	4.1%
32×20	-5.219	0.8%
64×40	-5.186	0.2%
128×80	-5.177	0.0%

Table 5.1 contains a summary of the results. The displacement values are the maximum values for each case. A deviation of the results is calculated in relation to the finer mesh, using

$$deviation = \frac{-5.177 - disp}{-5.177}, \tag{5.1}$$

where *disp* is the maximum displacement (in millimeters) for the mesh which is being calculated. Using this parameter, it is concluded that the coarser mesh is a little worse having a considerable deviation of 4.1%. On the other hand, the results of the other meshes deviate less than 1% from each other. Therefore, a mesh having 32×20 panels proves to be a good approximation and still cheap in terms of computational cost.

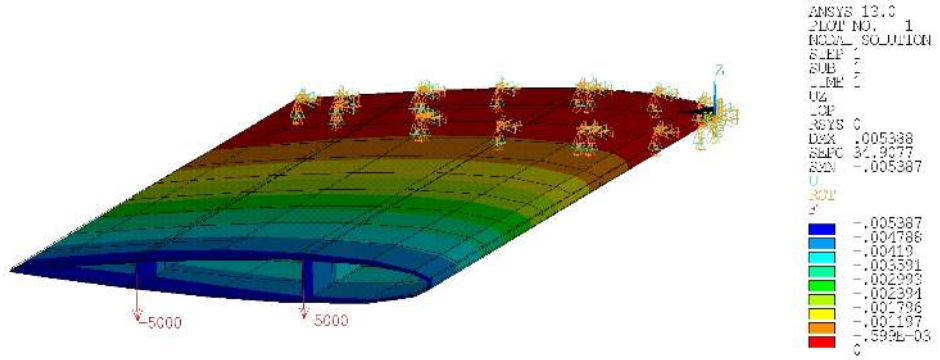

(a) 16x10 mesh

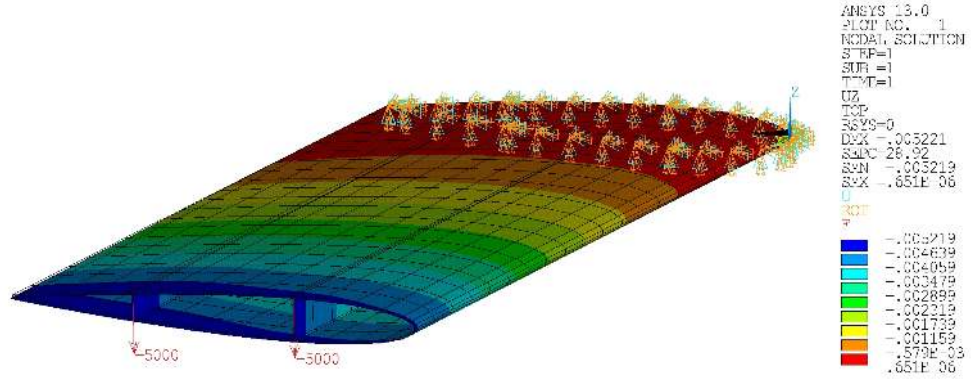

(b) 32x20 mesh

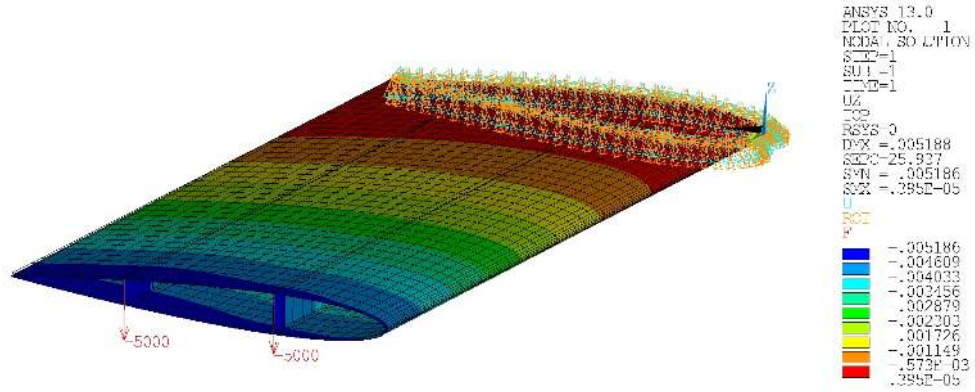

(c) 64x40 mesh

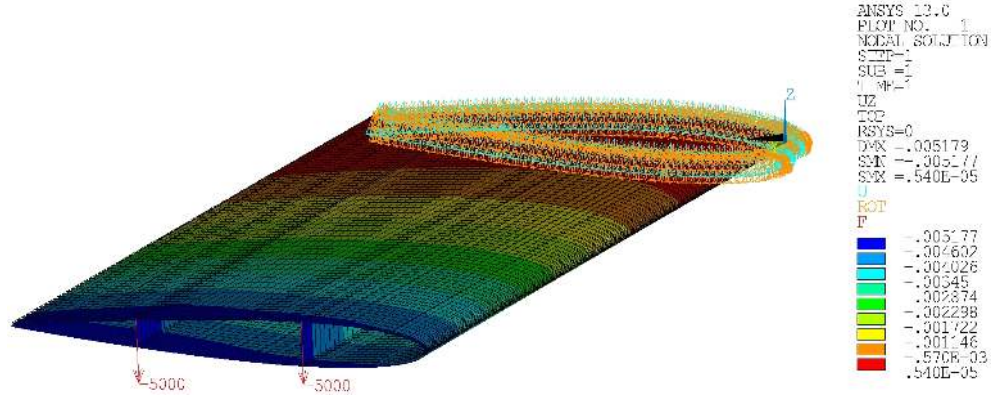

(d) 128x80 mesh

Figure 5.3: Static test using a wing with two nodal loads of $5000\,N$ (comparison made from coarser to finer mesh).

Chapter 6

Computational Aerodynamic Analysis

Following the theory presented in Chapter 3, one can now proceed with the implementation of a panel method code to perform calculations of aerodynamic flows.

Nevertheless, it is firstly important to make an historical review of those methods making it possible to use previous researches and conclusions as a starting point of the present study.

Table 6.1: Chronological list of some three-dimensional panel methods and their main features [1].

Method	**Year**	**Geometry of panel**	**Singularity distribution**	**Boundary conditions**
Douglas-Neumann	1962	Flat	Constant source	Neumann
Woodward I	1966	Flat	Linear source / Constant vortex	Neumann
USSAERO	1973	Flat	Linear source / Linear vortex	Neumann
Hess I	1972	Flat	Constant source / Constant doublet	Neumann
MCAIR	1980	Flat	Constant source / Quadratic doublet	Dirichlet
SOUSSA	1980	Parabolic	Constant source / Constant doublet	Dirichlet
Hess II	1981	Parabolic	Linear source / Quadratic doublet	Neumann
PAN AIR	1981	Flat	Linear source / Quadratic doublet	both
VSAERO	1982	Flat	Constant source / Constant doublet	both
QUADPAN	1983	Flat	Constant source / Constant doublet	Dirichlet
PMARC	1987	Flat	Constant source / Constant doublet	both

In most of the literature, the work developed by J. Hess and A. Smith in the McDonnell-Douglas is considered the cornerstone in the panel methods implementation and their method, the so called *Hess-*

Smith Panel Method, is the first truly practical method [46]. They started firstly with sources to calculate potential flows around non-lifting bodies and then added vortexes to introduce the lift force.

Table 6.1 presents some of the first panel method codes created and used in industry applications. There one can have a perspective of the evolution of the programs and the efforts from the researchers to improve results by changing the boundary conditions, the order (constant, linear, quadratic, etc.) and type (source, doublet or vortex) of the singularity and the geometry of the panel. Those developments were naturally only possible with the increase of the processing capabilities of computers.

In the 90 decade, more progresses were made in the mathematical formulation, creating the so called higher order panel methods (see Table 6.2). One example is the method presented in [2] which uses splines to interpolate the geometry and arbitrary doublet distributions (the distribution of each singularity is not prescribed but instead calculated and so variable).

Table 6.2: Chronological list of some high order panel methods and their main features [2].

Method	**Year**	**Dim.**	**Geometry of panel**	**Singularity distribution**
Johnson	1980	3D	Quadrilateral	Linear source
Cabral et al.	1990	2D	B-spline curves	B-spline curves source
Hsin and Kerwin	1993	2D	B-spline curves	B-spline curves source
Ushatov et al.	1994	3D	B-spline surfaces	B-spline surfaces source
Hughes and Bertram	1995	3D	Quadrilateral	Quadrilateral source
Kehr et al.	1996	3D	Quadrilateral	Linear source
Kouh and Ho	1996	3D	Arbitrary	Arbitrary source
Chuang	1999	2D	Arbitrary	Arbitrary source
Kouh and Suen	2000	3D	B-spline surfaces	Arbitrary doublet

The natural disadvantages of such methods are the need of well-defined geometries and the high computation effort. Therefore, it was decided to use the simpler formulations in this work.

6.1 Method choices

In Section 3.4, some reasons for the choosing of source and doublet for the singularity type were presented. It is still needed to make decisions about the boundary condition and the singularity order.

Katz and Plotkin [1] made some studies with constant, linear and quadratic singularities to compute flows around airfoils. One of the conclusions is that the boost of the order largely increases the computation CPU time. Furthermore, it suggests that an increase on the number of panels can achieve good results while still using a first order approximation. This will then be the approach used here.

In the VSAERO theory document [10], one can find some explanations regarding the choice of boundary conditions. In the case of a thick body, it proved to be important to give some concern to the internal flow, though it is not important to the results.

By comparison of the two main possibilities, Neumann and Dirichlet boundary conditions, the former considers that inside the body there is stagnation (Figure 6.1(a)), while the latter has the condition that the inside flow is equal to the onset flow (Figure 6.1(b)).

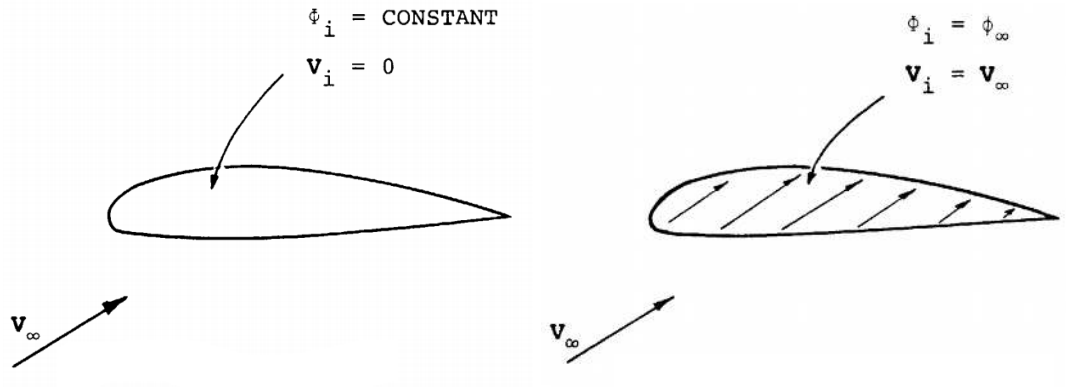

(a) Stagnation inside - Neumann (b) Zero perturbation inside - Dirichlet

Figure 6.1: Two different options in the boundary condition selection [10].

Tests made in [10], proved that the Dirichlet formulation has a better behavior, even for 'bad' panel arrangements. The explanation is that when passing through the boundary of the body, the potential jump from the internal to the external flow should be small, thus requiring a minimum of perturbation of the singularities. Clearly, the Neumann approach has a bigger jump causing the strength of the singularities to be much higher. Moreover it is emphasized that this only applies for thick bodies. If the object studied is a plate or a thin body, then the Neumann boundary condition is pretty adequate and that is why the VSAERO program has both boundary conditions (Table 6.1). In this work, the main topic of study are aircraft wings, so the Dirichlet boundary condition is implemented.

6.2 Program Development

Coming back to the topic Aeroelasticity (Section 1.2), one can have static and dynamic phenomena. So, it will be needed to compute both steady and unsteady flows while performing aeroelastic analysis.

Therefore, and also to obtain some experience in the panel method implementation, it was decided to start with the simple two-dimensional steady program and to proceed step by step to the final unsteady three-dimensional goal. Figure 6.2 shows all the four steps.

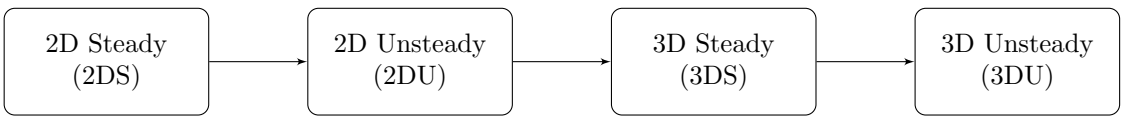

Figure 6.2: Sequence of panel method program development.

For this task, the software MATLAB is chosen because of its simple and user-friendly interface, easy matrix manipulation and useful plotting abilities.

For simplicity, the programs will be referred by the abbreviations inside brackets shown in Figure 6.2.

The source from where the code is based is once more Katz and Plotkin [1], which has in its appendix many panel method programs coded in FORTRAN language.

6.2.1 Two-dimensional Steady Program

In this case, the coordinates of any airfoil are used to build the panels. Each panel contains a constant source and a constant doublet, calculated in relation to the collocation point, the geometric center of the panel.

The wake is approximated with only one panel which goes from the trailing edge (collocation point) to infinity (Figure 6.3).

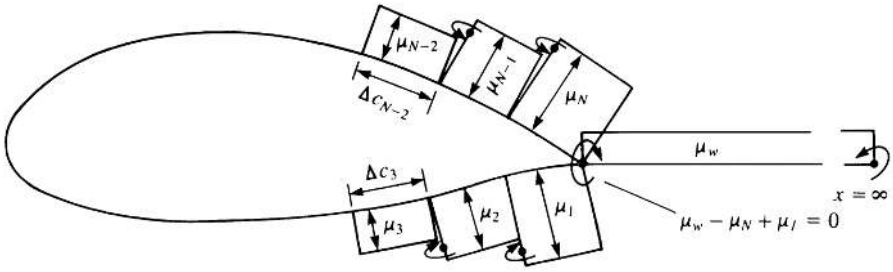

Figure 6.3: Wake panel considered in 2D steady calculations [1].

This panel has only a constant doublet since it has no thickness (so the source strength is zero). The doublet strength is simply obtained from the Kutta condition (3.41).

The panel coordinates are obtained with the help of the software XFOIL [47], which has an algorithm to interpolate coordinates with splines. It also creates a proper panel sizing, shorter close to the trailing and leading edges.

To validate and verify program, a *Kármán-Trefftz* airfoil was used. It is result of the transform of a circle in the ζ-plane to the physical z-plane, similarly to the *Joukowski transform*, called *Kármán-Trefftz transform*. Airfoils from this family have a non-zero angle between the upper and lower surfaces of the trailing edge, while the Joukowski airfoils have a cusped trailing edge [48].

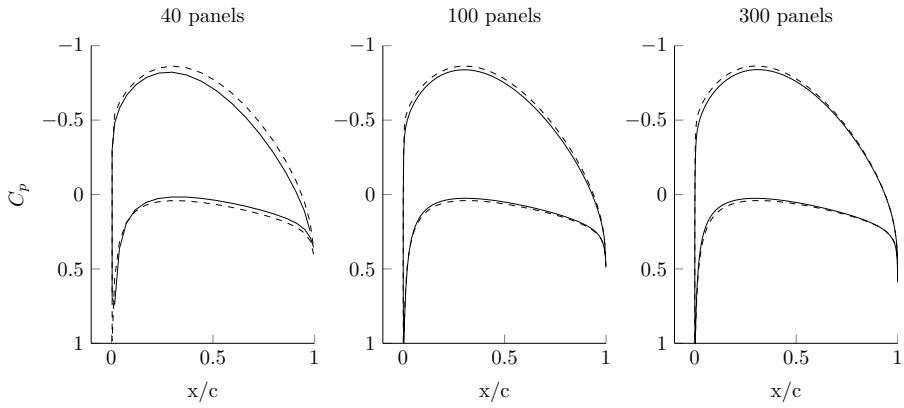

Figure 6.4: Kármán-Trefftz airfoil pressure coefficient for $\alpha = 2°$ (analytical solution in dashed lines and computational numerical solution in solid line).

The Kármán-Trefftz transform is equal to

$$z = n\frac{\left(1+\frac{1}{\zeta}\right)^n + \left(1-\frac{1}{\zeta}\right)^n}{\left(1+\frac{1}{\zeta}\right)^n - \left(1-\frac{1}{\zeta}\right)^n}, \tag{6.1}$$

where n is related with the trailing edge angle α and ζ and z are imaginary numbers.

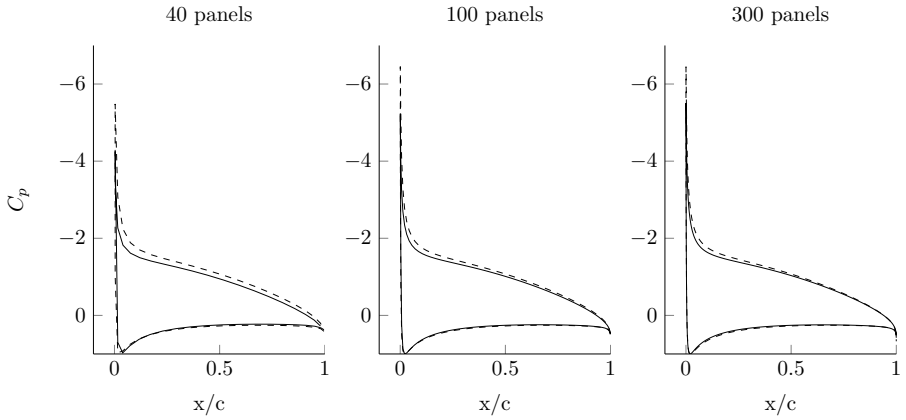

Figure 6.5: Kármán-Trefftz airfoil pressure coefficient for $\alpha = 8°$ (analytical solution in dashed lines and computational numerical solution in solid line).

For both of them, in the two dimensional case, the problem has an analytical solution. Figures 6.4 and 6.5 illustrate the results. On average, 2DS is very close to the exact solution. Furthermore, the increase of the number of panels improves the quality of the numeric solution, which is a sign of good behavior of the approach. In Figure 6.5, 2DS fails to reach the suction peak, though it gets closer in the 300 panels case.

For comparison of the lift calculation, a similar computation of a NACA 0012 airfoil is made and the results compared with the XFOIL. For a 2 degrees angle of attack and 300 panels, the XFOIL gives a lift coefficient of 0.2426, while 2DS gives 0.2280 with 90 panels and 0.2372 in the same conditions. The difference is then very small and might be explained with the different approach of XFOIL, which uses a linear-vorticity streamfunction formulation [47]. Besides, XFOIL uses a trailing edge panel, while the present method uses the opened airfoil.

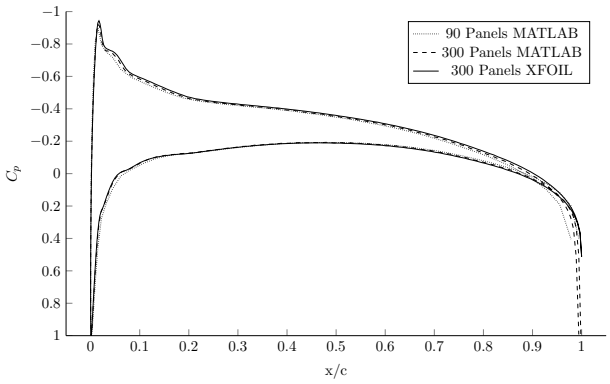

Figure 6.6: Pressure distribution for $\alpha = 2°$ for a NACA 0012 airfoil for the 2DS and the XFOIL program.

Figure 6.6 shows both pressure coefficient distributions. The results are quite good as far as the C_p distributions are almost coincident. To have a better C_l, a wake relaxation could be introduced, since here it is assumed as parallel to the chord. It is though not the goal of this work to develop a two-dimensional program.

6.2.2 Two-dimensional Unsteady Program

After the previous step, not many changes are necessary to convert the program to perform unsteady calculations. Basically, the kinematics and time step of the new movement, the body movement and the wake conditioning are the extra parts of the new code (see flowchart in Figure 6.7).

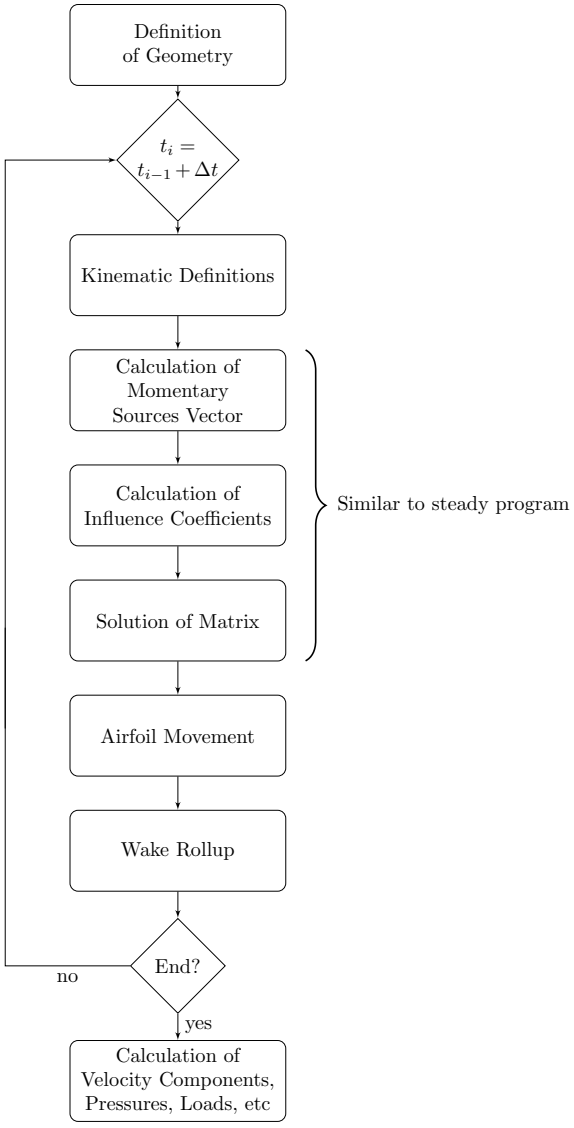

Figure 6.7: Scheme of the many stages in the 2DU panel method.

In this case, no body changing is considered, which means that the respective panels are always the same and so are the influences between them. However, also the strengths of the sources change here accordingly to the velocity angle.

Two problems were solved at this stage, to check the validity of the approach (particularly of the time-

stepping method for the wake presented in Section 3.4): a simple airfoil with moving with a constant angle of attack (steady problem) and the same airfoil with an heaving oscillatory motion.

In the first case, the verification of the results was simple made by looking at the pressure distributions and the lift coefficients. As expected, after some distance they stabilize and the results are the same as in the 2DS.

The oscillatory motion is defined with a sinusoidal function

$$X_0 = -U_\infty t \qquad Z_0 = h_0 sin(\omega t), \tag{6.2}$$

where h_0 is the heaving amplitude and ω is the frequency. The velocities are the derivatives in respect to time, so

$$\dot{X}_0 = -U_\infty \qquad \dot{Z}_0 = h_0 \omega cos(\omega t). \tag{6.3}$$

Here, (X, Y, Z) is the inertial frame of reference which is defined as the frame at $t = 0$.

It was not possible to find similar solutions in the literature, therefore the values for h_0 and ω were chosen in such a way that when the cosine is one, the vertical velocity is the same as for the 2 degrees angle of attack case studied in the steady program. By roughly comparing the lift values in that situation, one can say that the program is giving correct results (Figure 6.8).

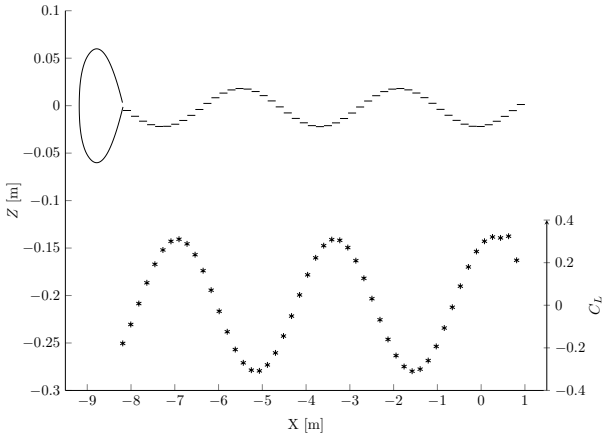

Figure 6.8: Oscillatory airfoil motion and respective lift coefficient (lines behind airfoil are wake panels convected with flow velocity).

6.2.3 Three-dimensional Steady Program

The next stage is three-dimensional expansion of the 2DS. Here one has a rectangular wing (assumed symmetrical) which is discretized in the chordwise and spanwise directions. The panels are then quadrilateral and flat. The singularities are still constant doublets and sources.

3DS demands some more calculations then the two-dimensional one, caused by the additional geometry considerations. So the program was completely taken from [1], which has a complete version in the FORTRAN language.

The wake shape is once more one panel in the chordwise direction (and the same quantity as the wing

in the spanwise direction), but now it cannot have infinite size. A value of three times the span size of the wing was considered enough.

To validate and verify the program, the experimental results as well as the numerical results of a similar panel method from Baltazar [37] (here referred as 3DBalt) are used in comparison with 3DS. To do that, pressure distributions are calculated in specific spanwise sections of the wing with $\mathcal{AR} = 4$ and NACA 0015 airfoil. Three sections are illustrated at 21.1%, 61.1% and 96.1% span. To have a fair comparison, a similar mesh 64×32 panels is used with a cosine distribution on the spanwise direction.

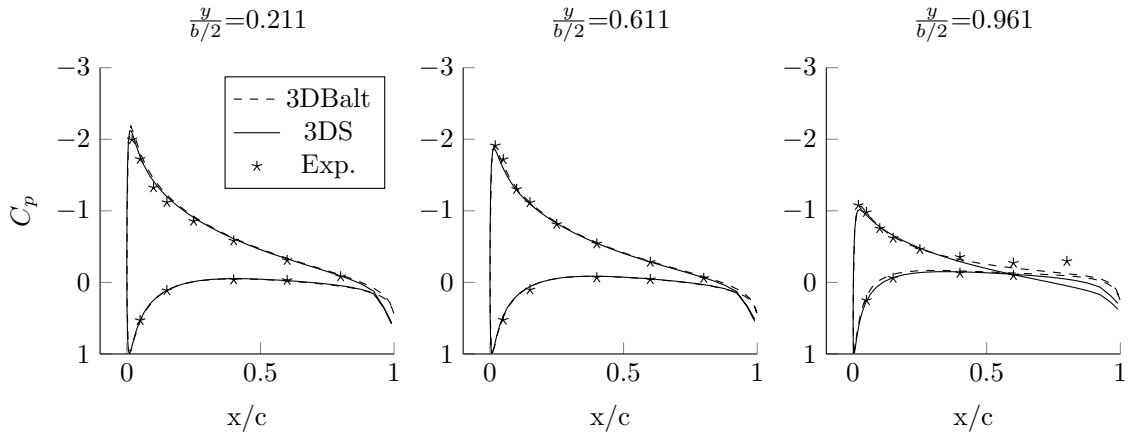

(a) Pressure distributions for the $\alpha = 8.5°$

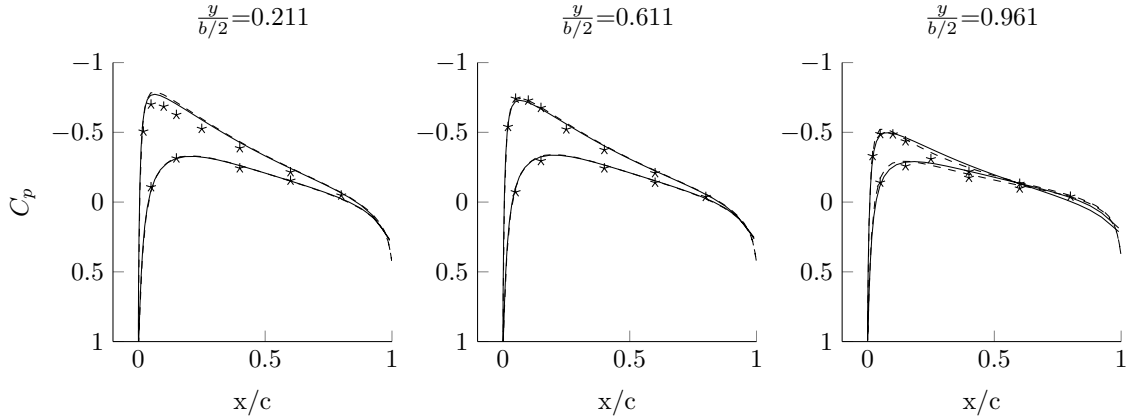

(b) Pressure distributions for the $\alpha = 2.5°$

Figure 6.9: Comparison of pressure distributions for 3D steady case.

In Figure 6.9, 3DS shows a good approximation of the experimental results, even at the wing tip. The consequence of the use of a linear Kutta condition can be clearly seen here, since 3DS shows an opened contour at the trailing edge. In contrast, with a converged solution using the iterative pressure Kutta condition, 3DBalt exhibits a fully closed curve.

Moreover, it is presented in Figure 6.10 a comparison of the non-dimensional circulation (or potential jump) of the wake, which shows good accordance of both panel methods. Herein, the cosine spanwise discretization makes the difference since the circulation changes closer to the wing tip, while it is almost constant close to the wing root. In this case, a wing with $\mathcal{AR} = 4$ and NACA 0010 airfoil was simulated at $\alpha = 2.5°$ and $\alpha = 8.5°$.

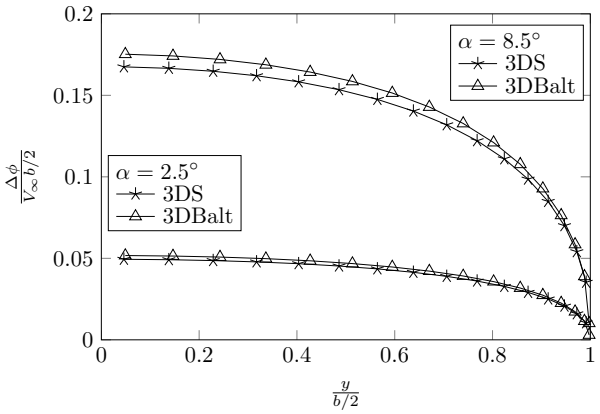

Figure 6.10: Comparison of the potential jumps along the span of the wing.

For the previous configuration, applying an 6° angle of attack, also the lift and drag coefficients were evaluated for different meshes and they are presented in Table 6.3.

Table 6.3: 3D steady results comparison for different meshes.

Mesh (chordwise×spanwise)	3DBalt		3DS	
	C_L	C_D	C_L	C_D
16×10	0.1082	0.0039	0.08842	0.0038
32×18	0.1024	0.0034	0.09376	0.0064
64×34	0.1002	0.0032	0.09572	0.0074
128×66	0.0993	0.0031	0.09632	0.0079

The results are close between programs. However, while the refinement approximates the lift coefficient results from 3DS to 3DBalt, it increases the difference on the induced drag predicted by 3DS as well.

6.2.4 Three-dimensional Unsteady Program

The evolution from steady to unsteady is very similar from two to three dimensions. Figure 6.7 applies also here as well.

Here, the same time-stepping approach is also used. The wake panels are moved with the instantaneous flow velocity. In the case of a oscillating wing, its velocity is included as well.

The program was tested with a steady problem (as it was done in two-dimensional program), which revealed correct results, compared with Table 6.3. Here, besides the wing and wake discretization, the time discretization has also influence on the results. In Figure 6.11, an illustration of the resultant panels for the same $\mathcal{AR} = 4$ wing with NACA 0010 airfoil is shown.

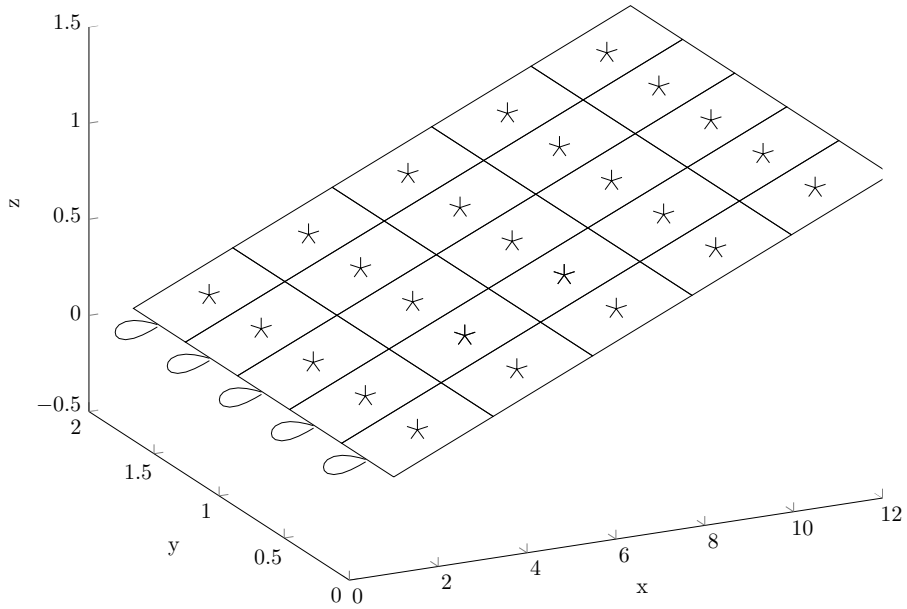

Figure 6.11: Example of application of the unsteady program in a 6° angle of attack and a time discretization of 5 steps each step of 2 seconds (marks are wake collocation points).

Chapter 7

Aeroelastic Analysis Framework

In the previous chapters, the two main domains of a FSI problem were developed. Moreover, the Chapters 2 and 3 were dedicated to the theory behind the structural and fluid flow analyses, respectively. Chapter 4 concerned the several problems and solutions while coupling the two referred domains to obtain correct and accurate results.

After that, the application of the theory was addressed. In Chapter 5, some special features needed for the structural analysis of an aircraft wing were discussed and, in Chapter 6, a program for the aerodynamic analysis was created and validated with wind tunnel data.

It is then now time to put it all together to achieve the main goal of this thesis, perform aeroelastic analysis. In this chapter, further particularities of the coupling process will be explained and also some remarks about the methods and approaches that were chosen for the task.

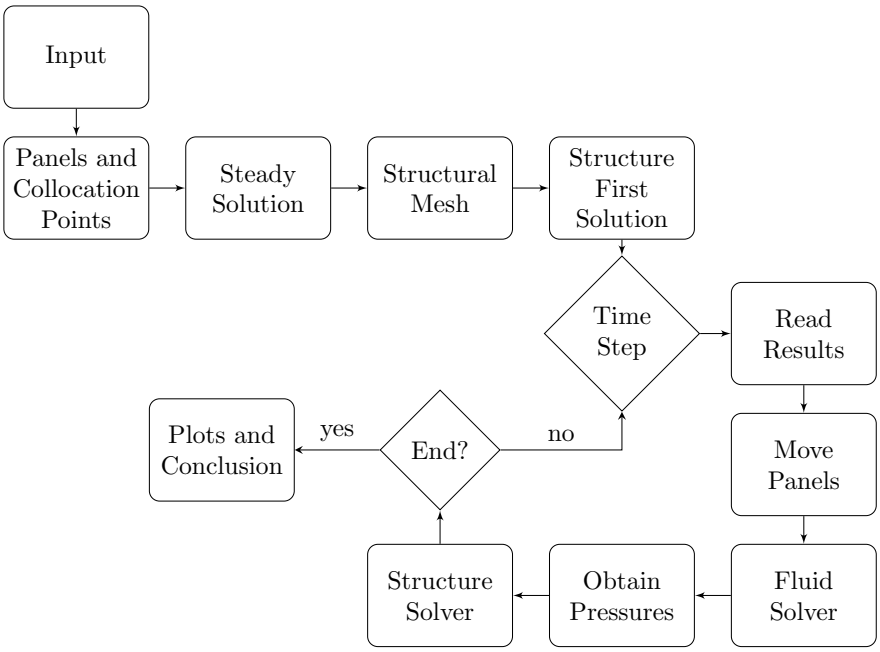

Figure 7.1: Flowchart illustrating the aeroelastic calculation process.

Figure 7.1 presents the main structure of the aeroelastic framework. Further explanations are given

in the next sections.

7.1 Input

Several input constants are here enumerated and organized in categories:

1. **Fluid** - density, velocity and angle of attack;
2. **Wing** - chord at wing root and tip, x and z coordinates of the point on the leading edge on the wing tip (sweep and dihedral);
3. **Mesh** - file with the airfoil coordinates (number of points dictates the number of chordwise panels), number of spanwise panels;
4. **Steady Wake** - initial steady wake angle and length;
5. **Structure** - spars location, material properties, thicknesses, presence of ribs;
6. **Time** - time step size, number of steps;
7. **Method** - Choice of CSS or ISS procedure and time discretization method for the fluid domain, Backward Euler or Crank-Nicholson method.

After this stage, the first pressures are obtained from a steady solution from 3DS using the parameters here defined.

7.2 Pre-processing

This part covers the four steps after all the inputs are established. First of all, the wing panels and collocation points are stored in the respective variables and 3DS program is applied to introduce a steady solution for the specified angle of attack. This will produce the first set of loads.

Next, two lists are created in such a way that APDL is able to read it. One contains the nodes and their position and the second contains the elements and the information needed (nodes, material, section number, element type, and frame of reference). Those lists are saved in files and read in APDL.

Though the ribs are simply located at the existing panel borders, the spars are placed exactly where the user specifies. So a special routine was created to check if the placement is coincident with an existing node. If not, the element is divided into two and the consequent new elements added. This verification is done for every span position of the mesh.

The full transient solver from APDL is here applied (see Section 2.4). The difference of the first solution is that at the beginning the wing is at rest. In the subsequent ones, a set of initial conditions (velocity and displacement) is applied using the values of the last substep of the previous structure solution. This assures that one has continuity of the movement.

Essentially, the mesh input is always the same, only the initial conditions change.

Figure 7.2 shows an example of a load case applied on a wing with $\alpha = 4°$, obtained after the pre-processing stage. The elements of the structural mesh were created in such a way that the normals of the skin elements are pointing outwards by the right-hand rule. However, APDL plots the pressures applied from inside, causing this weird perspective of Figure 7.2.

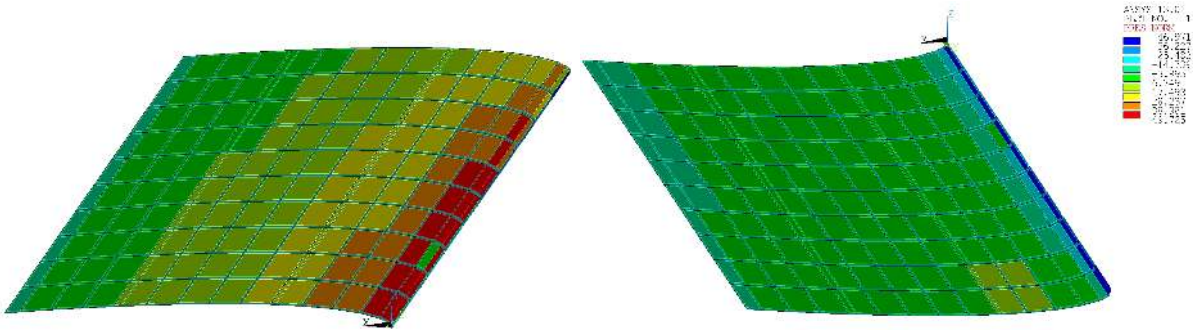

(a) Upper or suction surface

(b) Lower or pressure surface

Figure 7.2: Example of a load case on an aircraft wing (legend valid for both images).

The spanwise rows of smaller elements are caused by the spar location, being still applied the correct pressure of the panel.

Time substeps are used here to be able to follow the movement more precisely, since all the values at all substeps are saved in a file and later imported to MATLAB and plotted for analysis.

7.3 Time Cycle

After the initialization of the computation, the program enters in a cycle in the time domain. It begins by reading and sorting the results file wrote by APDL, that contains the displacements and velocities for all nodes in all the time substeps computed in this visit.

Next, the aerodynamic mesh is updated and introduced together with the previous wake positions and strengths into a fluid solver. The box Move Panels in Figure 7.1 is where the situation changes accordingly to the method chosen. Like it was presented in Chapter 4, if using CSS then $\vec{x}_{n+1} = \vec{u}_n$, which means the panels just move with the displacement. If, however, ISS is used, then $\vec{x}_{n+1/2} = \vec{u}_n + \frac{\Delta t}{2}\dot{\vec{u}}_n$, which means also the velocity is used.

The mentioned fluid solver is nothing more than the 3DU program adapted to a function which receives the previous state as input and gives back the velocity field in the next time step.

The pressure field is then computed using Equation (3.31) and pressure vector are obtained from the dimensionalization of C_p with $\frac{\rho}{2}V_\infty^2$.

This cycle simply continues the solution until the desired time limit is reached.

7.4 Post-processing

When the last cycle is completed, the last set of results is read. In this moment, some plots can be done to observe the behavior of the wing during the movement. A possible and simple analysis is to plot the

z-coordinate of two nodes from the last spanwise section, namely one at the leading edge and another one at the trailing edge. This way it is possible to watch the bending and torsion motions.

Figure 7.3 shows another possible post-processing manner which tracks the evolution of the wake during the whole calculation. This is the (X, Y, Z) frame and the wake is being convected with the flow velocity. The last panel row is wider because it represents the steady initial solution.

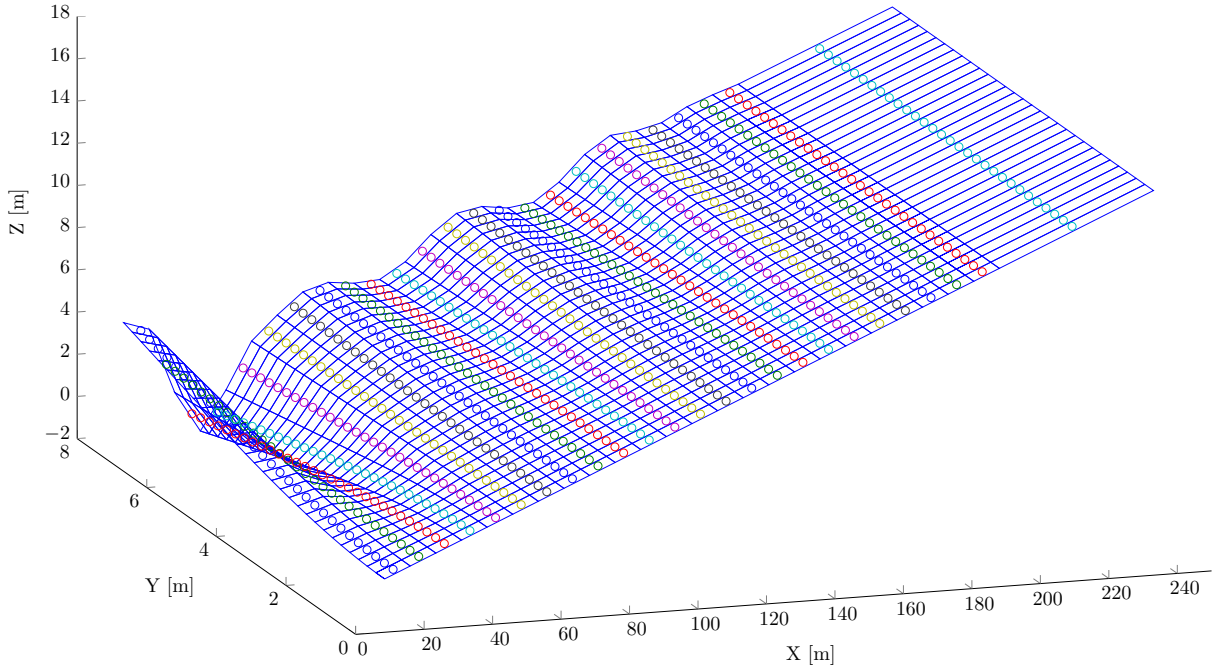

Figure 7.3: Example of the wake panels after 25 time steps (blue lines are the panel edges and colorful circles are the respective collocation points).

Chapter 8

Aeroelastic Analysis of Aircraft Wings

In Chapter 7, the final assembly of the aeroelastic program was presented. Finally, the critical point of this thesis will be reached by the computation of aeroelastic behaviors.

Firstly, for a wing with a certain structure, two aeroelastic computations will be done, one dynamic and another static. The former is used later as a reference for comparisons. The latter is simply to check the physical truth of the framework created.

However, in order to justify some of the decisions which will be made later on, some comments are given about the first tests done when the procedure described in Chapter 7 was finished.

8.1 First Experiences

In the first approach, it was decided to use a wing with the skin made of light wood and the spars made of steel. Xie et al. [49] does use something similar but with a beam instead of spars. However, this wing proved to be very weak. Even for low angles of attack and low velocities, the wooden skin was always severely deformed after some oscillations. Since buckling analysis is out of the scope of this work, this wing setup was discarded.

A next try was to use steel for all wing, but using the skin much thiner than the spars. The movement was still very unstable, even using a fine mesh. This behavior is naturally explained by the absence of some of the typical structural elements of the aircraft wing such as the ones illustrated in Figure 1.6. Some of the typical structure elements of the aircraft wings are missing, namely the stringers which support the thin layer of skin, avoiding its deformation. To compensate this miss, exaggerated skin thicknesses will be used in the following sections, like it was already done in Section 5.4.

The ribs are used to maintain the shape of the wing section and assist in transmitting external loads to the wing skin [5]. This could be the solution for the problem, however all tries with more or less ribs and with a skin 2 mm thick revealed poor results.

The consequence of having such thick skin is that the dynamic behavior of the wing will be influenced

mainly by the skin. However, as it will be showed late, the spar locations will have influence on the dynamic behavior of the structure.

The grid was chosen having two things in mind: to reduce the time needed for each time step and to have a level of discretization good enough to generate accurate results. What was spotted in the first tests was that for meshes with 16 and 32 chordwise panels, the fluid solver was calculating huge pressures in a few panels, which sort of 'punch' the structure and destroy all the movement.

The grid 64×40 never showed this problems, being however quite expensive since each cycle takes approximately 300 seconds with the computer used. So the number of spanwise divisions was reduced to 30, which saved 150 seconds per cycle and revealed no problems for the fluid solver. Using this mesh, a computation of 70 cycles takes between 3 and 4 hours (using an Intel Core i7-2670QM CPU). The mesh 128×80 takes more than one hour per cycle, which would make the computation to be very expensive. Moreover several time steps were tried, being 0.1 s the option that, without losing information, spares more computation time. Using smaller values the results were macroscopically similar, having considerable oscillations.

Referring to the time integration method for the fluid domain, the Crank-Nicholson method tested for the reference case which is presented next, caused the pressure load to oscillate quite heavily. Therefore, all the presented results were obtained using the Backward Euler method.

The aeroelastic procedure ISS was also tested, but it revealed to introduce a numeric damping, which caused the wing movement to be always convergent, even for very high velocities. Hence, the CSS procedure will be preferred for the further computations.

One last word is given about the load consistency issue that was enunciated in Section 4.3. In APDL, it is possible to obtain to total forces applied and a comparison was made with the force generated in the fluid solver and the accordance was reasonable. Since in this work the fluid and structural meshes will be the same, the transferences between domains is no longer a problem and no interpolating or mapping framework is needed. This is one of the big advantages of the panel methods compared to other fluid solvers.

8.2 Reference Case Input

The same input values used in the APDL static test from Section 5.4 are here applied, using a 64×30 mesh, $\text{Æ} = 15$, NACA 0010 airfoil, two spars at 0.3 and 0.7 chordwise location and the wing being rectangular with $c = 1$ m and no ribs (see Figure 8.1). Moreover, CSS procedure is applied using Backward Euler for the pressure time integration and Newmark in APDL for the structural time discretization.

The fluid density is assumed to be $\rho = 1$ kg/m^3 corresponding to an altitude of 1371 m at standard atmosphere conditions (considering a temperature offset of 20 $°C$), the angle of attack is $\alpha = 4°$ and the fluid velocity $V_\infty = 75$m/s. The initial wake angle is the angle of attack and its length is three time the wing span. The time step is set to 0.1 s.

Using this input data, a computation is done using the transient structural solver yielding a dynamic aeroelasticity problem. The results from this computation are referred as *Reference Case* (RC).

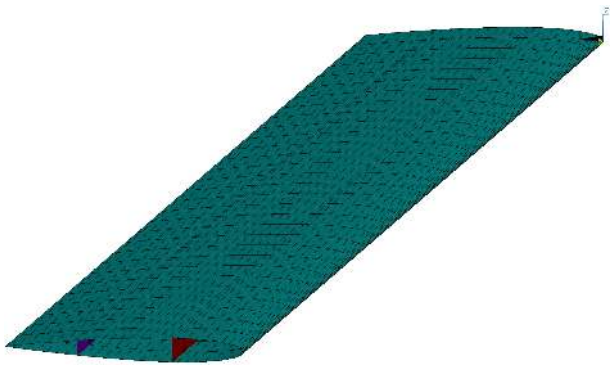

Figure 8.1: Structural model used for the aeroelastic calculations.

8.3 Aeroelastic Dynamic Computation

To be able to track the wing movement, several prints are taken during each structural step in APDL. The vertical movement of two nodes at the wing tip leading and trailing edges (like it was justified in Section 7.4) is plotted in Figure 8.2(a).

The nodal trajectory of both nodes is almost coincident so the torsion is very low. This is confirmed by Figure 8.2(b) that shows a maximal rotation of $1.2 \cdot 10^{-3}$ rad which means roughly $0.1°$. Microscopically, the rotational movement has a lot of oscillations, which are neither desirable nor expected. They may be result of too big time step or skin local and small buckling effects. Since the order of total rotation is very low, those oscillations appear to be quite big. Therefore, the signals were filtered and only the low frequency oscillations are showed in the upcoming figures. More details about the filtering process are found in Appendix B.

This macroscopically movement has the same period of the vertical displacement. When one is at the minimum displacement, it corresponds to the maximum rotation (positive rotation around Y is using the Right-hand rule, from Z towards X axis, also called nose-up) and vice-versa. So, the torsional movement seams to be damping the bending movement. However the increase of the wing maximal displacement shows clearly that this velocity is already higher than the flutter velocity.

Table 8.1: Period and frequency of the vertical movement of reference case.

Time [s]	Displacement [m]	Period [s]	Frequency [Hz]
0.2	0.06413	0.56	1.786
0.76	0.06633		
8.9	0.08486	0.58	1.724
9.48	0.08719		
16.42	0.11343	0.60	1.667
17.02	0.11363		

Using the peak values, the movement period and frequency are easily obtained. To obtain a consistent value, three values were used at the beginning, middle and end of the movement. The results are summarized in Table 8.1. Like it was expected, the frequency of the movement is nearly constant during all computation. If one counts the total number of peaks and divides by the respective time, the frequency

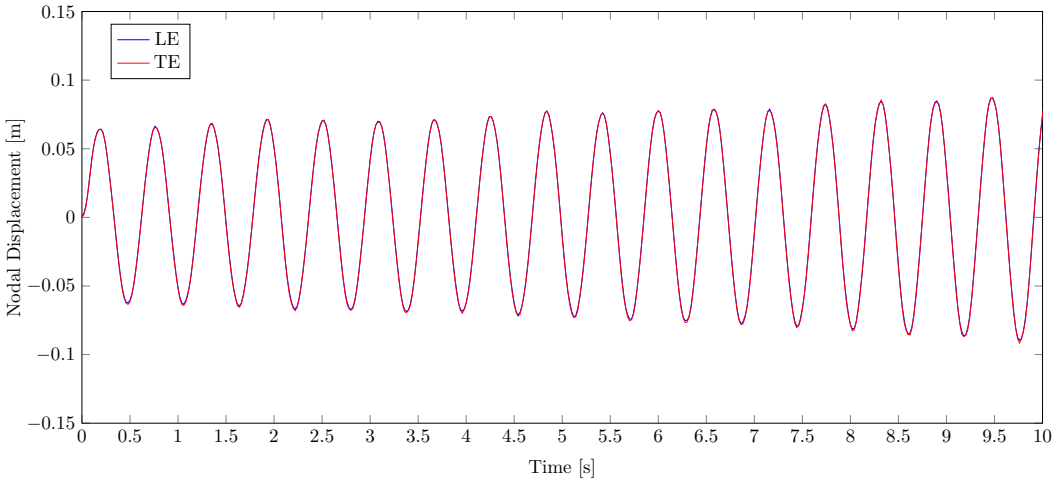

(a) Vertical displacement of LE and TE wing tip nodes.

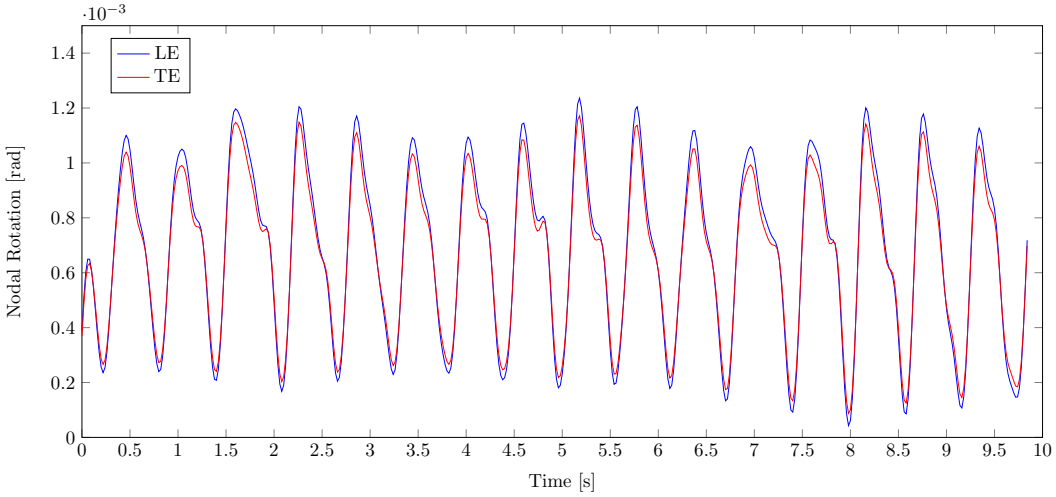

(b) Rotation of LE and TE wing tip nodes.

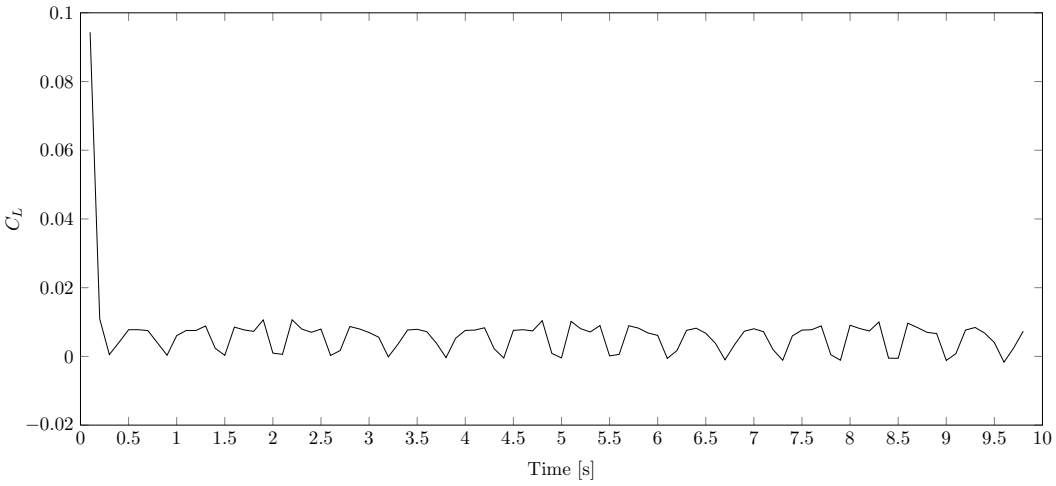

(c) Wing lift coefficient.

Figure 8.2: Aeroelastic reference results for the input values from Section 8.2.

obtained is 1.7 Hz, so that proves the constancy of the movement.

Table 8.1 also includes the displacement values at the peaks, which confirm the divergence of the

movement.

Figure 8.2(c) shows the evolution of the lift coefficient with the time. After the initial steady solution, the variation is not very significant, being however possible to see the oscillation caused by the wing movement, which varies with approximately the same frequency than the nodal displacement from Figure 8.2(a). Furthermore, lift positive peaks correspond to rotation positive peaks, which is physically correct.

Finally, the tracking of a complete period from the RC is showed in Figures 8.3 and 8.4. The difference between those are the time steps and the contours, which symbolize the Z-displacement in the former and the Y-rotation in the latter. Hereby, one can also confirm the nose-up position when the vertical displacement is minimum and nose-down when it is maximum.

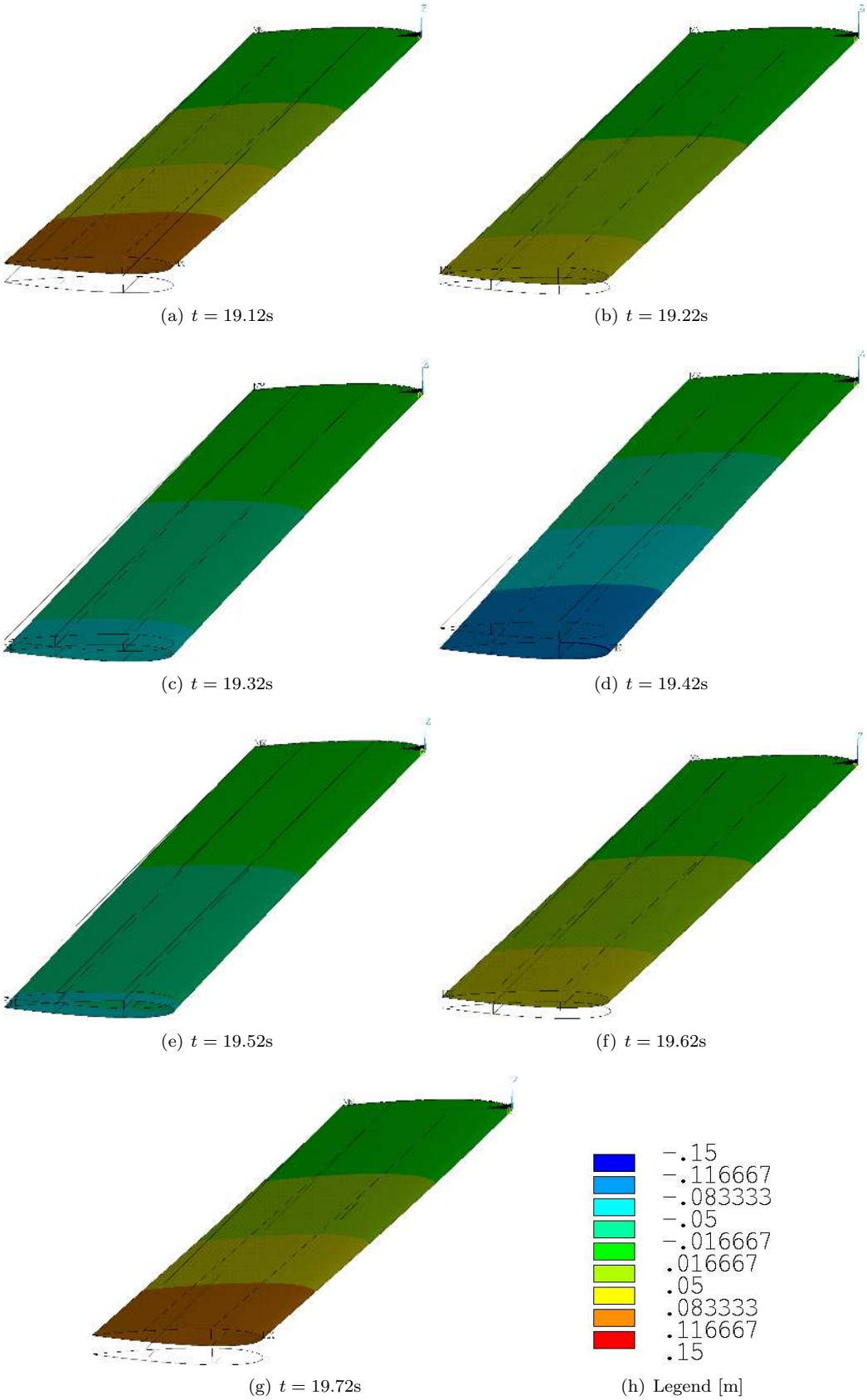

(a) $t = 19.12$s (b) $t = 19.22$s

(c) $t = 19.32$s (d) $t = 19.42$s

(e) $t = 19.52$s (f) $t = 19.62$s

(g) $t = 19.72$s (h) Legend [m]

Figure 8.3: Complete period of the movement using APDL prints (color contours give vertical nodal displacement on the Z axis) (8.3(e) is valid for all contours).

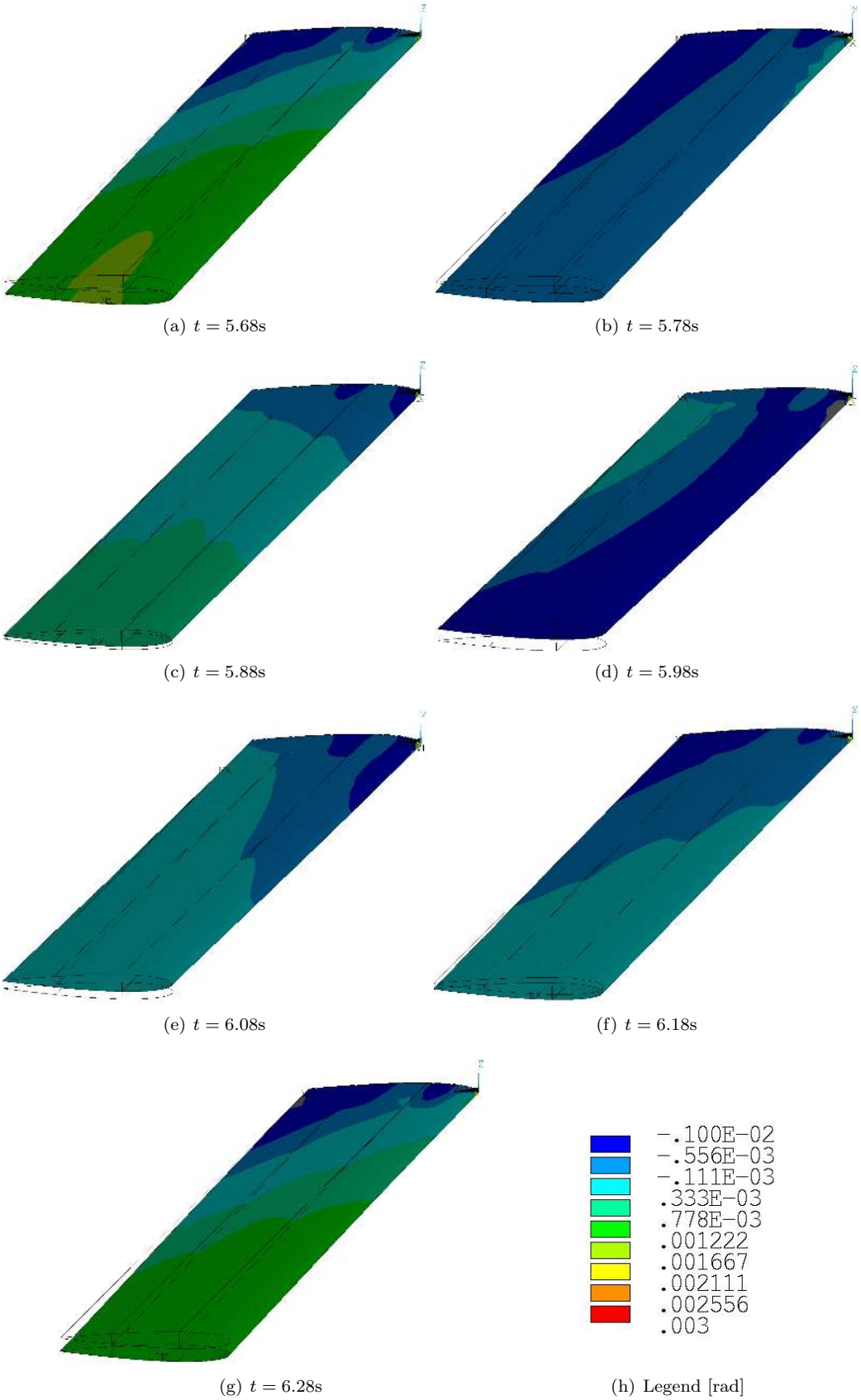

(a) $t = 5.68$s (b) $t = 5.78$s

(c) $t = 5.88$s (d) $t = 5.98$s

(e) $t = 6.08$s (f) $t = 6.18$s

(g) $t = 6.28$s (h) Legend [rad]

Figure 8.4: Complete period of the movement using APDL prints (color contours give nodal rotation about spanwise axis) (8.3(e) is valid for all contours).

8.4 Aeroelastic Static Computation

In this section, a different test will be performed using the same data from Section 8.2. However, for each time step, the structure will be solved as a static analysis yielding a static aeroelastic problem (in practice there is no real time, each cycle is one more static computation). This way, one eliminates the inertial forces, which shall cause the wing to converge to a stable position.

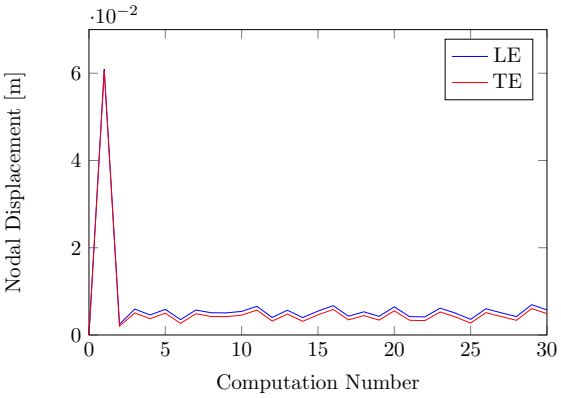

(a) Vertical displacement of LE and TE wing tip nodes.

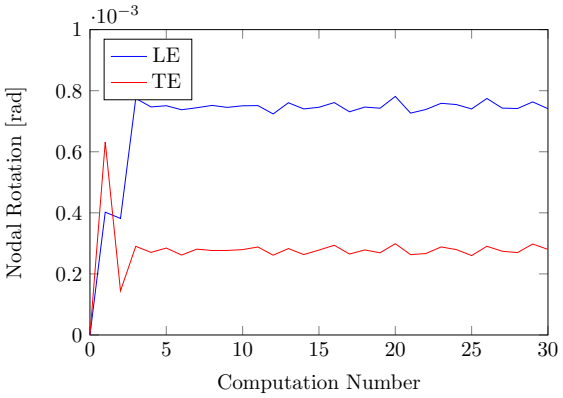

(b) Rotation of LE and TE wing tip nodes.

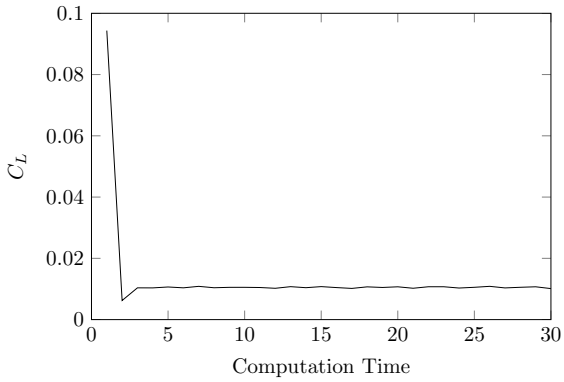

(c) Wing lift coefficient.

Figure 8.5: Results from RC solved with structural static solver from APDL.

Figure 8.5 shows exactly that behavior. After an initial oscillation, the structure goes to a stable position, only having very small movements after that. 30 computation cycles were more than enough to confirm that.

Chapter 9

Parameter Influence Studies

In Section 8.3, the dynamic aeroelastic behavior of a wing was summarized. Herein, further computations will be done having one input parameter changed. The results shall be plotted together with Figure 8.2 to study the influence of each of those parameters.

9.1 Free Stream Velocity

The first parameter to study is the free stream velocity. As it was seen, the RC is already beyond the flutter velocity. By reducing the velocity, one should be able to see when the movement starts to be divergent. Velocities studied are 60, 40 and 10 m/s. Figures 9.1(a) and 9.1(b) show the wing tip LE node behavior. The TE node was suppressed because its movement is almost coincident with the LE.

The graph for the 60 m/s is still smoothly divergent, while the 40 m/s has practically zero damping. So it is concluded that the flutter velocity is around 40 m/s. With the 10 m/s, the wing still oscillates but with displacements of the order 10^{-4} m, so it cannot be seen here.

In Figures 9.1(a) and 9.1(b), it is possible to see the bending-torsion coupling, since both movements have the same frequency, however opposite polarity (i.e. 180 degrees phase difference). Watching also 9.1(c), one can confirm that the positive rotation is a nose-up position, since the lift coefficient has also a maximum. Moreover, the lift has the same frequency of the rotational and bending movements.

Figure 9.1(c) also shows an interesting property: the velocity reduction increases the average C_L. This coefficient is obtained from the pressure coefficient integration, which is non-dimensionalized with the free stream velocity (see Equation (3.58)). So the larger the V_∞, the smaller are the absolute values from the second and third terms from (3.58) and the larger is the pressure coefficient. As it is known, the major part of the wing load comes from the suction side (examples in Figures 6.4 and 6.5), which means the more negative is the pressure, the higher the lift coefficient. So this detail is physically correct.

As it is expected, the frequency of the movement does not change with the free stream velocity. As it will be seen later, other parameters will have this effect.

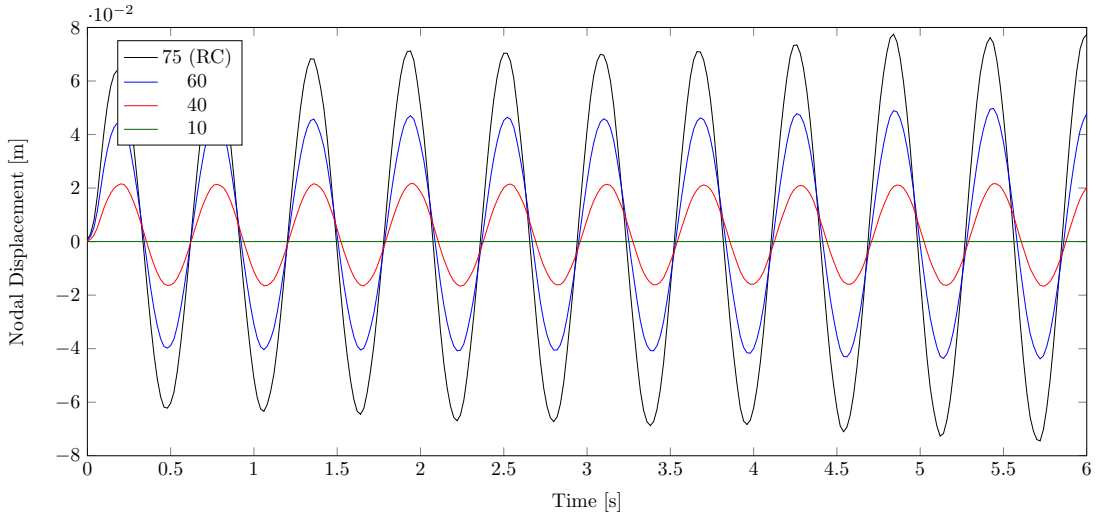

(a) Vertical displacement of LE wing tip node.

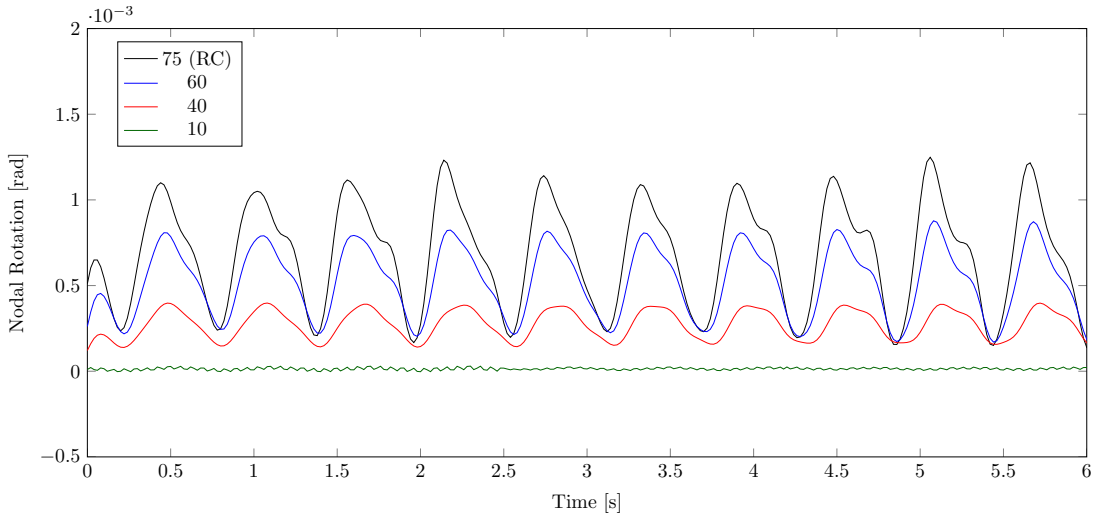

(b) Rotation of LE wing tip node.

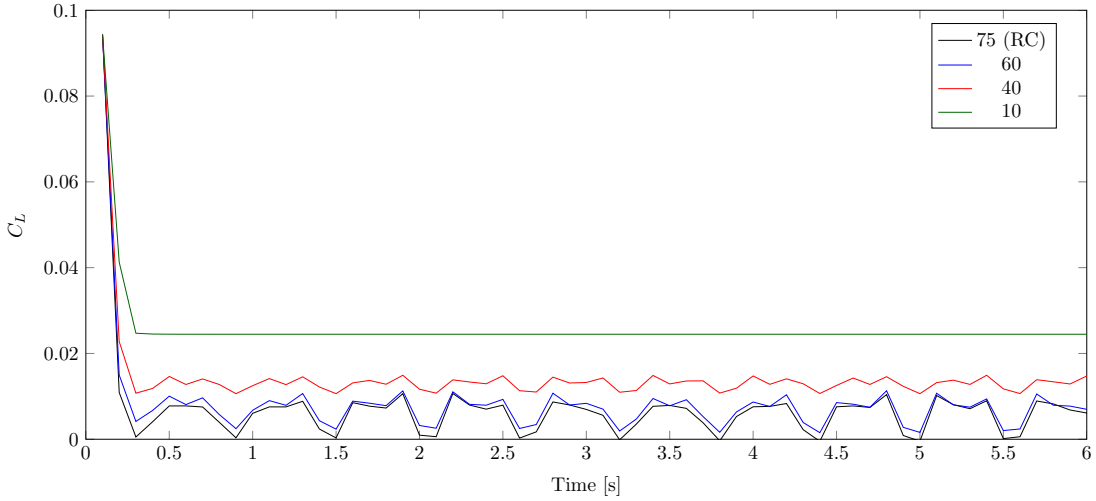

(c) Wing lift coefficient.

Figure 9.1: Influence of the free stream velocity [m/s] in the aeroelastic wing behavior.

9.2 Spar Location

The next test is made changing the location of the two wing spars. As it will be seen, by moving the spars in the chordwise direction towards one of the edges, one is changing the wing torsional stiffness, maintaining the bending movement frequency very similar.

Three computations were done with the spars at 0.7 and 0.9 chords, which means close to the trailing edge; 0.1 and 0.3, close to the LE; 0.45 and 0.55, closer to each other than the RC (0.3 and 0.7 chords).

In the first case, the wing movement is largely divergent and the vertical displacement reaches the order of meters in a few seconds, so it will not be plotted here. This result was expected since, in practice, what was done was to move away the twist center from the aerodynamic center (see Figure 1.3). This causes torsional divergence [5] and, consequently, also bending divergence.

Figure 9.2 shows the results for the other cases compared with the RC. 9.2(a) confirms that the bending frequency was not affected. However, by placing the spars closer to each other at the wing center, the flutter velocity increased and the nodal maximum vertical displacement is decreasing very slow in this case.

The lift coefficient is also not significantly affected, maintaining also the frequency accordingly to the displacement.

The big difference is the torsional movement when the spars are pushed towards the LE, which places the center of twist ahead of the aerodynamic center. As it can be seen in Figures 9.2(a) and 9.2(b), the bending movement is still similar but a torsional divergence with higher frequency appears.

9.3 Sweep Angle

Airplanes, and particularly jets, have very often a swept back wing for many reasons, for instance for reducing the effective velocity and avoiding shock waves in transonic flights, which increase the drag. However also the bending-torsion coupling will be affected. Therefore two swept wings were tested, one back-swept and the other forward-swept, both having the same sweep angle of 15°.

The bending movement does not differ too much from the RC, having a slightly lower frequency for both back- and forward-swept wings (Figure 9.3(a)). The difference comes in Figure 9.3(b), where the rotations will be higher. Moreover, the back-swept wing keeps in phase with the RC (positive rotation for negative displacement), while the forward wing is in anti-phase with the RC. The positive rotation for positive displacement will cause a local increase of the angle of attack, inducing stall. This is why the forward-swept wing is said to be unstable and is very rarely used in airplanes.

9.4 Skin Density

After making changes in the flow, in the wing spar and in the sweep angle, the next two parameters to change are related to material constants. Like it was stated before, the material changes in the spars did not affect significantly the wing dynamic behavior, so only the changes in the skin are presented here.

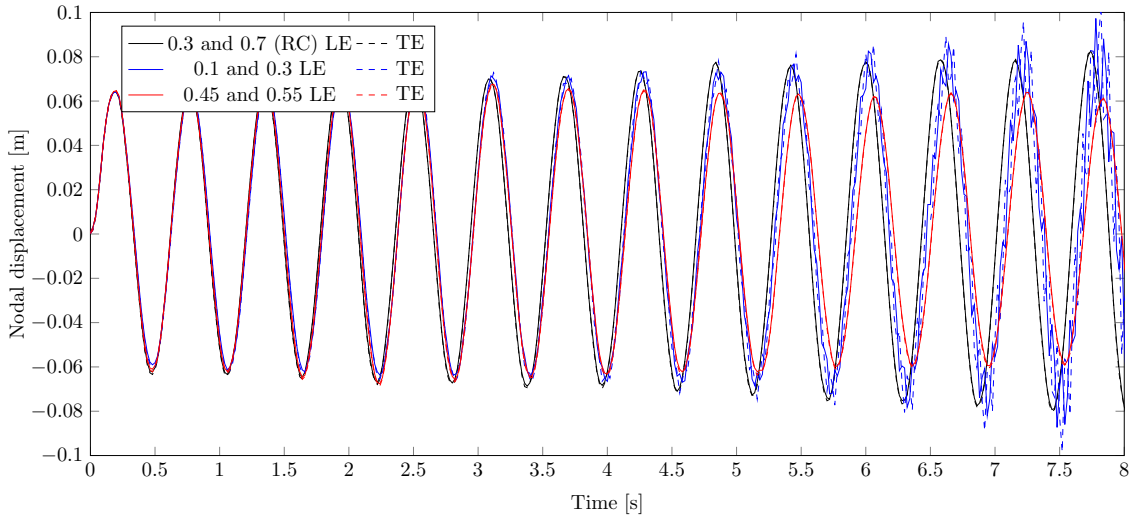

(a) Vertical displacement of LE wing tip node.

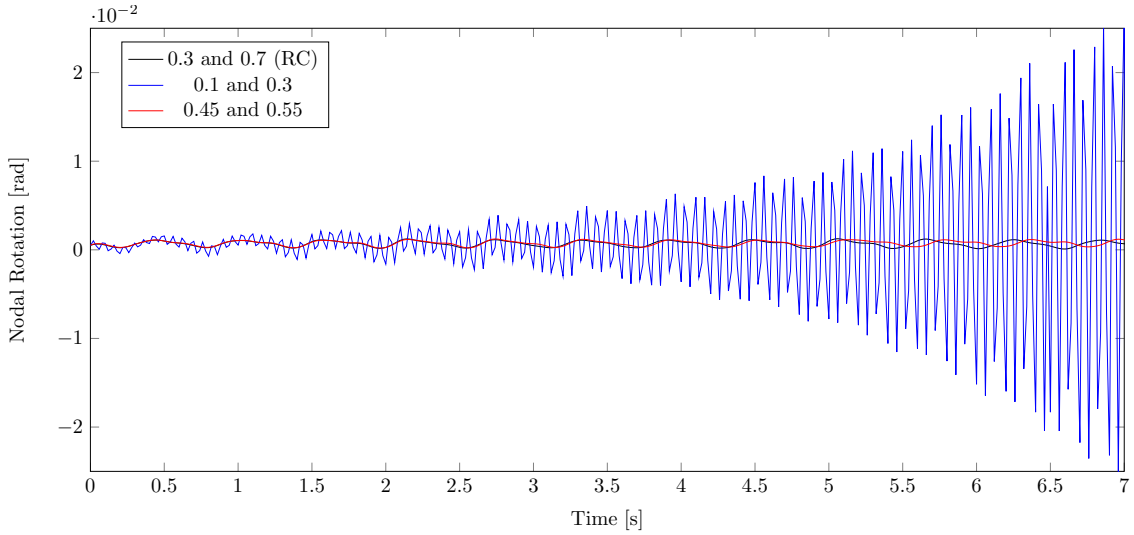

(b) Rotation of LE wing tip node.

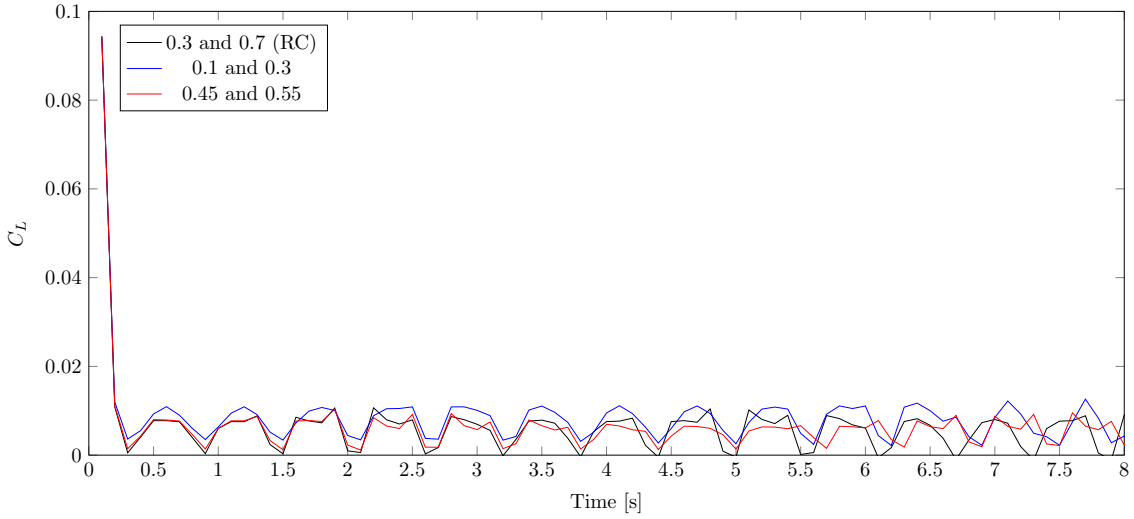

(c) Wing lift coefficient.

Figure 9.2: Influence of the spars location (measured in chords) in the aeroelastic wing behavior.

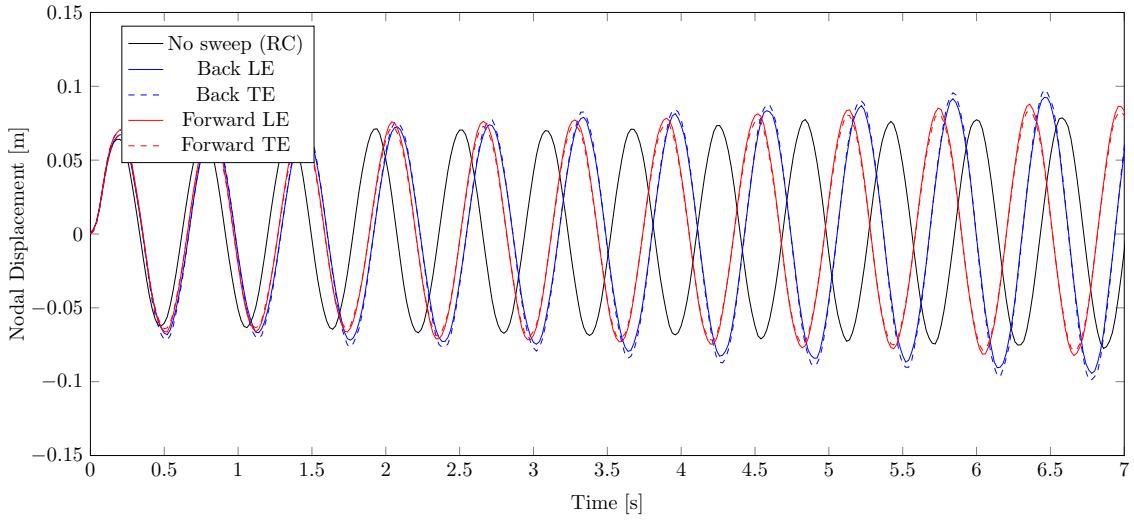

(a) Vertical displacement of LE wing tip node.

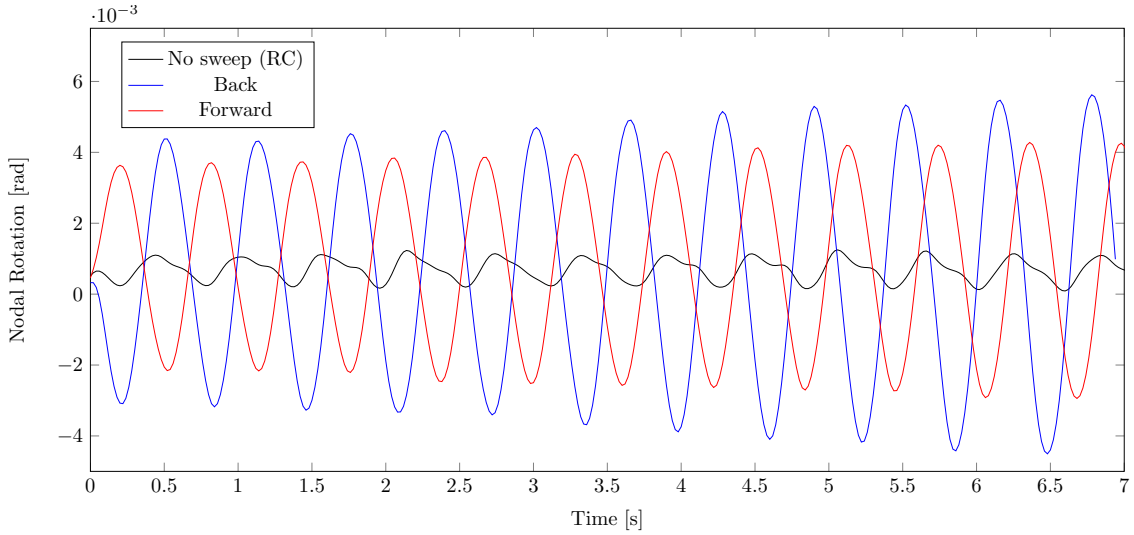

(b) Rotation of LE wing tip node.

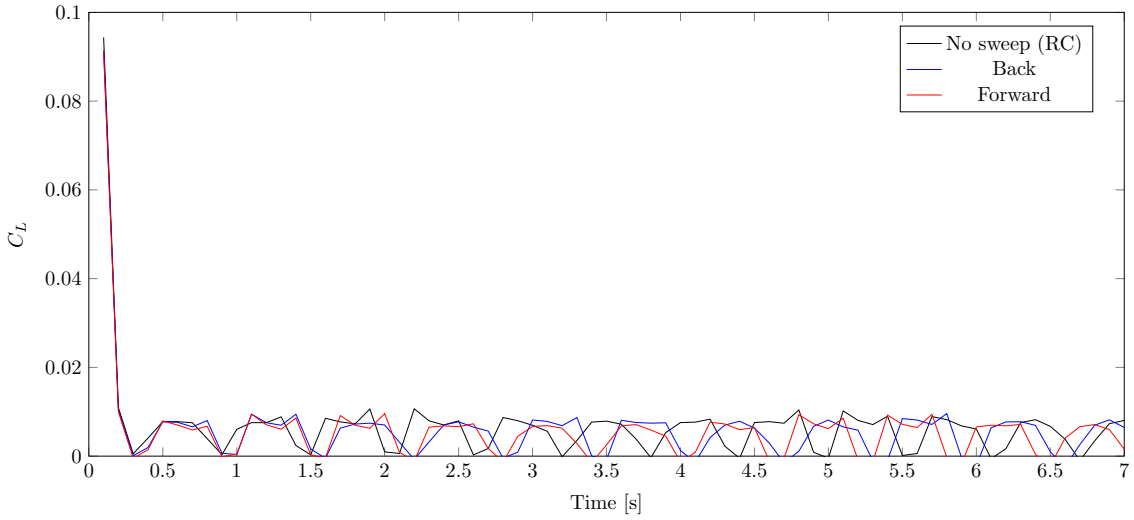

(c) Wing lift coefficient.

Figure 9.3: Influence of the sweep angle in the aeroelastic wing behavior.

Herein, the influence of the density is investigated. Taking a look back at Chapter 2, the density will have influence on the structural mass matrix M defined in Equation (2.5). Equation (2.3) shows that M influences the inertial forces, since it is multiplied by the acceleration vector $\ddot{\vec{u}}$. So, the higher the density, the higher the inertial forces.

The RC presented in Chapter 8 used the mechanical properties of steel. Since the goal here is to study only one parameter, unrealistic materials will be used. Having the RC a density of 7800 kg/m^3, two more computations were made using 5000 and 10000 kg/m^3. Figure 9.4 summarizes the results.

In Figure 9.4(a), one can immediately see that the density influences mainly the frequency of the vertical movement. Table 9.1 summarizes the frequency calculation for the three computations.

Table 9.1: Period and frequency of the vertical movement for changing material density.

Density [kg/m^3]	First peak [s]	Last peak [s]	Number of peaks	Period [s]	Frequency [Hz]
5000	0.16	6.82	15	0.476	2.10
7800	0.20	6.56	12	0.580	1.72
10000	0.22	6.72	11	0.65	1.54

Figure 9.4(a) also shows that reducing density also helps the wing to diverge, since the peak values increase in comparison with the RC. In reverse, the heavier wing has more inertia causing the amplitude of the oscillations to be smaller.

Figures 9.4(b) and 9.4(c) basically show accordance to 9.4(a) in terms of the frequency, like it was expected.

9.5 Skin Young Modulus

Next, the influence of the elasticity or Young modulus E will be tested. This parameter is present in D (Equation (2.2)), which is used to calculate K (Equation (2.4)). Increasing E makes the material more stiff, while decreasing makes it more elastic.

Having the reference value of 200 GPa, two more computations were made with 100 and 300 GPa.

The results are clear in Figure 9.5. As soon as one decreases the Young modulus, both bending and torsion amplitudes will increase, likewise the period. In this specific case, the increase to 300 GPa also transforms the movement to convergent, since the amplitude is decreasing with the time.

The lift coefficient does not suffer a significant change, besides the frequency which is in accordance with Figures 9.5(a) and 9.5(b).

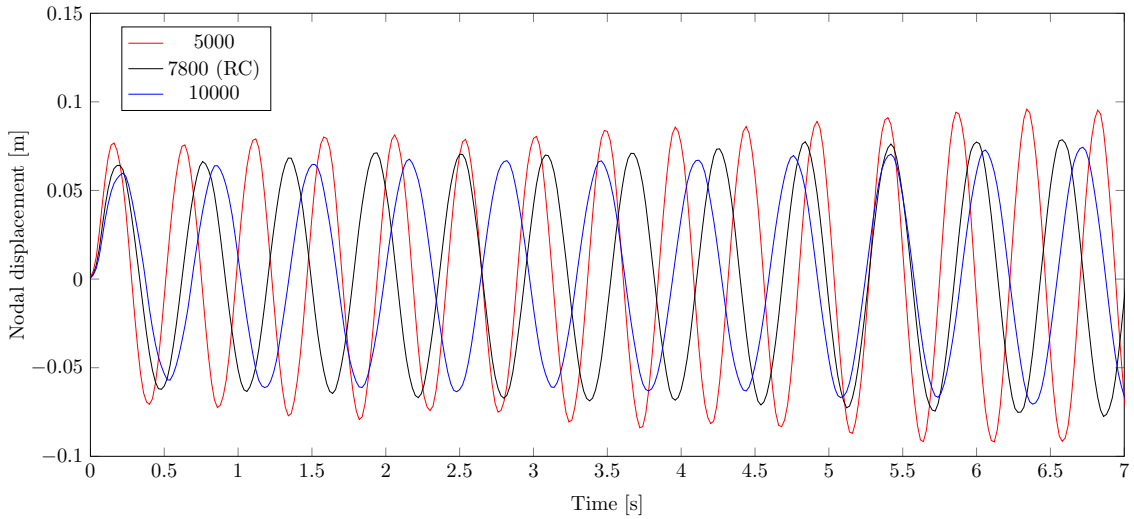

(a) Vertical displacement of LE wing tip node.

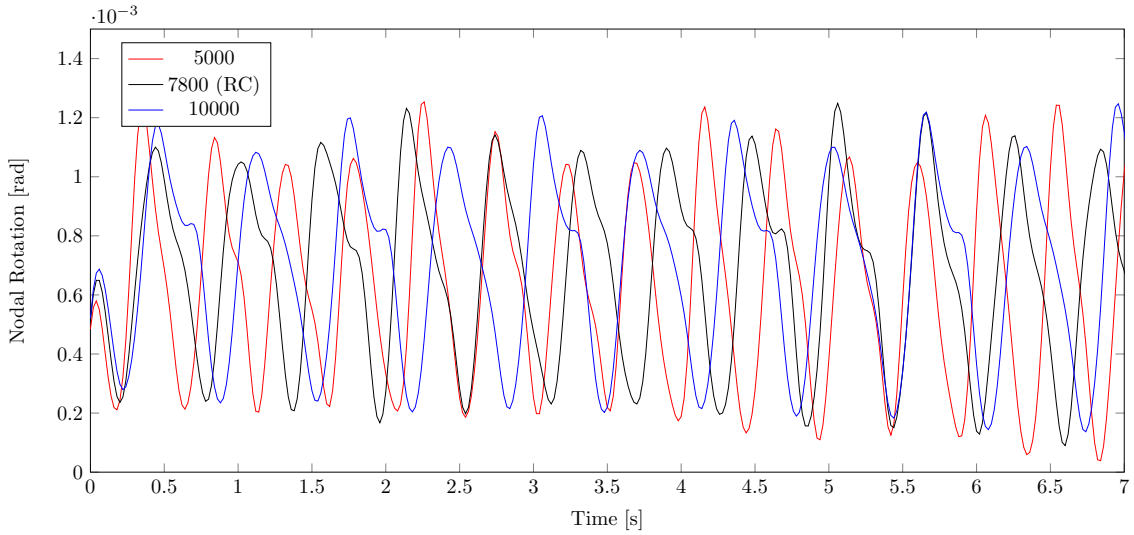

(b) Rotation of LE wing tip node.

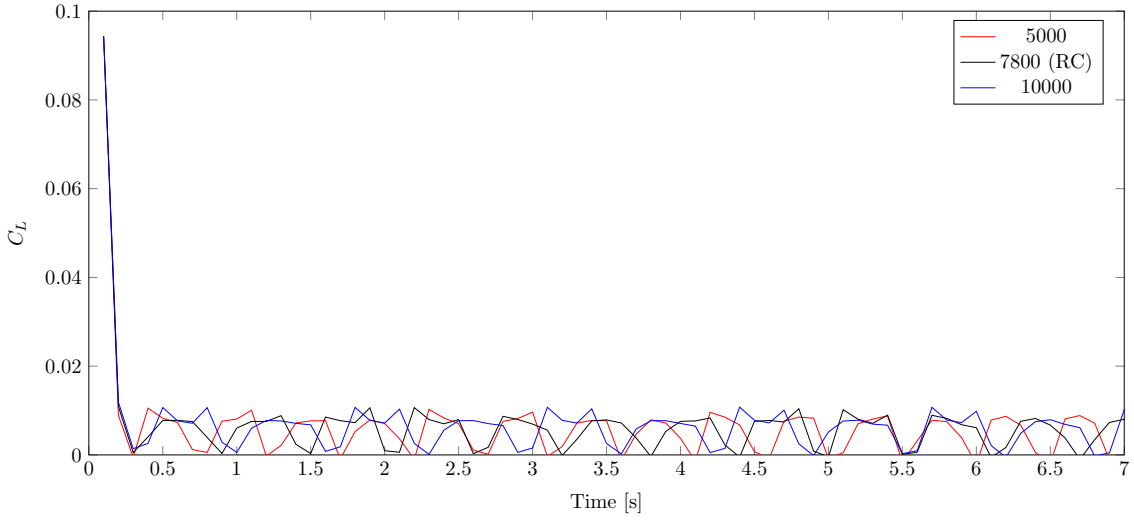

(c) Wing lift coefficient.

Figure 9.4: Influence of the skin density [kg/m^3] in the aeroelastic wing behavior.

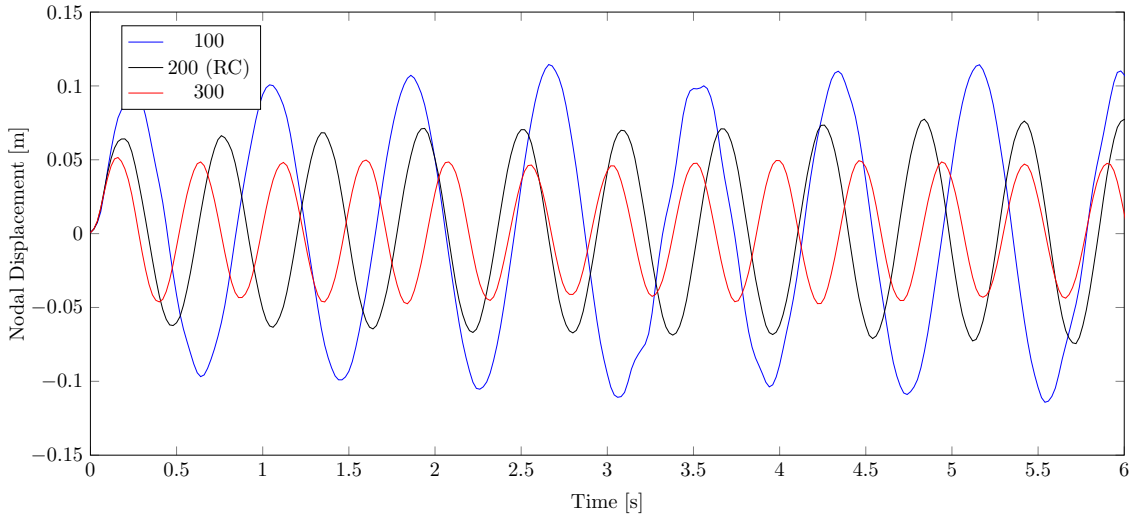

(a) Vertical displacement of LE wing tip node.

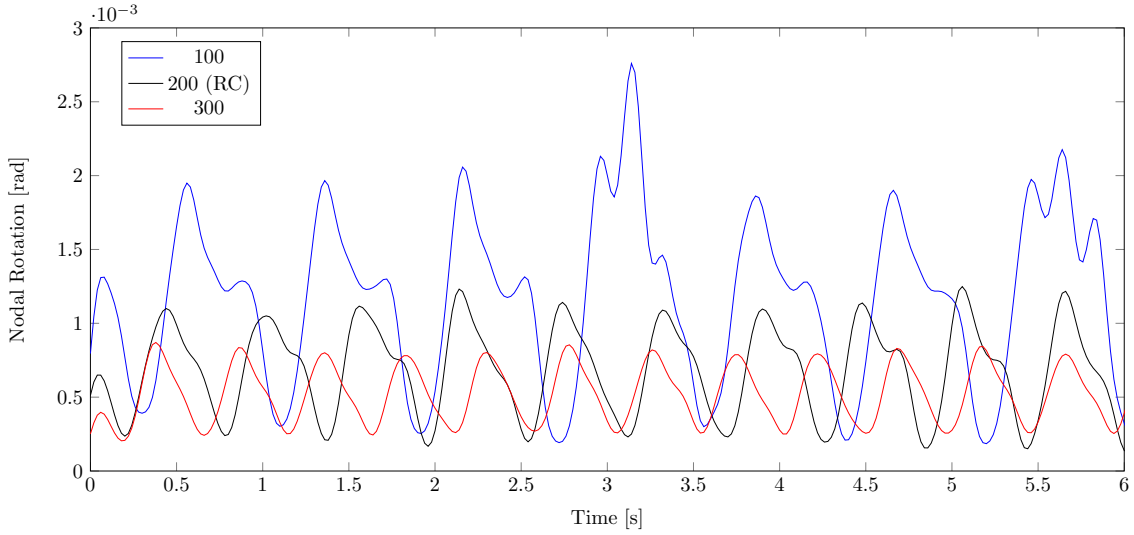

(b) Rotation of LE wing tip node.

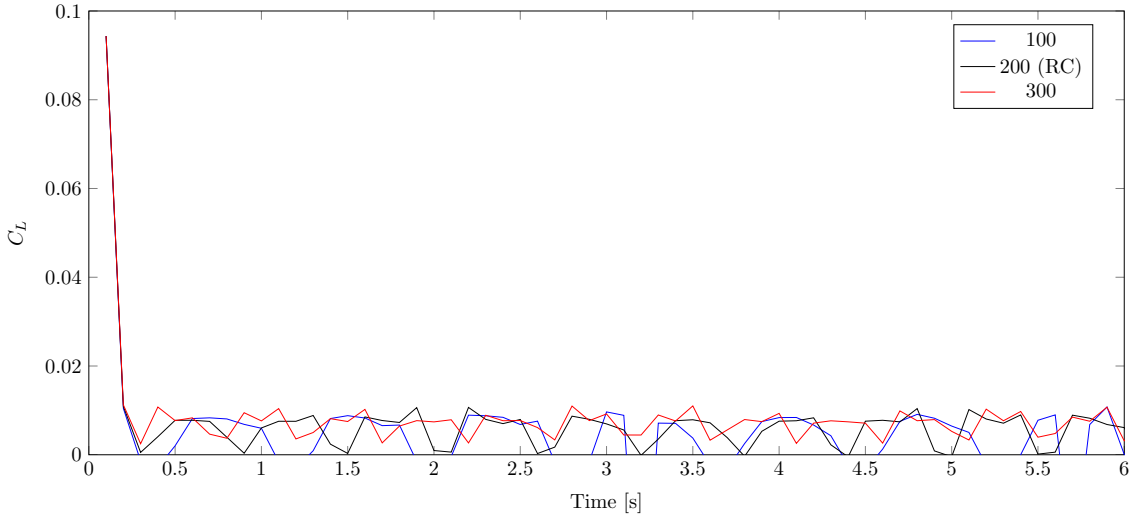

(c) Wing lift coefficient.

Figure 9.5: Influence of the skin Young modulus [GPa] in the aeroelastic wing behavior.

Chapter 10

Conclusions

An aeroelastic design framework was presented for the study of aircraft wings. It is composed by three main parts: the structure solver APDL, the fluid solver a panel method coded in MATLAB and a coupling procedure also in MATLAB which controls the other two parts.

The fluid solver was fully developed in MATLAB, going from the steady two-dimensional to the unsteady three dimensional problem, being the two-dimensional case validated with exact results from the potential theory and the three-dimensional validated with wind tunnel tests. Furthermore, the results were also compared with another panel method program presented in [37] and with XFOIL.

The structure solver is called from MATLAB using the technique described in Appendix A. The mesh nodes and elements, the material constants, the section types and thickness, the loads and the initial conditions are saved to files by MATLAB and then read from APDL, which, in turn, writes the nodal displacements, velocities and rotations to another files. This method proved to be very efficient and reliable.

The FSI normally generates some issues like the transfer of loads and displacements, the frame of reference and the added mass. The first two were very simplified, since the fluid solver used made it possible to use the same grid in both domains, having only left the Load Lumping issue, which was proved to be accurate. The latter just influences cases when the fluid and structure densities are comparable, for instance blood flows inside veins.

The aeroelastic framework created starts with a fluid steady solution for the values input by the user. Then, it generates the structural mesh which remains the same during all the computation. After the first structural solution, a time cycle starts performing a defined number of cycles with the same time step for both fluid and structure solver. The latter has however the possibility to have substeps to track the body movement more precisely.

Having defined a reference group of inputs, a dynamic and a static computation were performed. The latter was just to check if everything is correct with the framework. By having no inertial forces, the system should evolve to a stable position, which was the result observed. The dynamic study is the main focus of this work.

In dynamic aeroelasticity, it is usual to calculate the flutter velocity. Therefore that was the first

parameter to vary and the results show that it is possible to calculate an approximate flutter velocity for an aircraft wing. The other tests showed that the spar position changes the wing center of twist, the sweep angle changes the coupling between the bending and torsion movements, the skin density influences the inertial forces and consequently the period and amplitude of the bending movements, as well as the Young modulus which influences the material stiffness or elasticity.

10.1 Achievements

A fluid solver was fully created capable to compute aircraft wings with sweep, dihedral and tapering, given only the airfoil coordinates, the $\mathcal{AR}$ and those parameters. This solver was fully validated.

An aeroelastic design framework was created using two commercial programs and several tests were performed, which proved that it provides physically correct results.

10.2 Future Work

As it was said before, the absence of structural elements like stringers, forced the use of very thick skin elements. A more realistic step would be to add elements to the structural mesh to simulate the stringers.

APDL Batch run proved to be efficient but it also caused some problems having errors arising from some conflicts with Windows. A certainly great improvement would be to program a structural transient solver in MATLAB which would be easier to couple with the panel method.

Two coupling procedures were tested and also two fluid time integration schemes. The possibility of having both solvers coded in MATLAB would make possible a monolithic approach with different discretization methods.

A very important step would be to construct a wing model and obtain wind testing data in order to validate the results computed by this framework.

Further work can also be pursued in shape or topology optimization using the aeroelastic analysis framework here developed and presented. Tackling problems of flutter speed maximization of an aircraft wing with constraints in weight is something of utmost importance in very high performance aircrafts.

Bibliography

[1] J. Katz and A. Plotkin, *Low-Speed Aerodynamics*, 2nd ed., ser. Cambridge Aerospace Series, M. J. Rycrift and W. Shyy, Eds. Cambridge University Press, 2001, no. 13.

[2] J. Kouh and J. Suen, "A potential-based and desingularized high order panel method," *Ocean Engineering*, vol. 28, no. 11, pp. 1499–1516, 2001, doi:10.1016/S0029-8018(00)00069-X.

[3] A. Janus, "Winged wonders," Smithsonian National Air and Space Museum, March 2009, http://blog.nasm.si.edu/archives/winged-wonders/.

[4] A. R. Collar, "The first fifty years of aeroelasticity," *Aerospace*, vol. 5, no. 2, pp. 12–20, Feb. 1978.

[5] T. H. G. Megson, *Aircraft Structures for Engineering Students*, 4th ed., ser. Elsevier Aerospace Engineering Series. Oxford: Butterworth-Heinemann, 2007.

[6] Boeing, Visited in March 2014, http://wallpho.com/27017-bell-boeing-v-22-osprey-id-18530.htm.

[7] Airbus, Visited in September 2014, http://www.nomenclaturo.com/tag/airplane-wing.

[8] *ANSYS Mechanical APDL Modeling and Meshing Guide*, ANSYS, Inc., Canonsburg, PA, November 2010, release 13.0.

[9] G. P. Guruswamy, "A review of numerical fluids/structures interface methods for computations using high-fidelity equations," *Computers & Structures*, vol. 80, no. 1, pp. 31 – 41, 2002, doi:10.1016/S0045-7949(01)00164-X.

[10] B. Maskew, "Program VSAERO theory document," NASA, Contractor Report 4023, 1987.

[11] E. H. Hirschel, H. Prem, and G. Madelung, *Aeronautical Research in Germany From Lilienthal until Today*, 1st ed. Berlin Heidelberg: Springer-Verlag, 2004.

[12] R. L. Bisplinghoff, H. Ashley, and R. L. Halfman, *Aeroelasticity*, 1st ed., ser. Dover Books on Physics. Mineola, New York: Dover Publications, Inc., 1996.

[13] R. Clark, D. Cox *et al.*, *A Modern Course in Aeroelasticity*, 4th ed., ser. Solid Mechanics and its Applications, E. H. Dowell, Ed. Dordrecht: Kluwer Academic Publishers, 2005, vol. 116.

[14] H. Ashley and G. Zartarian, "Piston theory - a new aerodynamic tool for the aeroelastician," *Journal of the Aeronautical Sciences*, vol. 23, no. 12, pp. 1109–1118, January 1956.

[15] G. SenGupta, J. Castro, and T. Kim, "Computational methods in aeroelasticity," AIAA Short Courses, Honolulu, HI, April 2007.

[16] R. Udrescu, "Effects of oscillating shock waves on the dynamics of fluttering panels," *19th AIAA Applied Aerodynamics Conference*, June 2001, doi:10.2514/6.2001-1669.

[17] X. Guo and C. Mei, "Application of aeroelastic modes on nonlinear supersonic panel flutter at elevated temperatures," *Computers & Structures*, vol. 84, pp. 1619–1628, January 2006, doi:10.1016/j.compstruc.2006.01.041.

[18] A. Pellegrino and C. Meskell, "Vortex shedding from a wind turbine blade section at high angles of attack," *Journal of Wind Engineering and Industrial Aerodynamics*, vol. 121, pp. 131–137, October 2013, doi:10.1016/j.jweia.2013.08.002.

[19] S. S. Bhat and R. N. Govardhan, "Stall flutter of NACA 0012 airfoil at low Reynolds numbers," *Journal of Fluids and Structures*, vol. 41, pp. 166–174, April 2013, doi:10.1016/j.jfluidstructs.2013.04.001.

[20] C. D. Turner, "Effect of store aerodynamics on wing/store flutter," *Journal of Aircraft*, vol. 19, no. 7, pp. 574–580, July 1982, doi:10.2514/3.57431.

[21] B. Singh and I. Chopra, "Elastic-blade whirl flutter stability analysis of two-bladed proprotor/pylon systems," *Journal of Aircraft*, vol. 42, no. 2, pp. 519–527, April 2005, doi:10.2514/1.2814.

[22] M. H. Love, P. S. Zink, P. A. Wieselmann, and H. Youngren, "Body freedom flutter of high aspect ratio flying wings," in *Proceedings of the 46th AIAA/ASME/ASCE/AHS/ASC Structures, Structural Dynamics and Materials Conference*, no. AIAA 2005-1947, Austin, Texas, April 2005, doi:10.2514/6.2005-1947.

[23] *Theory Reference for the Mechanical APDL and Mechanical Applications*, ANSYS, Inc., Canonsburg, PA, November 2010, release 13.0.

[24] F. P. Beer, J. E. R. Johnston, D. F. Mazurek, P. J. Cornwell, and E. R. Eisenberg, *Vector Mechanics for Engineers: Statics and Dynamics*, 9th ed. McGraw-Hill, 2010.

[25] J. D. Anderson, G. Degrez, E. Dick, and R. Grundmann, *Computational Fluid Dynamics An Introduction*, J. F. Wendt, Ed. New York: Springer-Verlag, 1992, a von Kármán.

[26] G. Borrell, J. A. Sillero, and J. Jiménez, "A code for direct numerical simulation of turbulent boundary layers at high Reynolds numbers in BG/P supercomputers," *Computers & Fluids*, vol. 80, pp. 37–43, July 2013, doi:10.1016/j.compfluid.2012.07.004.

[27] C. Hirsch, *Numerical Computation of Internal and External Flows*, 2nd ed. Oxford: Butterworth-Heinemann, 2007, vol. 1 Fundamentals of Computational Fluid Dynamics.

[28] P. Lu and C. Liu, "DNS study on mechanism of small length scale generation in late boundary layer transition," *Physica D*, vol. 241, pp. 11–24, January 2012, doi:10.1016/j.physd.2011.09.014.

[29] R. Bouffanais, "Advances and challenges of applied large-eddy simulation," *Computers & Fluids*, vol. 39, no. 5, pp. 735 – 738, 2010, doi:10.1016/j.compfluid.2009.12.003.

[30] L. Tan, B. Zhu, Y. Wang, S. Cao, and K. Liang, "Turbulent flow simulation using large eddy simulation combined with characteristic-based split scheme," *Computers & Fluids*, vol. 94, no. 0, pp. 161 – 172, 2014, doi:10.1016/j.compfluid.2014.01.037.

[31] L. Davidson, "The PANS model in a zonal hybrid RANS-LES formulation," *International Journal of Heat and Fluid Flow*, vol. 46, no. 0, pp. 112 – 126, 2014, doi:10.1016/j.ijheatfluidflow.2014.01.002.

[32] D. Kirshman and F. Liu, "Flutter prediction by an Euler method on non-moving cartesian grids with gridless boundary conditions," *Computers & Fluids*, vol. 35, no. 6, pp. 571 – 586, 2006, doi:10.1016/j.compfluid.2005.04.004.

[33] P. K. Kundu and I. M. Cohen, *Fluid Mechanics*, 2nd ed. Academic Press, 2002.

[34] E. Kreyszig, *Advanced Engineering Mathematics*, 10th ed. John Wiley & Sons, Inc., 2011.

[35] D. E. Raveh, "Computational–fluid–dynamics–based aeroelastic analysis and structural design optimization–a researcher's perspective," *Computer Methods in Applied Mechanics and Engineering*, vol. 194, no. 30 - 33, pp. 3453 – 3471, 2005, doi:10.1016/J.CMA.2004.12.027.

[36] J. Moran, *An Introduction To Theoretical And Computational Aerodynamics*. New York: John Wiley & Sons, Inc., 1984.

[37] J. M. R. D. C. Baltazar, "On the modelling of the potential flow about wings and marine propellers using a boundary element method," PhD dissertation, Instituto Superior Técnico (IST), September 2008.

[38] Y. Bazilevs, K. Takizawa, and T. E. Tezduyar, *Computational Fluid-Structure Interaction Methods And Applications*, 1st ed., ser. Wiley Series In Computational Mechanics. UK: John Wiley & Sons, Inc., 2013.

[39] R. Kamakoti and W. Shyy, "Fluid–structure interaction for aeroelastic applications," *Progress in Aerospace Sciences*, vol. 40, no. 8, pp. 535 – 558, 2004, doi:10.1016/j.paerosci.2005.01.001.

[40] M. Souli and D. J. Benson, Eds., *Arbitrary Lagrangian–Eulerian and Fluid–Structure Interaction*, 1st ed. USA: John Wiley & Sons, Inc., 2010.

[41] C. Farhat and M. Lesoinne, "Two efficient staggered algorithms for the serial and parallel solution of three–dimensional nonlinear transient aeroelastic problems," *Computer Methods in Applied Mechanics and Engineering*, vol. 182, no. 3 - 4, pp. 499 – 515, 2000, doi:10.1016/S0045-7825(99)00206-6.

[42] S. Piperno and C. Farhat, "Partitioned procedures for the transient solution of coupled aeroelastic problems – part II: energy transfer analysis and three-dimensional applications," *Computer Methods in Applied Mechanics and Engineering*, vol. 190, no. 24 - 25, pp. 3147 – 3170, 2001, doi:10.1016/S0045-7825(00)00386-8.

[43] R. Szilard, *Theories and Applications of Plate Analysis: Classical, Numerical and Engineering Methods*. Hoboken, New Jersey: John Wiley & Sons, Inc., 2004.

[44] P. K. Gudla and R. Ganguli, "Error estimates for inconsistent load lumping approach in finite element solution of differential equations," *Applied Mathematics and Computation*, vol. 194, no. 1, pp. 21 – 37, 2007, doi:10.1016/j.amc.2007.04.009.

[45] *Verification Manual for ANSYS Mechanical APDL*, ANSYS, Inc., Canonsburg, PA, November 2010, release 13.0.

[46] A. S. Iglesias, "Hess-smith panel method," 2009, cFD WORKSHOP - Athens Course UPM 41.

[47] M. Drela, "XFOIL: An analysis and design system for low Reynolds number airfoils," Conference on Low Reynolds Number Airfoil Aerodynamics, June 1989, university of Notre Dame.

[48] V. de Brederode, *Fundamentos de Aerodinâmica Incompressível*. Department of Mechanical Engineering, IST, Lisbon: Autor Edition, 1997, (in Portuguese).

[49] C. Xie, Y. Liu, and C. Yang, "Theoretic analysis and experiment on aeroelasticity of very flexible wing," *Science China Technological Sciences*, vol. 55, no. 9, pp. 2489–2500, 2012, doi:10.1007/s11431-012-4941-3.

[50] MathWorks, "Use Matlab editor to write and run Ansys program," March 2011, http://www.mathworks.com/matlabcentral/fileexchange/30887-use-matlab-editor-to-write-and-run-ansys-program.

[51] ——, "Signal processing toolbox," http://www.mathworks.com/help/signal/index.html.

[52] G. K. Amanda, P. P. Sukumar, and M. S. Selig, "Low-to-moderate aspect ratio wings tested at low Reynolds numbers," in *30th AIAA Applied Aerodynamics Conference*, no. 2012-3026, New Orleans, LA, June 2012.

[53] C. Farhat, P. Geuzaine, and G. Brown, "Application of a three–field nonlinear fluid–structure formulation to the prediction of the aeroelastic parameters of an F–16 fighter," *Computers & Fluids*, vol. 32, no. 1, pp. 3 – 29, 2003, doi:10.1016/S0045-7930(01)00104-9.

[54] D. H. Hodges and G. A. Pierce, *Introduction to Structural Dynamics and Aeroelasticity*, 2nd ed. New York: Cambridge University Press, 2011.

[55] J. R. Wright and J. E. Cooper, *Introduction to Aircraft Aeroelasticity and Loads*, ser. Aerospace Series. Chichester, England: John Wiley & Sons, Ltd, 2007.

Appendix A

MATLAB-APDL Bridge

In order to couple the fluid and structure solver, it was needed to open the APDL with a MATLAB command. The solution was found in the Mathworks website [50].

Basically, the APDL script is written in MATLAB, then converted to an APDL extension. Then APDL is opened in a silent mode called the *Batch run* which does not open a GUI, but instead runs the commands and prints the results to files and even takes print screens to the results if required by the user. The command is

```
dos([AnsysPath ' -m ' num2str(workspace) ' -db ' num2str(database) ' -b -p ANE3FL ' '-i
' FileName '.inp ' '-o fem_temp.out'],'-echo');,
```

where `AnsysPath` is the APDL installation directory. The `dos` MATLAB function introduces a command in the Windows MS-DOS inputing `Filename.inp`, which is the APDL script and outputting `fem_temp.out`. It is also possible to have more inputs and outputs using APDL commands to read from file and write on file.

Using this technique, MATLAB waits until the APDL finishes its run and then continues, making it possible to read the output right after the analysis.

Appendix B

Curve Filtering

After several aeroelastic computations using the framework here designed, it was recognized that the rotational movement had many microscopic oscillations which are not being modeled and do not interest in this problem. To be able to see only the macroscopic movement, a filtering work was done using the MATLAB Signal Analysis Toolbox [51], which allows the user, among many other tasks, to design filters.

Since one wants to eliminate the microscopic oscillations, the same is saying that one needs a filter to eliminate the high frequency oscillations or a *Lowpass filter*. To design the filter, many parameters are needed, namely the sampling frequency which determined from the used time step and the stop frequency which is based on the frequencies which were calculated on the movement and then simple adjusted with many tries.

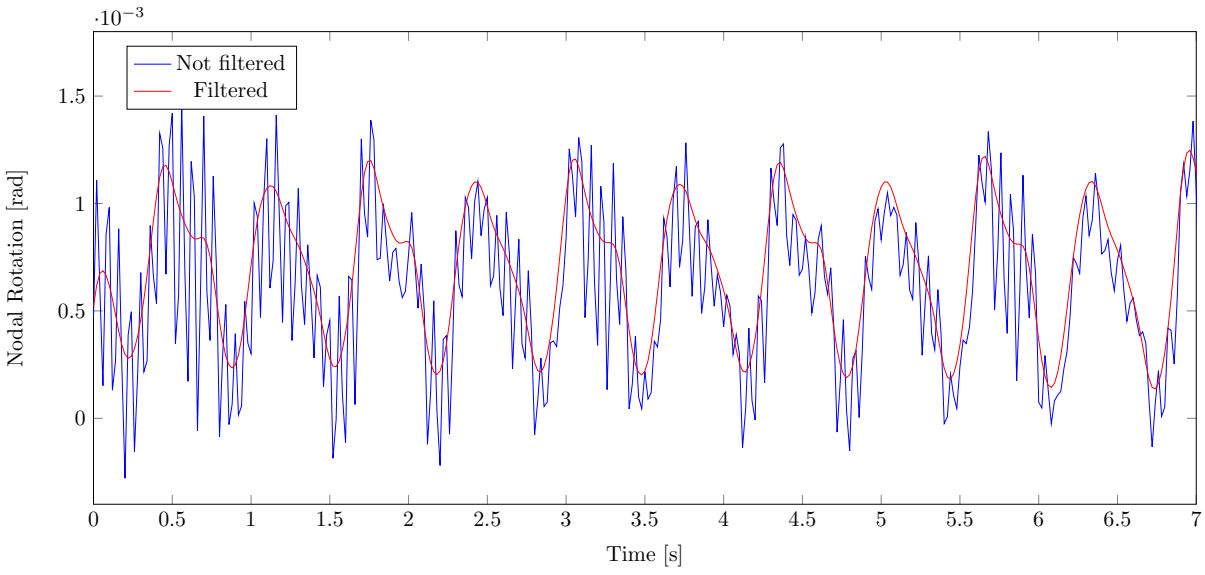

Figure B.1: Example of the filtering of the curve in Figure 9.4(b) correspondent to a density of 10000 kg/m^3.

Figure B.1 shows an example using a lowpass filter (Equiripple method) with sampling frequency 50 Hz ($\Delta t = 0.1$ with 5 substeps), end of the passband at 3 Hz, beginning of the stopband at 12 Hz, stopband attenuation of 100 dB and passband ripple of 1 dB.